ABSTRACT

Title of Document: STABILITY OF RIDGE-RIDGE-RIDGE TRIPLE JUNCTIONS BASED ON THE MECHANICS OF RIFT INTERACTION: THE NORTHERN GALÁPAGOS AND RODRIGUEZ TRIPLE JUNCTIONS

Garrett Alan Mitchell, Master of Science, 2010

Directed By: Assistant Professor Laurent G.J. Montési, Department of Geology

Although known for decades to be kinematically stable, Ridge-Ridge-Ridge (RRR) triple junctions sometimes display a complex sequence of short-lived rifts and no direct connection between the ridges. The Galápagos Triple Junction (GTJ), in the Eastern Equatorial Pacific Ocean and the Rodriguez Triple Junction (RTJ), in the Central Indian Ocean, serve as end-members of stability observed as RRR triple junctions. I propose that the stability of RRR triple junctions, principally whether secondary rifts are generated or direct connection between the spreading centers is favored, can be understood based on the mechanics of crack interaction. I develop numerical models of the stress field in an elastic plate under tension, with cracks representing rifts in the vicinity of a RRR triple junction and GIS spatial analysis to demonstrate the factors that control RRR triple junction's stability. Although RRR triple junctions are kinematically stable, rift junctions are mechanically unstable, generating a rapidly evolving and complex plate boundary.

STABILITY OF RIDGE-RIDGE-RIDGE TRIPLE JUNCTIONS BASED ON THE MECHANICS OF RIFT INTERACTION: THE NORTHERN GALÁPAGOS AND RODRIGUEZ TRIPLE JUNCTIONS

By

Garrett Alan Mitchell

Thesis submitted to the Faculty of the Graduate School of the
University of Maryland, College Park, in partial fulfillment
of the requirements for the degree of
Master of Science
2010

Advisory Committee:
Assistant Professor Laurent G.J. Montési, Chair
Assistant Professor Saswata Hier-Majumder
Assistant Professor Wenlu Zhu

Acknowledgements

I would like to first and foremost acknowledge my advisor, Laurent Montési, for all of the assistance and guidance he has provided me with throughout this study. I would also like to thank the members of my thesis committee – Saswata Hier-Majumder and Wenlu Zhu; Debbie Smith and Hans Schouten of Woods Hole Oceanographic Institution's Department of Geology & Geophysics for the invitation to participate on a research cruise to the Galápagos Triple Junction and the use of unpublished bathymetry; Chie Honsho of the University of Tokyo for the gracious use of bathymetry of the Rodriguez Triple Junction; and finally to my family, in particular my mother, Pat and my fiancé, Susannah for their love and support.

Table of Contents

List of Tables

Appendix A: GIS Database

Appendix B: Model Data Tables

List of Figures

Chapter 1: Introduction

1.1 Triple Junctions

A fundamental tenet of plate tectonics is that the lithosphere is essentially rigid except at plate boundaries. There, plates can either diverge, converge, or simply slide past each other. Plate boundaries form a global interconnected geometric network, where three plate boundaries occasionally must connect as a consequence of a multi-plate planet. This is known as a triple junction, a singular point from which three plate boundaries radiate away, bounding three different plates (McKenzie and Parker, 1967; McKenzie and Morgan, 1969; Patriat and Courtillot, 1984).

The type of motion present at each of the boundaries at triple junctions, and the azimuth of each boundary controls the stability of a triple junction, which is defined by its kinematic ability to retain its geometry over time (McKenzie and Morgan, 1969; Patriat and Courtillot, 1984). Of the sixteen configurations discussed in McKenzie and Morgan (1969), only six are presently identified on Earth. The others are either unstable, or stable only for specific values of boundary orientations, which is unlikely to be realized over geologic time as plate motions constantly change (Cronin, 1992). Therefore, these boundaries are transient by nature. Of the various junction configurations, ridge-ridge-ridge (RRR) triple junctions are the most stable (McKenzie and Morgan, 1969). However, RRR triple junctions display a more complex geologic history than their long-term kinematic stability might suggest.

1.2 Ridge-Ridge-Ridge Triple Junctions and their Stability

Presently, RRR triple junctions are observed in the North Atlantic (Azores Triple Junction, Krause and Watkins, 1970; Searle 1980), South Atlantic (Bouvet Triple Junction, Sclater et al., 1976; Mitchell and Livermore, 1998; Ligi et al., 1999), Southwest Indian Ocean (Rodriguez Triple Junction, Tapscott et al., 1980; Sclater et al., 1981; Mitchell 1991; Mitchell and Parsons, 1993; Patriat et al., 1997), and the Eastern Pacific (Easter Island Triple Junction, Bird and Naar, 1994; Bird et al., 1999, and Galápagos Triple Junction, Searle and Francheteau, 1986, Lonsdale 1988)(Figure 1). The Easter Island RRR Triple Junction, at the junction between the Pacific, Antarctic, and Nazca plates, and the Galápagos RRR Triple Junction (GTJ), separating the Pacific, Cocos, and Nazca plates, are both observed to contain rotated abyssal hill fabric and microplates (Lonsdale, 1988; Larson et al., 1992; Bird & Naar, 1994; Bird et al., 1999; Klein et al., 2005). All of these RRR triple junctions are kinematically stable but exhibit complex tectonic features. Their history of local instability demonstrates that a kinematic description of stability is insufficient.

Several RRR triple junctions, most notably the Bouvet Triple Junction in the Southern Atlantic Ocean, temporarily adopt a ridge-ridge-fault (RRF) or ridge-fault-fault (RFF) configuration (Ligi et al., 1999). Current RRF or RFF triple junctions appear to evolve towards a RRR configuration (Fournier et al., 2008). Cronin (1992) proposed that RRR triple junctions are unstable with respect to finite amplitude plate motions, except in a few limited cases.

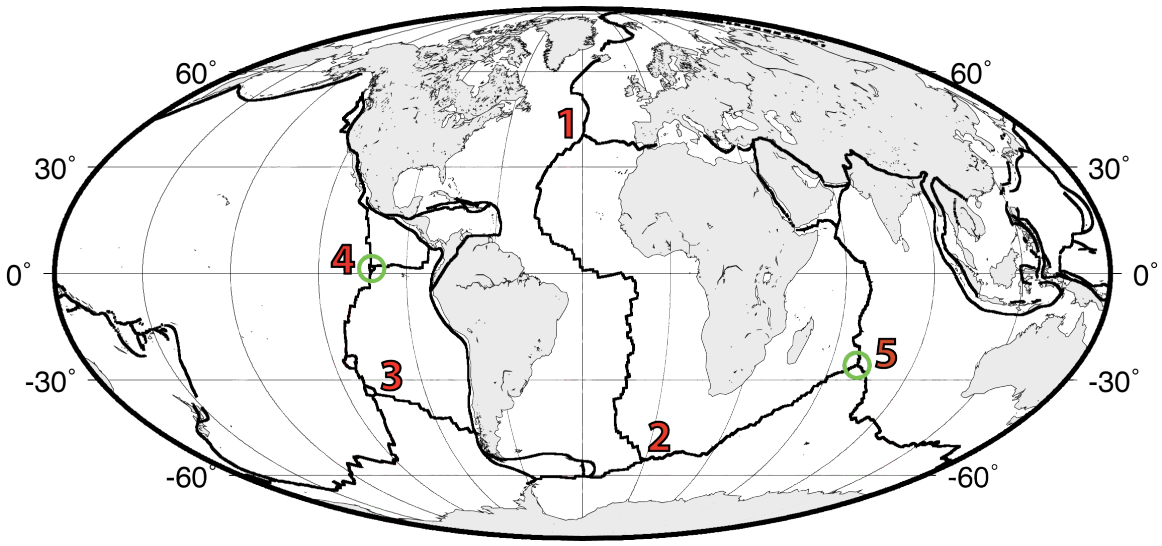

Figure 1. Location of the Earth's ridge-ridge-ridge (RRR) triple junctions. 1: Azores triple junction, North Atlantic. 2: Bouvet triple junction, South Atlantic. 3: Easter Island triple junction, Eastern Pacific. 4: Galápagos triple junction, Eastern Pacific. 5: Rodriguez triple junction, Eastern Pacific. Möllweide projection map centered at 30° W longitude. Green circles represent the triple junctions in the study.

Because the ridges involved at a triple junction have different spreading rates, the slowest ridge must propagate to maintain the triple junction configuration (McKenzie and Morgan, 1969). Reconstructions and observations of oceanic RRR triple junctions indicate that these junctions are characterized by episodic migration that involve propagating rifts and the formation and accretion of microplates in order to retain their kinematic stability (Bird et al., 1999). Even the Rodriguez triple junction in the Indian Ocean, which has been stable for the past 40 Ma (Sclater et al. 1981; Patriat and Segoufin, 1988), features a zone of distributed deformation associated with the propagation of the Southwest Indian Ridge (Sauter et al., 1997). At the GTJ, the Cocos-Nazca Rift (CNR) must propagate to keep pace with the faster-spreading East Pacific Rise. This propagation appears to be accompanied by the generation of a sequence of short-lived rifts roughly 70 km north of the CNR (Schouten et al., 2008) The Rodriguez triple junction contains a similar area of

lineations that crosscut Central Indian Ridge-generated abyssal hills (Mitchell, 1991). The kinematic stability of RRR triple junctions appears to be linked to the secondary ridges, transform faults, and microplates found in the vicinity of these triple junctions.

In order to analyze the factors that contribute to a RRR triple junction's stability, specifically why the GTJ features a lack of connection between the major ridges and a region of extinct secondary rifts whereas the RTJ has a much simpler geometry and a direct connection between ridges, I generate numerical models to examine RRR triple junction stability. Chapter 2 features a description of the tectonic settings of both the GTJ and RTJ. Chapter 3 presents a GIS analysis of the secondary rifts found at the GTJ, followed by a description of my previous results of GTJ modeling in Chapter 4. Chapters 5 and 6 contain a description of further numerical modeling of both the GTJ and RTJ investigating rift propagation, rift interaction, and an analysis of ridge geometry on stability. These results are then applied to both study areas along with an examination of the other RRR triple junctions in Chapter 7. The appendices contain a geospatial database, data tables, stress enhancement maps, and the numerical methods used in the study.

Chapter 2: Tectonic Setting of the Northern Galápagos and Rodriguez Triple Junctions

2.1 Northern Galápagos Triple Junction

At plate scale, the GTJ is the junction between the Cocos-Nazca Rift (CNR) and the East Pacific Rise (EPR, Figure 2). The EPR is a north-south trending oceanic spreading center that defines the eastern edge of the Pacific plate in the eastern equatorial Pacific Ocean. The fastest spreading rates on Earth of 150 mm/yr occur along the Southern East Pacific Rise, and the spreading rates of the EPR in the vicinity of the GTJ are 133 mm/yr (DeMets et al., 1994). The Cocos-Nazca Rift (CNR) is an east-west trending, 3 km high, volcanic ridge spreading at a rate of 42 mm/yr. It is propagating westward into a 5400 m deep intra-oceanic rift valley located at the tip of the Cocos-Nazca plate boundary. Westward propagation of the CNR has opened up a deep fissure in young oceanic crust called the Hess Deep rift basin that represents the tip of the Cocos-Nazca spreading center (Lonsdale, 1988).

Complexity in the regional tectonics appears to be associated with the termination of the CNR at Hess Deep. First, because of this termination, the CNR is not directly connected to the EPR. Second, secondary rifts have been identified along the EPR at 1°10'N and 2°40'N, forming a pair of actual RRR triple junctions (Searle and Francheteau, 1986; Lonsdale, 1988; Klein et al., 2005). The Galápagos microplate is bounded to the north and the south by these rifts. It was proposed that

the CNR termination at Hess Deep divides the Galápagos microplate into two counter-rotating microplates (Schouten et al., 1993; Klein et al., 2005).

The 1°10'N triple junction is defined by its intersection between the EPR and the Dietz Deep Rift. It appears to be the more stable of the two triple junctions, possibly because of a large seamount located in the vicinity of the Dietz Deep Rift (Lonsdale, 1988) or perhaps due to a more robust magma supply along the EPR.

The 2°40'N triple junction is marked by the Incipient Rift (IR). Lonsdale (1988) and Lonsdale et al. (1992) described the IR as a small westward propagating rift opening at 15mm/yr with a V-shaped eastern end. Further surveying to the northeast of the triple junction (Klein et al., 2005) revealed that the north-south trending abyssal hills are crosscut with a series of multiple extinct ancient rifts with similar orientations to that of the IR (Schouten et al., 2008). Thus, the IR appears to be the youngest of a set of short-lived rifts located to the North of the GTJ (Schouten et al., 2008). In addition, the eastern half of the IR narrows eastward, suggesting both eastward and westward propagation of the rift (Klein et al., 2005).

2.1.1 Northern Rifting at 2°40' N

The succession of transient extinct rifts located north of CNR is outlined in Figure 2C and was discussed in detail in by Schouten et al., (2008). A 250 km long and 50 km wide region northeast of the triple junction is delineated by a sharp transition in seafloor fabric from N-S trending abyssal hills characteristic of the EPR, to WNW-ESE-trending rifts. Schouten et al. (2008) identify over twenty-five rifts. Of these secondary rifts, the 100 km-long Extinct Rift (ER) is the largest and the IR is the youngest. All these extinct secondary rifts display a similar morphology and

azimuth, and are therefore interpreted to have once marked the Northern Galápagos triple junction. Schouten at al. (2008) suggest that these unstable rifts are moving north along the EPR, detaching from the EPR, and are rafted away with the northeast motion of the Cocos plate.

Schouten et al. (2008) developed a simple crack model to explain the generation of secondary rifts based on the gap between the tip of the CNR and the EPR. They modeled the Galápagos Triple Junction as a 2D rectangular elastic thin plate, subjected to N-S extension. In their model, a stress-free ellipse represents the CNR. It terminates at a distance *D* from a stress-free western boundary representing the EPR. Their model shows a decrease in tensile stress along the EPR ahead of the CNR tip and an increased tensile stress at ± 1.4*D* for the projection of the CNR along the EPR. They proposed that the zone of reduced tension is prohibiting the CNR from directly connecting to the EPR, preventing the formation of a simple RRR triple junction. The model also associates the current location of the RRR triple junction at 2°40' N with the regions of maximum stress enhancement at ±1.4*D* from projection of the CNR along the EPR. For application to the GTJ, *D* is approximately 50 km, the distance between Hess Deep and the EPR. Then, the region of maximum stress enhancement is approximately 70 km north along the EPR, which closely corresponds to the location of the 2°40'N triple junction. One goal of my study is to develop more complete models of rift interaction to further understand why the Northern GTJ appears unstable and why a succession of short-lived rifts formed North of the CNR.

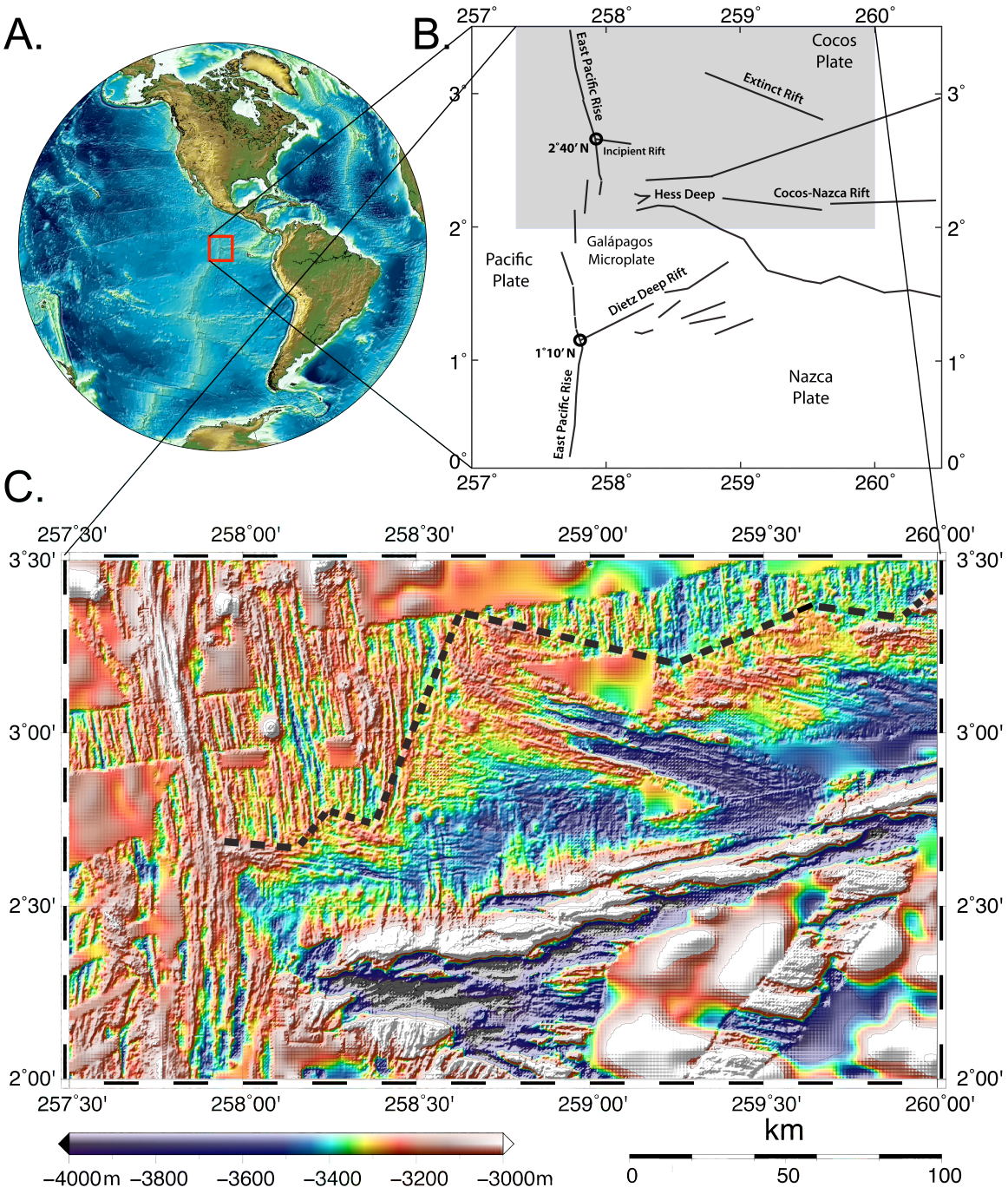

Figure 2: Regional and local tectonic setting of the Galápagos Triple Junction, a complex tectonic triple junction. Two RRR triple junctions are located at 1°10' N where the Dietz Deep Rift connects with the EPR and 2°40' N where the IR connects to the EPR. The Cocos-Nazca Rift is propagating westward without directly connecting with the EPR. The 2°40' N triple junction is characterized by a succession of extinct secondary rifts with similar azimuths and are outlined by the dashed line. Global bathymetry by Smith and Sandwell and local bathymetry from Schouten et al. (2008).

2.2 Rodriguez Triple Junction

In the Indian Ocean, the Rodriguez RRR Triple Junction (RTJ) separates the Indian, African, and Antarctic Plates (Figure 3). The three mid-ocean ridges defining this geometrically simple triple junction are the Central Indian Ridge (CIR), Southeast Indian Ridge (SEIR), and the Southwest Indian Ridges (SWIR). Their full spreading rates are 48, 58, and 14 mm/yr, respectively. Ridge spreading rates are obtained from Bill Menke's online plate velocity calculator. Numerous studies of the RTJ have been conducted since the pioneering work of McKenzie and Sclater (1971). Its geology is reported by Tapscott et al. (1980), Sclater et al. (1981), Mitchell (1991), Mitchell and Parsons (1993), Honsho et al. (1996), Patriat et al. (1997), and in Sauter et al. (1997).

As at the GTJ, the slowest spreading ridge at the RTJ (SWIR) intersects the faster spreading ridges, the CIR and SEIR, quasi-orthogonally. Thus, it must propagate to keep pace with the CIR and SEIR (Honsho et al., 1996; Sauter et al., 1997). This is an unavoidable characteristic of stable triple junctions if the ridges involved with the triple junction have different spreading rates (McKenzie and Morgan, 1969). The RTJ appears to be the most stable of the RRR triple junctions currently observed, with a stable configuration since 40 Ma and perhaps as along as 60 Ma (Patriat, 1987; Patriat and Segoufin, 1988).

The SWIR is defined by a deep intra-oceanic rift valley reaching depths of up to 5400 m, similar to the geologic setting of the CNR at the GTJ. However, the RTJ features a direct connection between the major ridges where the SWIR directly connects to a short segment of the CIR trending ~N347°W and an 85 km-long

segment of the SEIR that trends at ~N320°W. The axis of the CIR is kinked near the RRR triple junction where its new trend is approximated to be ~N328°W.

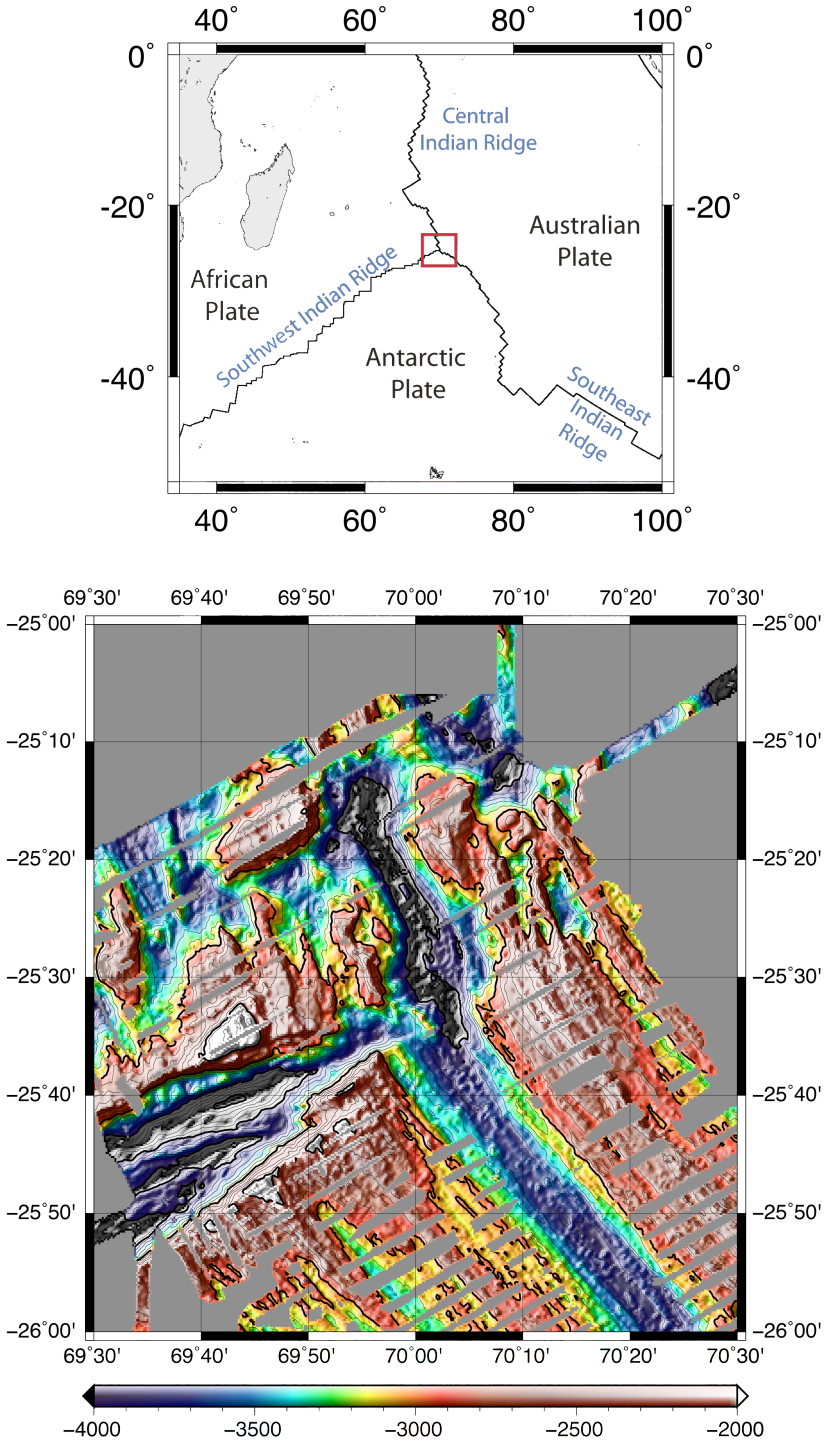

Figure 3. Regional and local maps of the Rodriguez Triple Junction, the junction between the African, Australian, and Antarctic Plates in the Indian Ocean. Unlike the complex Galápagos Triple Junction, the RTJ is characterized by a simple geometry between the Central Indian, Southeast Indian, and Southwest Indian Ridges.

This first segment of the SEIR contains a 3600 m deep rift valley that is connected to the second shorter segment by a left-lateral transform fault. This second segment of the SEIR trends at ~N314ºW and is contains a deeper (4200 m) axial valley with a more rugged seafloor suggesting a limited underlying magma supply (Honsho et al., 1996). The axis of the CIR is kinked near the RRR triple junction where its new trend is approximated to be ~N328°W.

Unlike the EPR at the GTJ, the SEIR and CIR spread at rates sufficiently different so that they cannot be regarded as a straight ridge. Although the geometrical complexity of the CIR near the RTJ makes it difficult to directly measure the angle between the CIR and SEIR, that angle is clearly less open than between the EPR North and South of the GTJ. One goal of my study is to determine to what extent the angle between the faster ridges of a triple junction influences rift interaction and use this angle to explain why the RTJ has maintained a stable configuration, with direct connection between all three ridges, for tens of millions of years.

Chapter 3: GIS analysis of rifting at the Northern Galápagos Triple Junction

3.1 GIS Database and Mapping Method

In order to compile a geospatial database of rifts found at the Northern GTJ (Figure 4), I utilized ESRI® ArcGIS software, a commercially available software package. ArcGIS is an integrated collection of GIS (Geographic Information Science) software products that provides a standardized platform for spatial analysis, data management, and mapping. Access to ArcGIS at the University of Maryland was possible through the Geography Department. Within the ArcGIS software package, I used ArcScene, an application of the ArcGIS 3D Analyst extension and a 3D raster GIS viewer.

ArcGIS is able to read an ASCII file containing x and y coordinates and association elevations z. The original GTJ gridded bathymetry data (.grd file) was converted into an ESRI ASCII using the GMT command:

> grd2xyz GTJbathymetry.grd -E > GTJbathymetry.asc

The ASCII file was then imported into ArcGIS and converted into a raster surface dataset. Projection for the map was defined as UTM Zone 14N and all coordinates are in decimal degrees. Points along the topographic volcanic highs of ridges and lows of rift valleys were defined in 3D using ArcScene. Polylines connecting points along the rifts and ridges were mapped in 2D. All points and lines mapped were saved as ESRI shapefiles and an exported as a database for Microsoft

Excel using ArcCatalog, an ArcGIS application that collects, stores, and manages GIS data.

The data that was mapped and collected is included in Appendix A. The associated shapefiles created in ArcGIS includes the spatial extent of abyssal hill fabric excluding the secondary rifts, the lengths of rifts/ridges, the exact coordinates of a point representing the western tip of each secondary rift, and the length between adjacent rift tips. Azimuths of the mapped rifts and the relative positions between adjacent rift tips were calculated using MATLAB. This last data is used to get a sense of the direction and magnitude of the rift jump from a disconnecting rift to a new crack forming along the EPR.

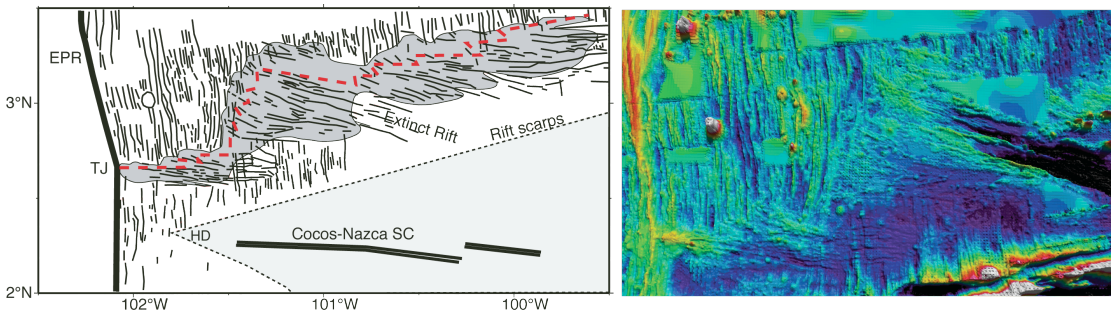

Figure 4. Map of the rifts and ridges found at the Northern Galápagos Triple Junction (Schouten et al., 2008) along with a 3D view of the topography using Fledermaus. Approximately 25 secondary rifts have been mapped to the northeast of the 2° 40' N triple junction and are into a Geographic Information Science spatial database found in Appendix A.

Once the coordinates of selected rifts were collected and organized into a database, I extracted the azimuth of the line linking adjacent rift tips and rift lengths. To calculate the azimuth between points on a sphere using MATLAB:

> az = azimuth(lat1,lon1,lat2,lon2)

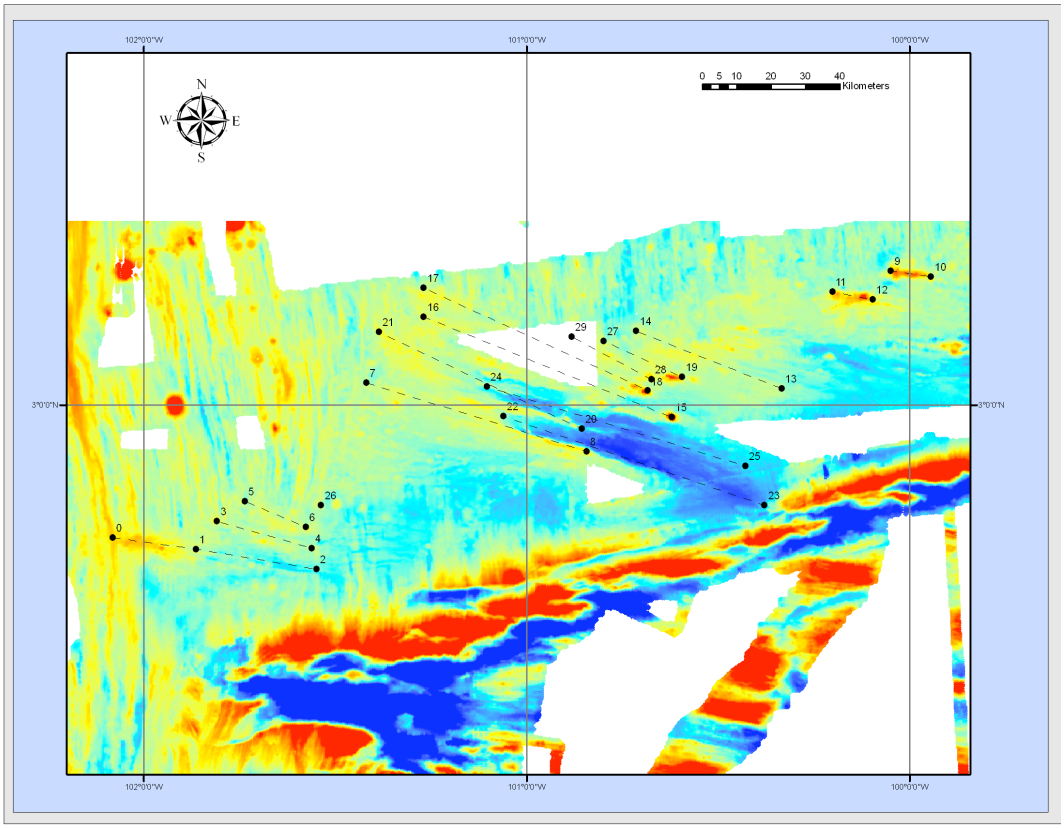

Figure 5. Screenshot of the 2D raster image of a selection of rifts mapped northeast of the 2°40' N RRR triple junction at the N. GTJ using ArcGIS software. Rifts are outlined with the dashed lines. Data on these rifts can be found in Appendix A.

3.2 Geospatial Analysis of Rifts

The analysis of several of the ~25 extinct secondary rifts found northeast of the 2°40' N triple junction and the compiled geospatial database of information regarding these extinct secondary rifts are used in the following sections to evaluate model predictions. Since the northwestern rift tip of the IR represents the current triple junction, the relative position of the northwestern tip from the adjacent rifts helps to constrain both the timing and the position of triple junction formation and timing of detachment. Analysis of rift azimuth, length, point of transition from ridge to rift were parameters measured using GIS.

Figure 5 shows a screenshot of the raster map of the Northern GTJ with the 15 rifts mapped by the dashed lines. Numbers indicate measured endpoints. Analysis of the current IR mapped between points 0 and 1 shows that this active rift is ~ 25 km long, topographically elevated, and strikes at ~ S99°E. This volcanic high transitions into a shallow rift valley that continues at the same azimuth for another ~ 35 km.

The youngest inactive rift found immediately to the northeast of the IR is mapped between points 3 and 4 (IR_1)(Figure 6). This rift follows as azimuth of ~ S106°E for ~ 29 km and is offset from point 0, the point representing the active triple junction proper along the EPR by a jump distance of 30.6 km and a jump azimuth of S261°W to the southwest. After this rift disconnected from the EPR, the current IR formation was "left-stepping" and will be further explained in the Section 4.2.

Similarly, the next youngest rift scar, mapped between points 5 and 6 (IR_2) is 19.3 km long and follows a similar azimuth of S111°E. The measured offset between IR_2's disconnection and IR_1's formation along the EPR is ~ 10 km with a jump to S237°W, another left-stepping rift. These data on rift jump distances and azimuths will be discussed in detail in Section 5.3 (see Figures 20-21).

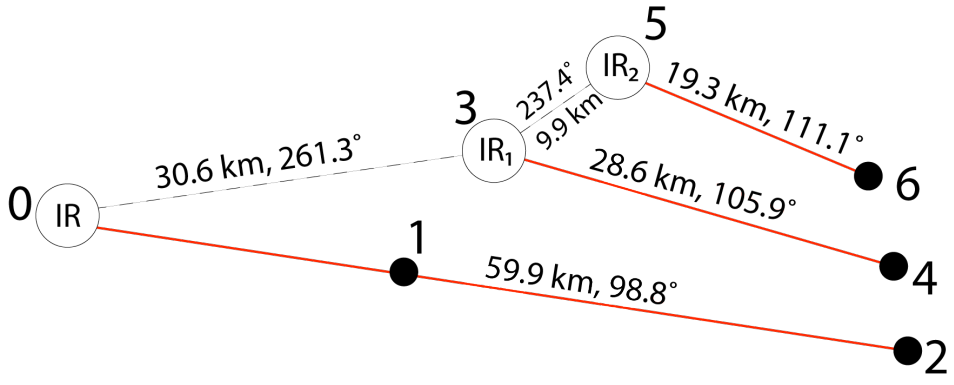

Figure 6. Relative positions of the Incipient Rift (Points 0-2) along with the most recently detached rifts found at the 2°40' N RRR triple junction showing the direction of rift-stepping.

Each of these mapped rifts follows a similar SE azimuth in the range of 95-117° whose azimuth frequency can bee seen in the histogram of rift azimuths in Figure 7. This similar trend for rifts can be attributed to its interaction with the presence of the CNR tip and will be further discussed in Section 5.4.

Figure 7. Histogram of rift azimuths mapped at the N. GTJ. Rift azimuths are fairly uniformly distributed in the range of 95-117°.

Chapter 4: Crack Interaction

4.1 Principles of Crack Interaction

Analysis of the rifts found at the N. GTJ can be understood through the concept of fracture mechanics. In essence, rifts can be modeled as cracks in an elastic plate and their stress interaction with other nearby cracks numerically and conceptually analyzed. During this study, I assumed a stress-free condition for rifts and modeled them as thin ellipses to explore the stress enhancements that develop along the major ridges.

Theoretical works involving the behavior of cracks within brittle solids – their inception, propagation, direction of propagation, and termination is rooted in the early works of Griffith (1920's) and Irwin (1940's). These early theoretical works formed the basis for the field of fracture mechanics, a field of study that relies on analytical and experimental methods to calculate crack propagation and the failure of specific materials. In particular, these studies analyzed stresses that developed around a crack's tip in response to a remote applied load.

A crack originally develops within a brittle material as a flaw, a microscopic defect within a material. These flaws control the specific strength or resistance to fracture of the material. Griffith recognized that flaws are present in most brittle materials and proposed that these flaws will grow into cracks and propagate when specific criteria are met.

Griffith proposed that cracks would propagate based on an energy – balance theory to describe conditional requirements for crack propagation. Griffith derived a critical stress that needs to be reached in order to drive the propagation of the crack:

$$\sigma_f = \sqrt{\frac{2E\gamma}{\pi c}} \qquad (1)$$

where E = Young's Modulus of the material
γ = the surface energy density of the material
c = crack length

The displacement field of a propagating crack can be divided into three modes or ways of applying a stress to a material in order to force a crack to propagate. Mode I cracking describes an opening mode where tensile stresses and the resulting displacement direction is normal to the plane of the crack. Mode II is a sliding mode where shearing occurs in the plane of the crack. A Mode III crack is a tearing mode where a shear stress acts parallel to both the plane of the crack and crack's edge.

The stress field surrounding the propagating crack tip determines the direction of crack propagation (see Figure 22) and is discussed in detail in Section 5.4. A Mode I crack will propagate in a direction normal to the direction of the principal tensile stress. In order to model crack propagation, the stress intensity factor must be calculated. This parameter depends on the applied load and orientation of the crack and describes the magnitude of the stress in the vicinity of the crack tip. When a uniform stress is applied to a crack, the stress intensity factor is defined as (for pure Mode I or Mode II):

$$K_I = \sigma_{yy}(\pi c)^{1/2}$$
$$K_{II} = \sigma_{xy}(\pi c)^{1/2} \qquad (2)$$

where σ_{yy} and σ_{xy} = the applied remote Mode I or Mode II stress.

In pure Mode I or Mode II stress loading, a crack will propagate when it reaches a critical stress value or fracture toughness, K_{Ic} (Mode I) or K_{IIc} (Mode II). This is a material-specific property that needs to be experimentally calculated through stress analysis. When $K_I > K_{Ic}$ (for Mode I), the crack will propagate in the direction that is normal to the direction of principal tension.

4.2 Rift Interaction Modeling Techniques

Schouten et al. (2008) proposed that the presence of the propagating CNR near the EPR influences the location and timing of secondary rift formation at the 2°40'N triple junction. The short-lived secondary rifts north of the Galápagos microplate were likely initiated from lithospheric cracking along the EPR at 2°40' N, but they rapidly ceased to be active, detached from the East Pacific Rise, and were carried away from the former triple junction with the northeast motion of the Cocos plate.

I developed numerical models in which the geometry and locations of rifts were varied in the general triple junction vicinity to constrain the factors that have led to the consistent location of secondary rifts at the northern triple junction. The modeling results indicate that once a rift has become detached from the East Pacific Rise, a zone of reduced tension forms at the rift tip prohibiting its reconnection. Two peaks of tensile stress enhancement develop along the East Pacific Rise and are offset from the detached rift indicating where a new crack is likely to form. In these models, the presence of the CNR, relative to the EPR, controls the location of new rift formation along the EPR. Therefore, I infer that the sequence of ancient rifts found

northeast of the current triple junction at 2°40’ N is a natural consequence of rift disconnection events and their relative positions records the kinematic history of the gap between the EPR and the CNR.

4.2.1 Modeling Method

Following the strategy of Schouten et al., (2008), each rift at the GTJ is represented by a stress-free crack embedded in a thin elastic plate. Plate motion puts these cracks under tension. However, unlike Schouten et al., (2008), I include all the rifts currently active at the Northern GTJ: the EPR, the CNR, and the IR, which leads to complex stress interaction. I solve numerically for the stress enhancement field that results from these cracks when under tension to determine where new cracks, and therefore new rifts, may form, using the commercial Finite Element software COMSOL Multiphysics®.

4.2.2 CNR Base Model Design

A fundamental length scale present in this problem is the distance between the EPR and the tip of the CNR, $D \sim 50$ km. In the model, all dimensions are scaled by D. The computation domain is composed of a rectangular elastic plate measuring $6D$ in the E-W direction and $8D$ in the N-S direction, with a thickness of $0.2D$. The western edge of the model is a stress-free boundary representing the EPR. Other rifts are represented by thin ellipses with a semi-minor axis of length $0.002D$. All the models discussed here include an ellipse representing the CNR. It splits the model horizontally from its eastern edge to a distance D from the EPR. Although the region north of that crack corresponds to the Cocos plate and the region south of the crack

represents the Nazca plate, the plate is continuous around the rift tip, where the Galápagos Microplate is located. When included, the IR and other secondary rifts are represented by additional thin stress-free ellipses. Their length and position are varied in this study to characterize the stress pattern due to stress interaction between the rifts. The plate is meshed using Delaunay triangulation, with increased resolution along the EPR and rift tips.

At the GTJ, the EPR opens at 133 mm/yr and the CNR at 42 mm/yr (DeMets et al., 1994). Spreading rates described above and used for the modeling are obtained from Bill Menke's online plate velocity calculator. The model is loaded by imposing the displacement on the northern, southern, and eastern boundaries of the model that corresponds to an arbitrary time, δt. Because the EPR cuts the entire left boundary of the model, only the opening of the CNR induces stresses in this model. In the absence of cracks other than the EPR, this motion would produce a uniform stress of $\sigma_0=2E^*d/L_y$, where E is the Young's modulus, d is the displacement at the north and the south end of the model, and $L_y=8$ is length of the model plate in the y direction. The stress field produced in the presence of rifts is scaled by σ_0 to produce of a map of the stress enhancement, $S=\sigma/\sigma_0$, produced by the rifts. For simplicity, I solve directly for the stress enhancement map by imposing $E=1$, and $d=L_y/2=4$. Studying the stress enhancement field suffices to determine the location of future cracks in the models. I study specifically the profile of stress enhancement along the model EPR to determine where rifts may be generated.

Four model series were developed (Figure 8). The first aims at reproducing the model of Schouten et al. (2008). This reference model incorporates only the CNR

ellipse. The second model series (Attached IR) also includes a smaller ellipse of length 0.4*D* to represent the active IR. The position of the smaller crack along the EPR, d_y, is varied in order to get a sense of how the tensile stress amplitude and peak position are affected by the position of the secondary crack. The last model series (Detached IR) includes a gap of 0.2*D* or 0.1*D* between the EPR and tip of the crack representing the IR. These models are used to constrain where along the EPR a new triple junction will form if the IR is no longer connected with the EPR. These models are analyzed to understand how the magnitude of the gap between the IR tip and EPR influences stress enhancement along the ridge.

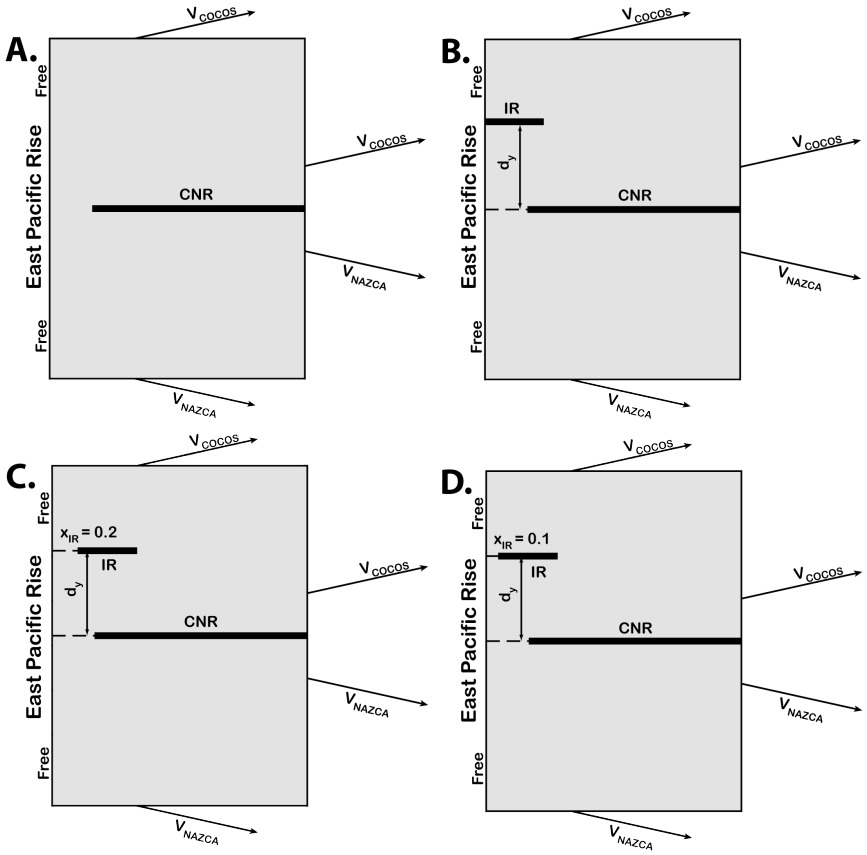

Figure 8. Schematics of the numerical models used in the rift interaction study. A: Reference model in which only the EPR and the CNR are included. B: Addition of an IR-like crack connected to the EPR (attached rift), representing the current configuration of the Northern GTJ. C: Model series where the IR is detached by a distance of 0.2*D* and moved north along the EPR. D: Similar model series but with the distance between the detached IR tip and the EPR decreased to 0.1. Models have dimensions of 6x8.

4.2.3 Modeling Theory – Model Boundary and Scaling Study

To validate the model geometry, I varied the dimensions of the rectangular base of the model while holding the distance from the CNR tip to the point directly ahead of the tip along the EPR constant. Figure 9 shows stress profiles taken along the western stress-free boundary of the model (EPR) with the presence of the CNR tip at a distance of 1 (*D*) from the boundary with various model widths ranging from 2 to 12. A model width of 6 is used for the base model and is shown in Figure 9 by the bold black line. When the width is 6 and above, consistent stress profiles are calculated and suggest that the width of 6 is sufficient for the models.

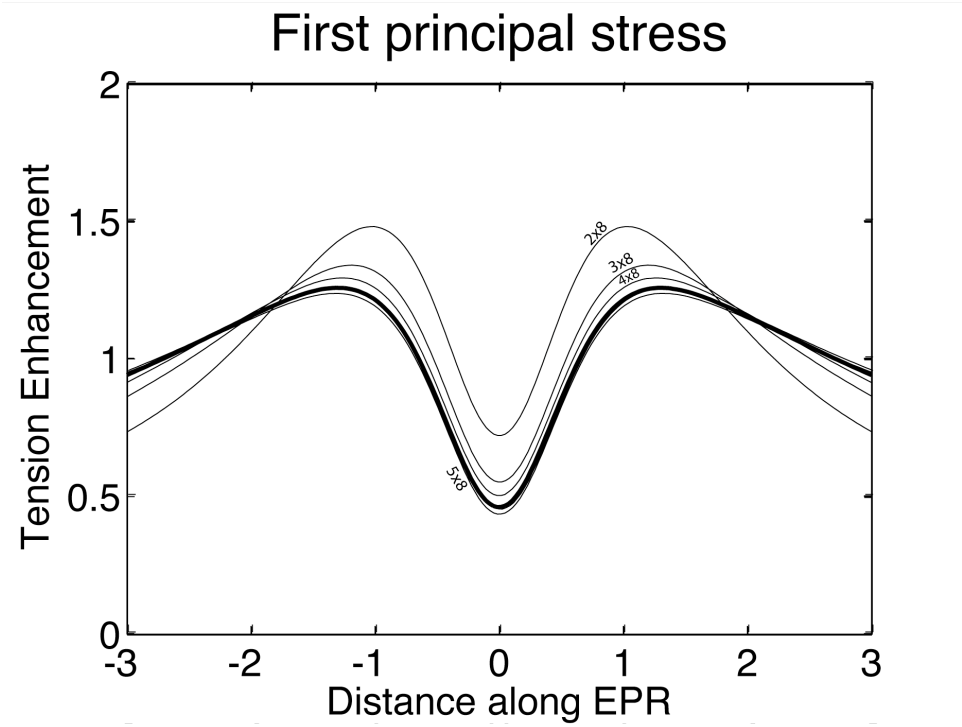

Figure 9. Tension enhancement profiles for various widths of the base model that includes the CNR-ellipse only. The stress profile for the base model dimensions of 6 (width) x 8 (length) is shown by the bold black line with maxima occurring at ± 1.35 and a stress minimum at 0. Profiles with width values of 7, 8, and 12 are overlain on 6x8 profile and show that model widths with vales of > 6 provide consistent similar results indicating model integrity.

In Figure 10, tension enhancement profiles are shown with varied length dimensions. Again, the bold black line highlights the base model dimensions of 6x8. The models with lengths of 7 and above provided consistent profiles with dual maxima peaks of similar amplitude and position along the EPR western edge of the model boundary, although the intensity of peak increases as model length increases beyond 7. This effect of model boundaries is predicted from crack mechanics. Thus, I cannot interpret the absolute value of the peak magnitude, only its position and its relative magnitude between models.

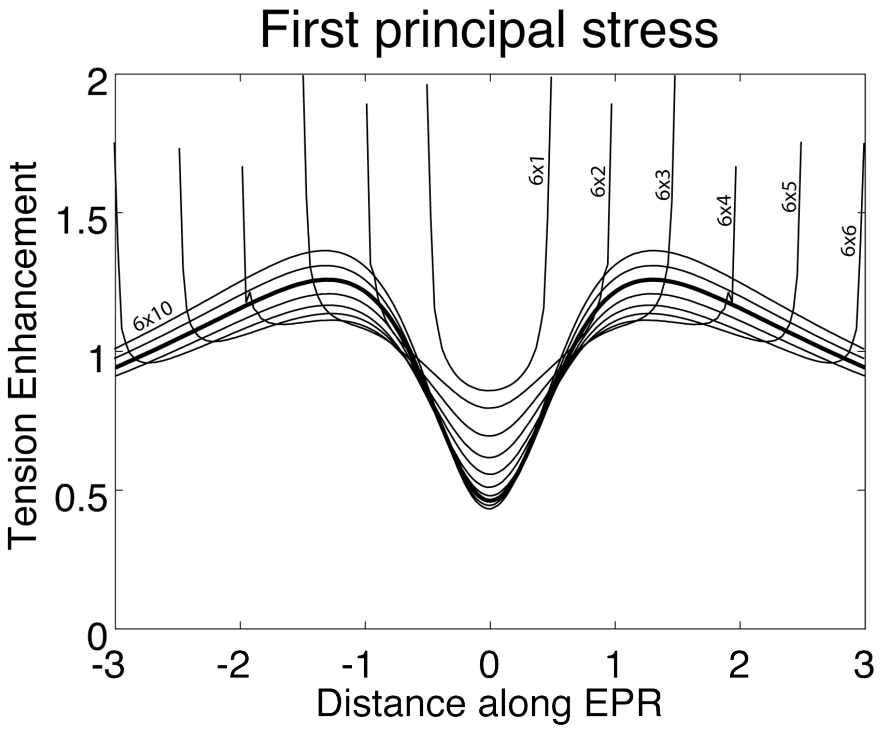

Figure 10. Stress enhancement profiles for models with various lengths. The bold line shows the profile for the base model with dimensions of 6x8. Overlay profile suggests that models with lengths over 7 provide consistent and reliable results.

The models used in the study have a CNR-like ellipse with a width (semi-minor axis) of 0.002. To test the effect of ellipses with various widths, I ran the models varying the CNR-like ellipse with values of 0.0001, 0.001, 0.002, 0.01, 0.1

and 1. The results of this modeling study can be seen in Appendix B. Assigning these various ellipse widths did not significantly affect the values of tensile enhancement amplitude and position. The only noticeable change is not in the max amplitude, but in the low amplitude at 0. Increasing the width of the CNR increases the compression at 0.

4.2.4 Analysis of Uncertainty

To characterize the uncertainties and validate the numerical models, I increased the resolution of the mesh of two example models (Figure 11) and analyzed how the values of the maximum stress enhancement were affected. The first model is the base model that has one rift tip far enough away from the EPR (stress-free surface that is being analyzed) and the other contains a detached rift whose refined element mesh has an influence over the EPR. The grid size contained within the script is adjusted along the stress-free EPR in order to increase the resolution of the mesh. Specific values of stress enhancement from these refined element meshes are extracted and compared to the models used in the research to estimate uncertainty.

For the model that has only the CNR (Figure 11A), I observe that the peak position has a calculated uncertainty of 1.3 ± 0.2 when it is measured against the maximum mesh size and that the peak amplitude has a calculated uncertainty of 1.259 ± 0.002 when measured against the maximum mesh size (Figure 12). The vertical line in each graph represents the mesh size (0.06) that was chosen for the models and is sufficient for accuracy.

For the model that has both the CNR and IR (Figure 11B), mesh refinement due to the addition of the IR increases along the EPR. This mesh refinement increases

the accuracy of the tensile stress maxima calculations; therefore, the uncertainties are even less for the models that include secondary rift additions.

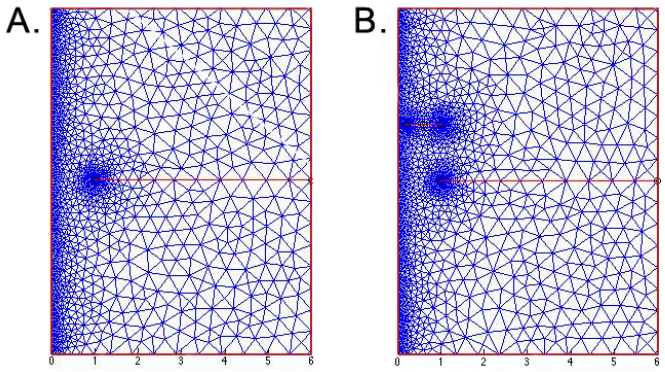

Figure 11. Model mesh resolutions used in the study. A: The mesh with a resolution of 0.06 for the model without the influence of a secondary rift mesh refinement. Uncertainty for this mesh resolution corresponds to the vertical line in Figure 12. B: The mesh with a resolution of 0.06 for the model with the influence of a secondary rift refinement.

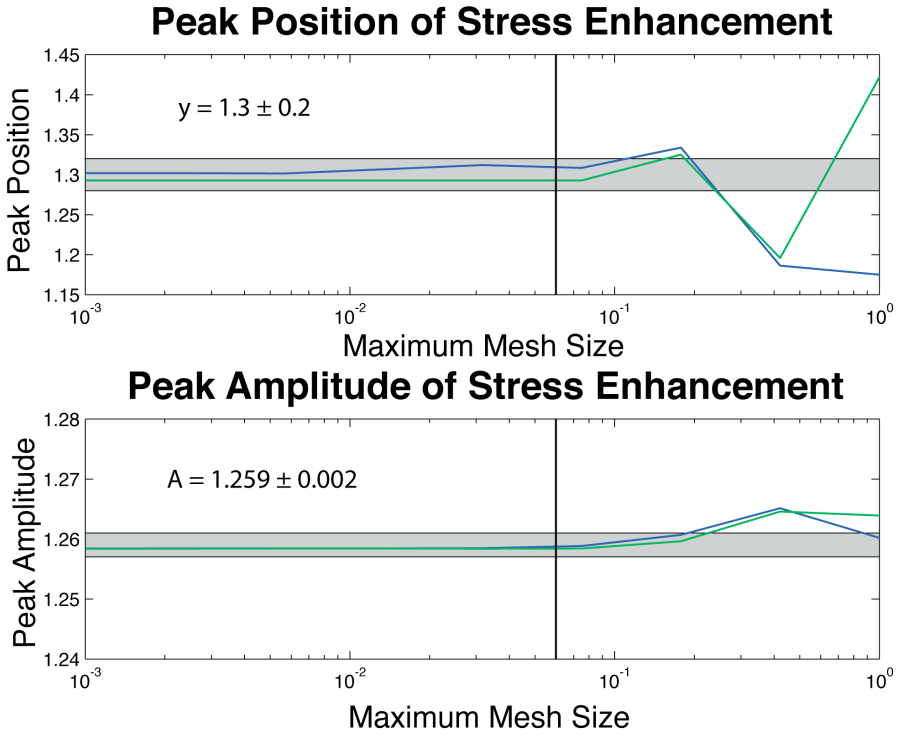

Figure 12. Values of the peak position when measured against maximum mesh size without the influence of a secondary rift. Uncertainty of the measured peak position is calculated to be 1.3 ± 0.2. Calculated uncertainty is 1.259 ± 0.002 of the peak amplitude when measured against the maximum mesh size. The vertical line in each graph shows the mesh size of 0.06 used in the models The gray area represents the uncertainty in each measurement, blue line is the south peak, and green line is north peak.

4.2.5 Goals of the Study

The motivation behind this research is to examine the apparent instability of the N. GTJ RRR triple junction and to better understand how stresses associated with the location of the CNR control the location and timing of secondary rift formation at the 2°40' N triple junction. I propose that the location of rift formation along the EPR is due to the interaction between the presence of the CNR and its distance from the EPR.

A second aim of this research is to examine the stability of these stable triple junctions – mainly why the GTJ lacks a direct connection and has a history of unstable secondary rifting while the RTJ appears to be directly connected and kinematically stable. I propose that the angle between the major ridges involved in the RRR triple junction control the stability. A RRR triple junction's geometry can either promote a connection (as in the RTJ case) or prohibit a connection (as in the GTJ case).

Chapter 5.1 and 5.2 describes the work I conducted for my undergraduate senior thesis concerning the formation of secondary rifts at the GTJ. This project was complemented by further models on rift offsets and geospatial analysis of the relative positions of secondary rifts found North of the CNR in Section 5.3. An analysis of the direction of crack propagation to determine whether the azimuth of these rifts is also a direct consequence of crack mechanics is presented in Section 5.4. Chapter 6 presents the study of the effect of ridge azimuth on triple junction stability, which is used to explain the different stability of the RTJ and GTJ. These models are applied to the study areas at the GTJ and RTJ in Chapter 7.

Chapter 5: Modeling the Northern Galápagos Triple Junction

Stress enhancement maps and profiles taken along the EPR are presented in Figures 13 and 14 for various rift configurations. If crack nucleation follows a critical stress criterion, the first crack to nucleate along the EPR will be located where stress enhancement is highest. A map of the tensile stress enhancement in the presence of the CNR but without a secondary rift is presented in Figure 13A. The resulting pattern is similar to previous geodynamic modeling of the GTJ presented in Schouten et al., (2008). The stress field is symmetrical with respect to the CNR. Directly ahead of the CNR tip, a region of reduced tension develops and two symmetric peaks of tensile stress enhancement form approximately at ± 1.35*D* along the EPR stress-free boundary (Figure 14). The location of the IR corresponds closely to the stress enhancement peaks (Schouten et al, 2008). The region of reduced tension acts as a barrier preventing the CNR from connecting to the EPR. This tension becomes more intense as the gap between the EPR and the CNR decreases.

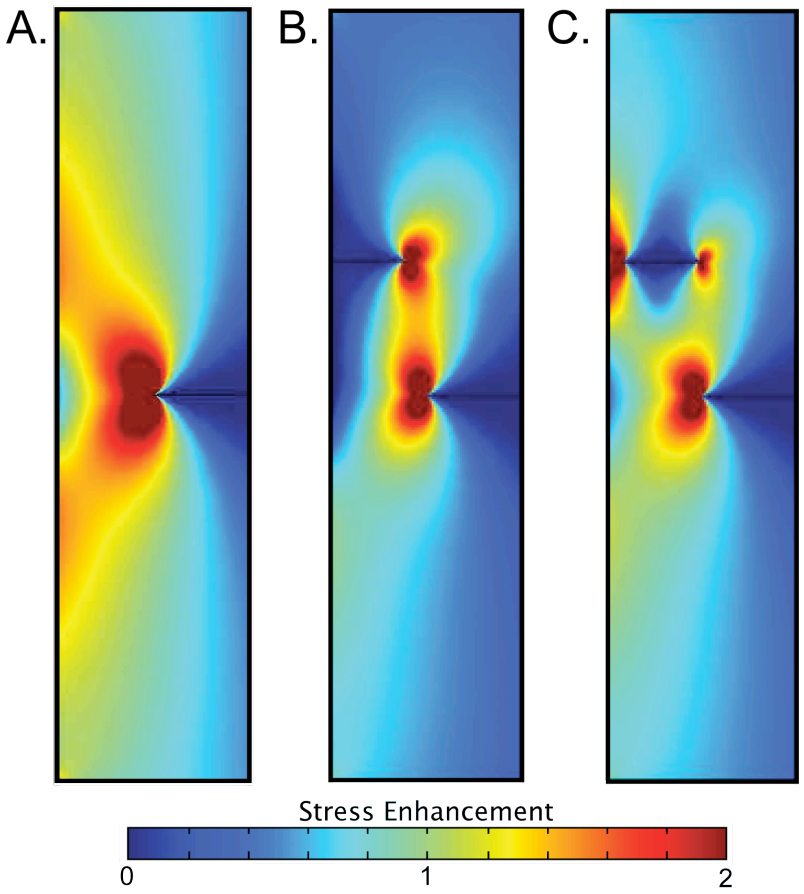

Figure 13. Maps of tension enhancement along the East Pacific Rise. A: Tensile stress field in the presence of the CNR only. Reduced tension forms directly ahead of the CNR tip on the EPR and off-axis peaks of tensile stress maxima occur approximately at ± 1.35*D*, where *D* is the length of the gap between the CNR and EPR. B: Attached IR at 1.4*D* along the EPR. Tensile stresses are released along much of the EPR boundary. C: Detached IR near 1.4*D* along the EPR. A zone of reduced tension develops at the tip of the secondary rift and prohibits its reconnection with the EPR. Two peaks of tension enhancement develop, offset from the detached rift. The new rift is assumed to form at the higher of the two peaks as a result.

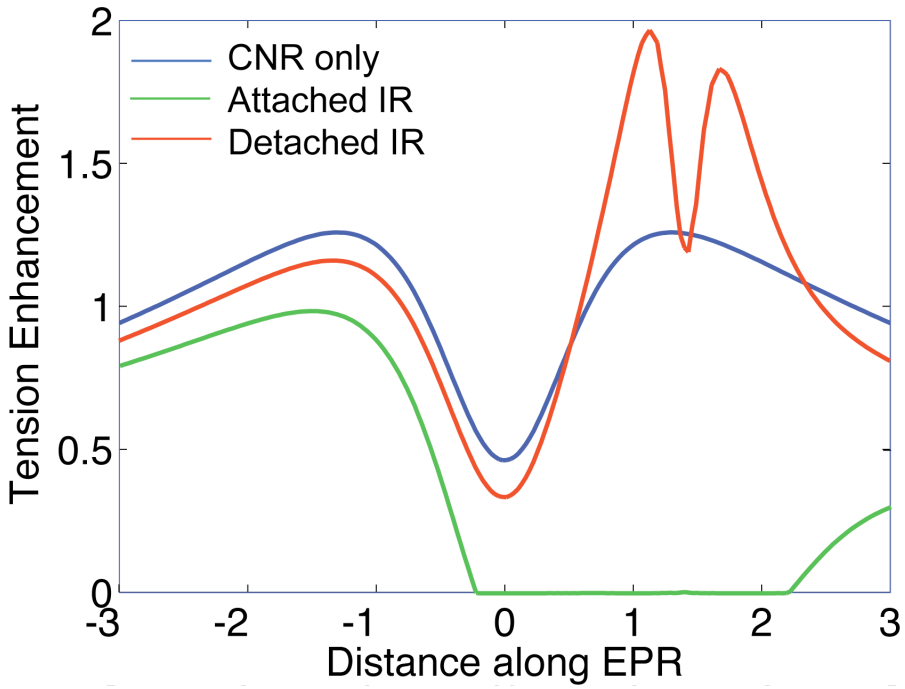

Figure 14. Stress enhancement profiles for the three models of Figure 13: the CNR only reference model (blue), the Attached IR model where d_y = 1.4 (green), and the Detached IR model where d_y= 1.4 and x_{IR} = 0.2 (red). When the IR is detached from the EPR, asymmetrical double peaks of stress enhancement form with a zone of reduced tension at the disconnected rift tip. This model predicts that a new rift will form to the south of the detached rift's position along the EPR.

5.1 Attached IR Model Series

When the IR is added into the model as a connected secondary rift the tensile stress decreases along the length of the EPR in a wide region centered at the triple junction. The resulting stress pattern is asymmetric as a secondary rift is included only to the North of the CNR (Figure 13B and its corresponding stress profile in Figure 14). Figure 15 reports the location and intensity of the northern and southern stress enhancement peaks as the location of the secondary rift along the EPR is varied. If the secondary rift is close to the projection of the CNR, its effect on the southern stress enhancement maximum is to reduce its amplitude and to displace it somewhat towards the South along the EPR. As the secondary rift is moved

northward along the EPR, closer to its observed position, it has less and less influence over the southern peak, so that the peak's regain its original position along the EPR and its amplitude. Eventually, the triple junction will have moved far enough North and will no longer significantly affect the stress pattern between the EPR and the tip of the CNR. After the IR has moved too far North, the northern peak will resume a similar position and amplitude to that of the northern peak in the reference model.

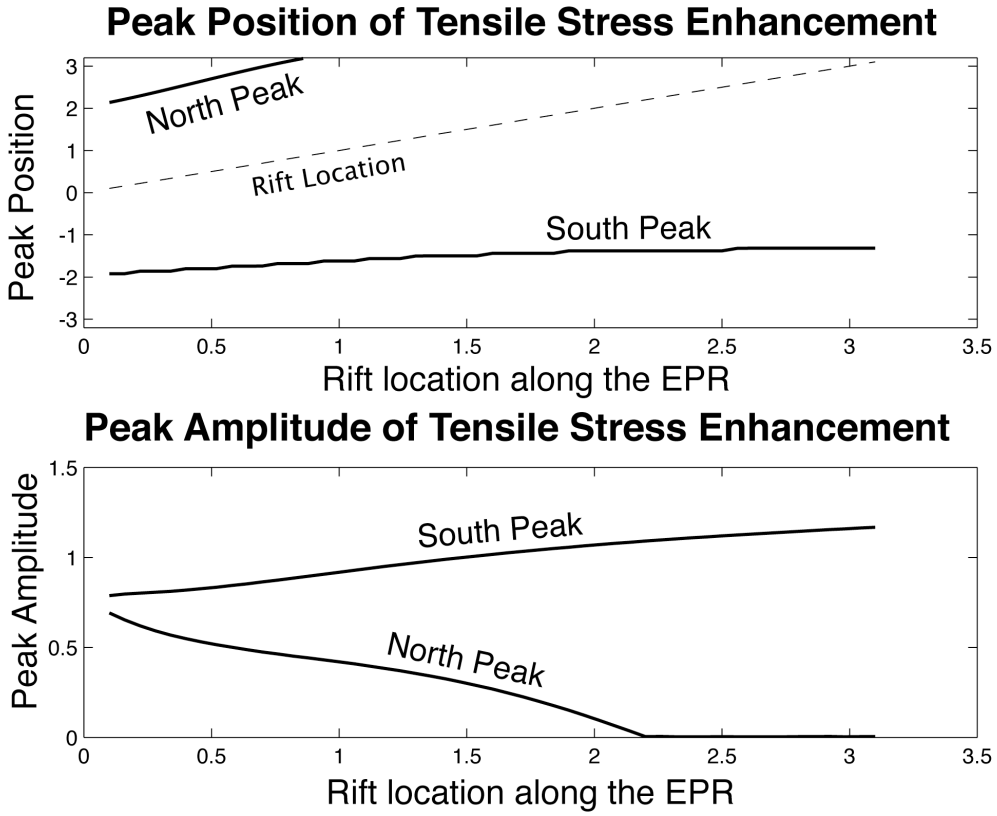

Figure 15. Position and amplitude of the stress enhancement peaks along the EPR in the Attached IR model series. The presence of a secondary rift releases tensile stress in the area of the triple junction. Both the position and amplitude of the stresses return along the ridge with values similar to the reference model after the IR has moved too far north to have an influence.

5.2 Detached IR Model Series

When the secondary rift is detached from the EPR, a strong, local pattern of stress enhancement is generated along the EPR. The stress profile is similar to that

seen in the reference model, but occurs over a smaller length scale, that of the gap between the EPR and the tip of the secondary rift. A zone of stress reduction fringed by two peaks of stress enhancement develops ahead of the detached rift tip. The zone of stress reduction along the EPR prevents reconnection of the secondary rift along the EPR. Instead, a new rift will nucleate at one of the two peaks of stress enhancement. The local double peak of stress enhancement that forms ahead of the secondary rift tip is asymmetric. In the example of Figure 14, the southern peak is slightly greater in amplitude than the northern, which suggests that the new rift will form offset to the south from the detached rift: a left-stepping rift sequence.

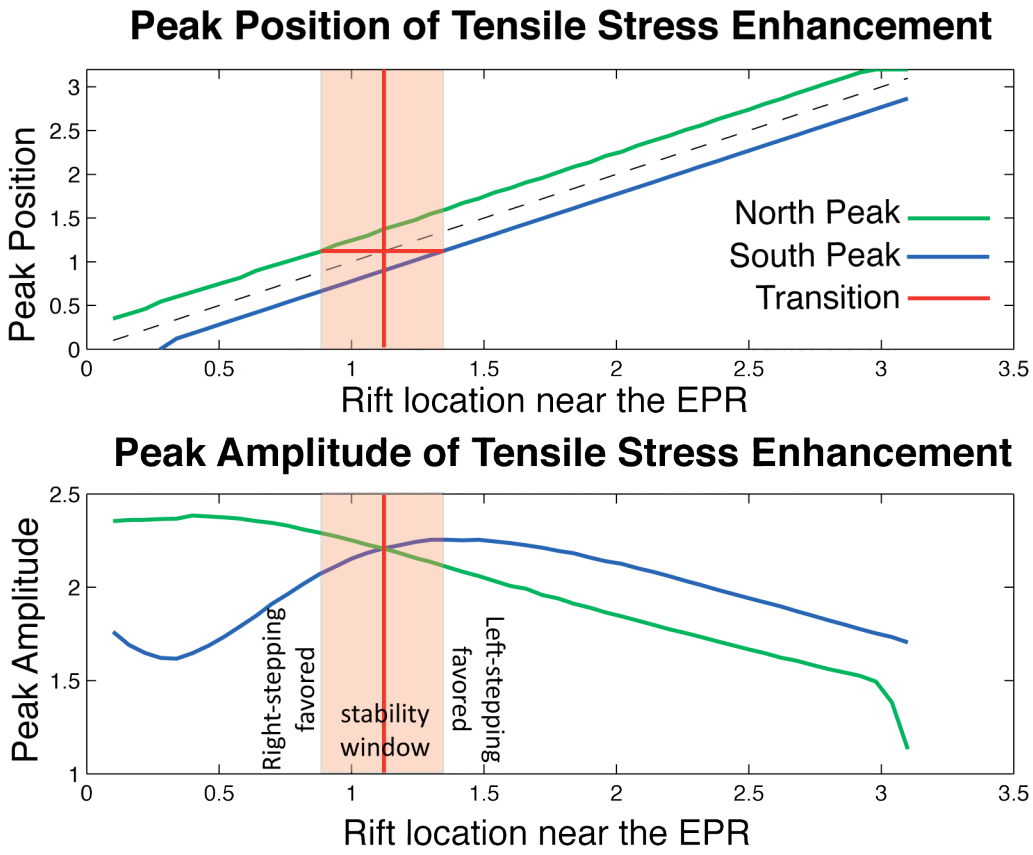

Figure 16. Results from the Detached IR model series when the gap between the EPR stress-free boundary and the IR is 0.2*D*. A rift detaching before 1.13*D* near the EPR (red vertical line), will have a higher northern peak and will form a right-stepping rift sequence. A detached rift North of this critical location will form a left-stepping rift instead. Within 0.22 of 1.13*D*, rift jumps will oscillate between right and left-stepping sequences without long-term drift. I refer to this region as the "stability window".

Figure 16 shows the effect of changing the position of the secondary rift along the EPR, keeping the gap between the EPR and the secondary rift tip at 0.2*D*. The two stress enhancement peaks follow the location of the secondary rift, and the distance between the two peaks remains approximately constant. However, the sense of the asymmetry between the peaks, that is, which of the two peaks is largest, depends on the position of the secondary rift along the EPR. North of a "Stability Window", the next rift is slightly to the South of the previous rift, a left-stepping sequence. South of the same stability window, the next rift is slightly to the North of the previous rift, a right-stepping sequence. Inside the window, rifts alternate between right- and left-stepping, with no long-term migration. Thus, the stability window serves as an attractor for the position of secondary rifts. Its location is controlled by the gap between the CNR and EPR, and its width by the gap between the newly detached rift and the EPR. It is centered at 1.13*D* when that gap is 0.2*D* (Figure 16). When x_{IR} is decreased to 0.1*D*, the zone of peak symmetry is centered at 1.07*D* (Figure 17).

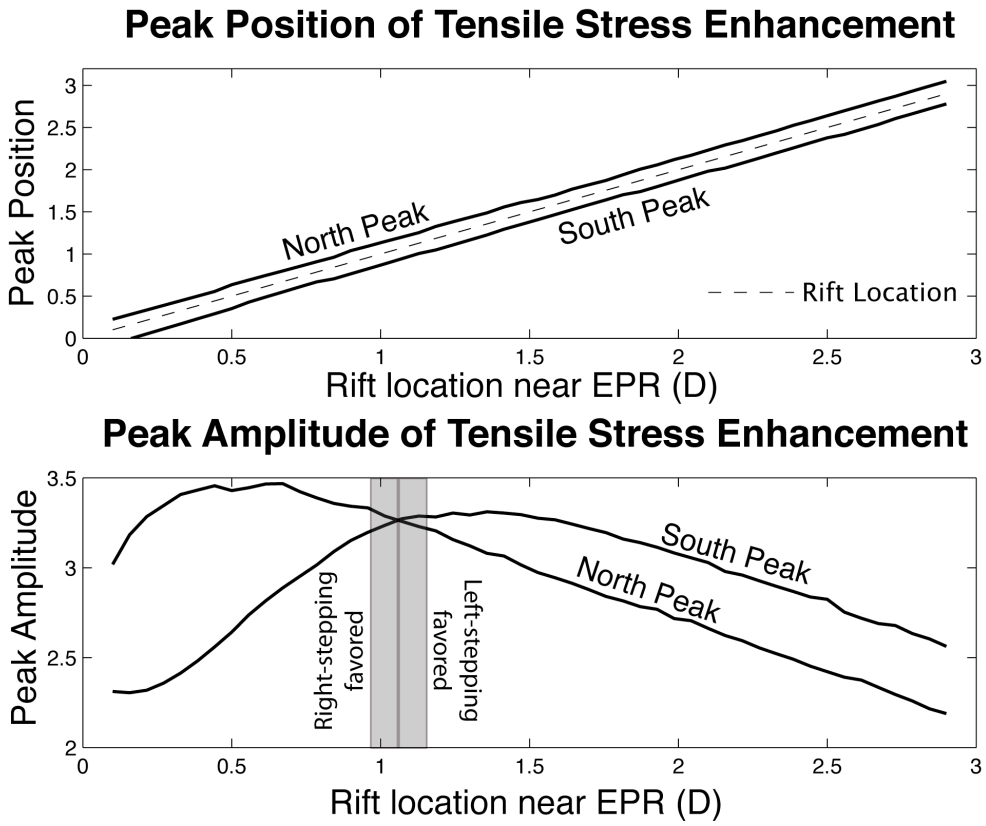

Figure 17. Results for the Detached IR model series when the gap between the IR rift tip and EPR stress-free boundary is decreased to 0.1*D*. A similar pattern to the Detached IR model series when x_{IR} = 0.2*D* develops. The above graph shows that the zone of peak amplitude symmetry occurs at 1.07*D* ± 0.13 when x_{IR} = 0.1*D*.

5.3 Controls on Rift Offset

My previously described rift interaction modeling study involving rift interaction at the Northern GTJ showed that where rifts detach from the EPR directly determines where the future rifts will form. Figure 16 indicates that when the secondary rift is less than 1.13*D* from the projection of the CNR along the EPR, the northern peak has the higher amplitude, resulting in a right-stepping rift sequence. Conversely, when the secondary rift is further North than 1.13*D*, the southern peak has the higher amplitude leading to a left-stepping sequence.

When the distance of the gap between the EPR and the tip of the detached secondary rift is decreased to 0.1*D* as shown in Figure 17, a similar result is observed, with two minor differences: the distance between the two peaks decreases, and the transition from right-stepping to left-stepping rifts takes place at 1.07*D* rather than 1.13*D*. Figure 18 shows how the magnitude of the gap between the IR tip and the EPR (x_{IR}) affects the position of peak tensile stress symmetry along the EPR. Also, the intensity of the local stress enhancement pattern increases, confirming the inverse correlation between the gap between rifts and the intensity of stress enhancement observed in the reference model. The calculated stress magnitude is a direct function of the distance to the tip of the IR crack ellipse, whereas the intensity pattern is a function of crack location (Shah and Kobayashi, 1973).

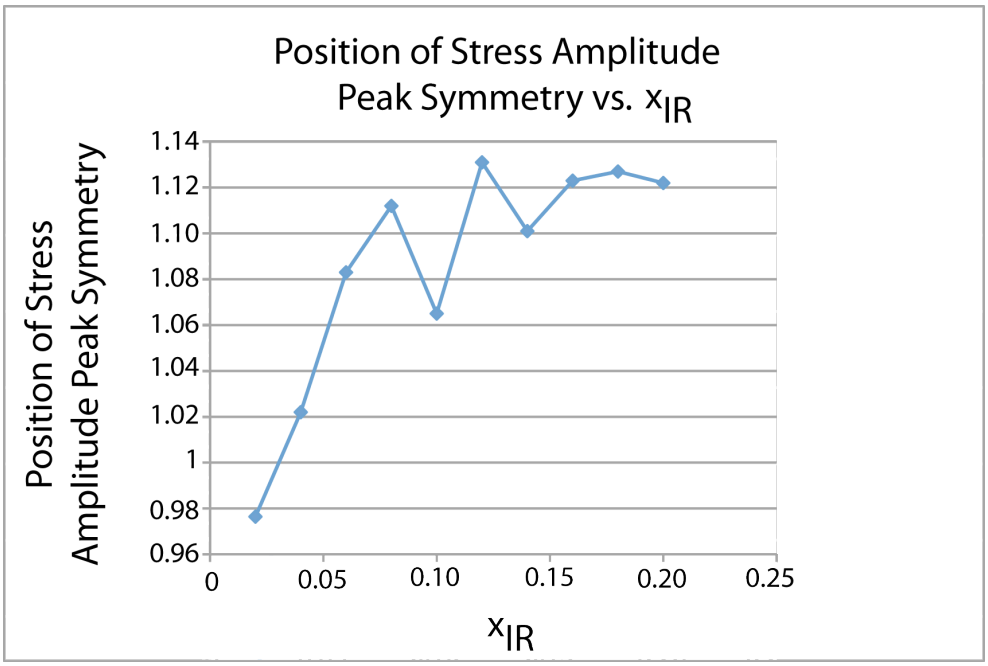

Figure 18. Graph of the position of double peak symmetry occurs as a function of rift detachment distance from the EPR. As the gap between the detached rift tip and the EPR widens, the dual peak symmetry or center of the oscillation window moves north along the EPR.

An outstanding question that remains to be determined is what is controlling the offset distance between the detached rift and crack formation along the EPR. The GIS analysis reveals the typical distances between detached rift tips range between 10 and 45 km with the majority of offset distance being < 20 km (Figure 20) with jump azimuths to Southwest (Figure 21). The actual detachment gap can only be smaller than the observed jump, projected normal to the plate separation direction because of possible westward propagation of the rift (Lonsdale, 1988; Lonsdale et al., 1992; Klein et al., 2005). The geospatial database implies that x_{IR} is smaller than 0.1, corresponding to a stability window 0.1*D* wide, centered at 1.1*D*. The offset distance between rift tips will provide the timing between detachment episodes, and therefore a temporal aspect of the kinematic evolution of the N. GTJ tectonics.

Figure 18 shows how the gap between the detached rift and the EPR are related to where the center of these stability windows will occur. Because there is a finite offset between parent and daughter rift, the product of a right-stepping event may be in the region where it will generate a left-stepping rift, and vice versa. In this case the detaching rifts produce alternatively left and right offsets with little or no long-term secondary rift migration. If the CNR tip is at a distance *D* from the EPR and the distance from the detached rift and EPR is 0.2*D*, the stability window is located between 0.91*D* and 1.35*D* (Figure 16). If the distance between the detached rift and the EPR is only 0.1*D*, the window is narrower and closer to the projection of the CNR along the EPR, from 0.94*D* to 1.20*D* (Figure 17). Thus, the distance between the detached rift tip and the EPR influences the width of the rift stability window (Figure 19) and the magnitude of stress enhancement while the regional

stress field, created by the presence of the CNR tip, controls its overall location along the EPR. The 1-1 relationship between the gap and width of the oscillation window suggests that the farther away the detached rift tip is, the closer the new rift will form to its predecessor.

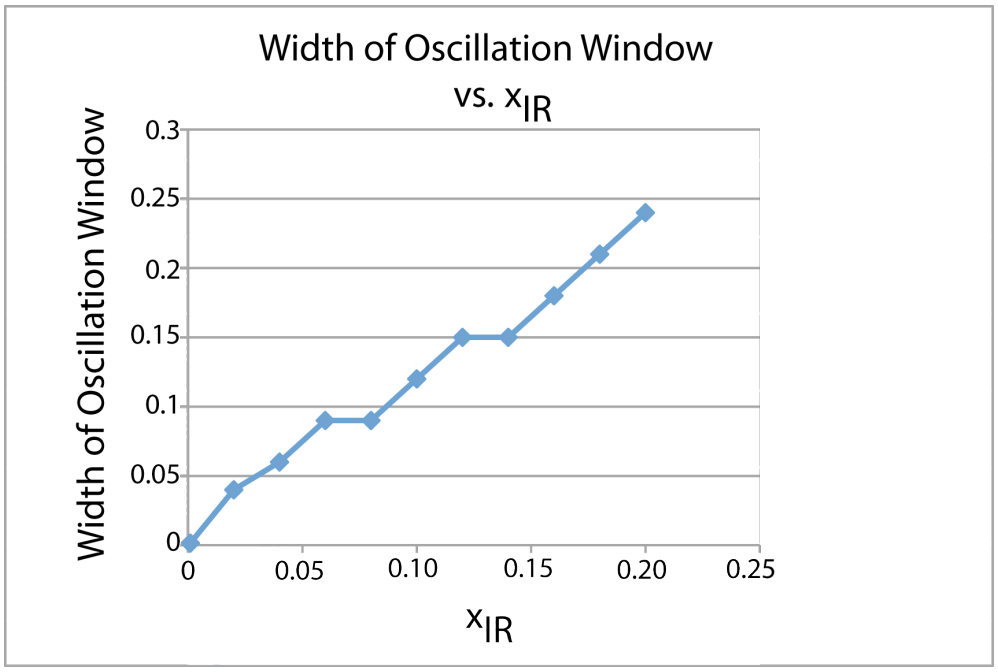

Figure 19. Graph of the width of the oscillation or stability window as a function of x_{IR}, the distance from the detached rift tip to the EPR. When the gap is increased the width of the oscillation window becomes larger and rifts detaching within this window will show little or no long-term migration from the original detachment point.

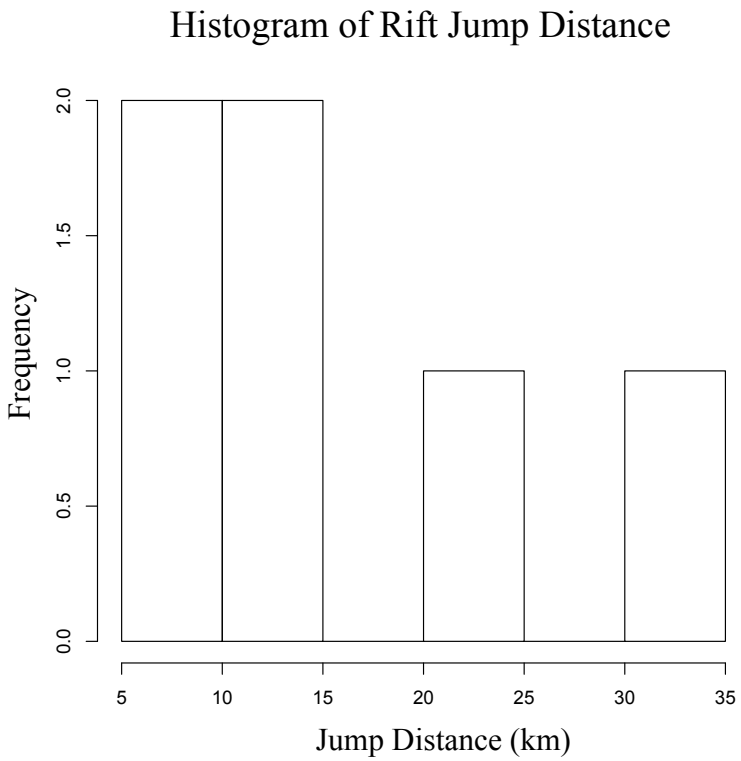

Figure 20. Histogram for rift offsets obtained from GIS analysis. The histogram shows that the majority of these adjacent extinct secondary rifts have offsets of < 20 km.

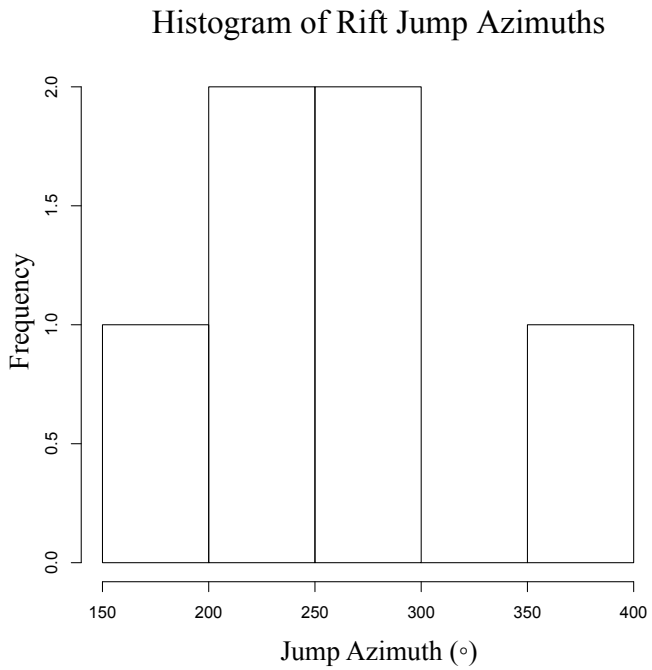

Figure 21. Histogram for the direction of rift detachment with a new rift formation along the EPR. These data show that the majority of these rifts are detaching North of the proposed stability window and jumping to the Southwest as a result. Rifts jumping to the Northwest are detaching South of the rift's specific stability window.

5.4 Propagation Direction of Secondary Rifts

Prediction of the propagation direction of a crack requires knowledge of the stress field surrounding the crack tip. This stress field in the vicinity of the crack's tip is a function of applied load, crack geometry, the distance from the crack tip (r), and angle with respect to the plane of the crack (θ). Figure 22a shows the geometry of a crack along with its rectangular and polar coordinates and Figure 22b shows the stresses around the tip of a Mode I crack, given by:

$$\sigma_{ij} = K_I (2\pi r)^{-1/2} f_{ij}(\theta) \tag{3}$$

where

$$\begin{aligned} f_{xx} &= \cos(\frac{\theta}{2})[1 - \sin(\frac{\theta}{2})\sin(\frac{3\theta}{2})] \\ f_{yy} &= \cos(\frac{\theta}{2})[1 + \sin(\frac{\theta}{2})\sin(\frac{3\theta}{2})] \\ f_{xy} &= \sin(\frac{\theta}{2})\cos(\frac{\theta}{2})\cos(\frac{3\theta}{2}) \end{aligned} \tag{4}$$

The stress field in the vicinity of a crack under mixed-mode loading can be described with the following expressions:

$$\begin{aligned} \sigma_r &= (2\pi r)^{-1/2}\cos(\frac{\theta}{2})[K_1(1 + \sin^2(\frac{\theta}{2})) + K_{II}(\frac{3}{2}\sin\theta - 2\tan^2(\frac{\theta}{2}))] \\ \sigma_\theta &= (2\pi r)^{-1/2}\cos(\frac{\theta}{2})[K_1\cos(\frac{\theta}{2}) - \frac{3}{2}K_{II}\sin\theta] \\ \tau_{r\theta} &= (2\pi r)^{-1/2}\cos(\frac{\theta}{2})[K_1\sin\theta + K_{II}(3\cos\theta - 1)] \end{aligned} \tag{5}$$

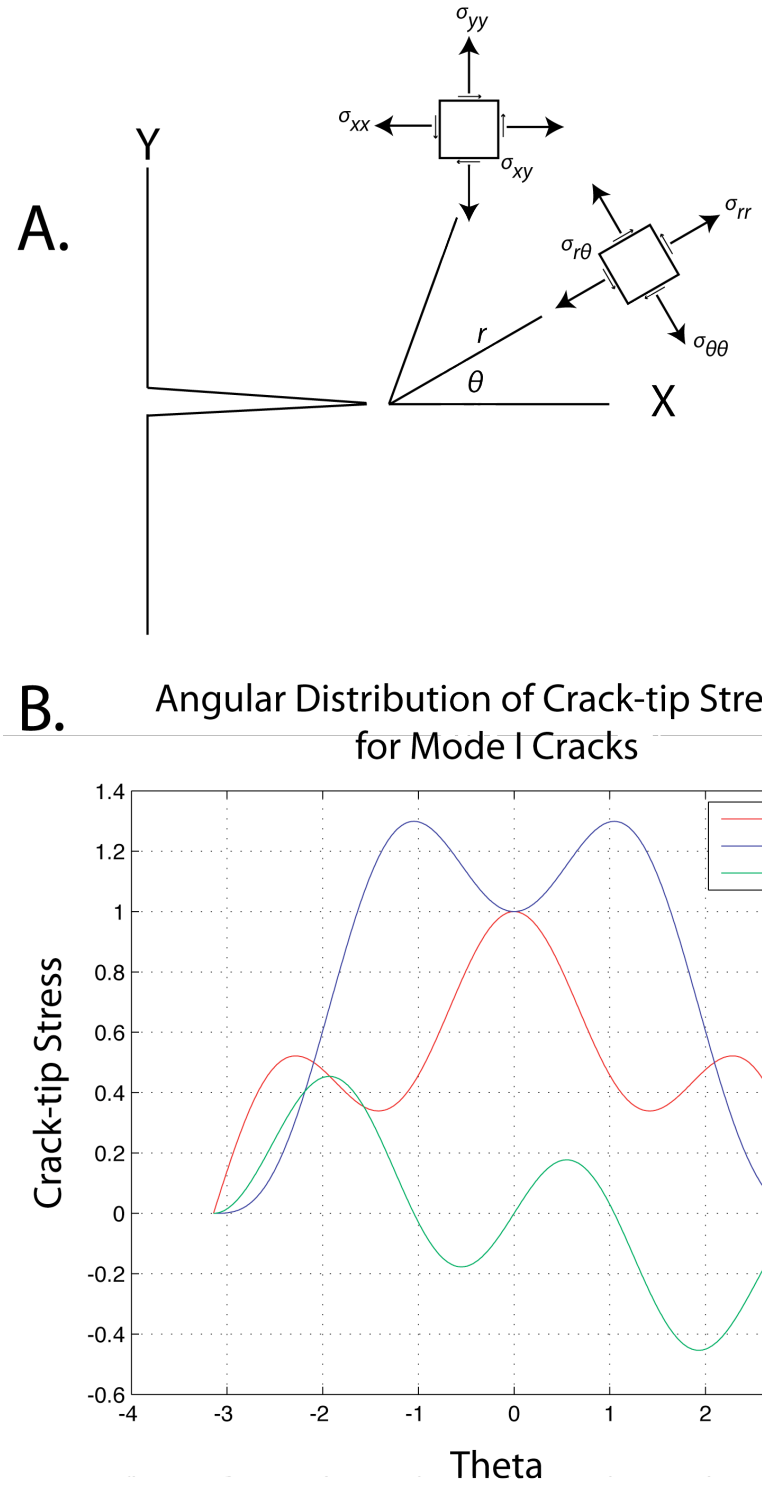

Figure 22. A. Stress field of a Mode I crack with polar and rectangular coordinates. From Lawn, 1993. B. Angular distributions of the stresses that develop at the crack tip for a crack undergoing Mode I cracking or tensile opening. The graphed stress functions are given in Equation 3 and 4 in Section 4.4.

A crack may propagate in response to a mixed-mode or combined mode loading. Several theories have been proposed to describe mixed-mode crack propagation. Erdogan and Sih (1963) proposed a maximum circumferential or tangential stress criterion (also referred to as the hoop stress or $\sigma\theta_{max}$ theory in literature) to account for mixed-mode crack propagation. This theory states that under slow applied mixed-mode loads, crack extension: 1) starts at the crack tip in a radial direction 2) starts in a plane normal to the direction of principal direction (where $\tau_{r\theta} = 0$) and 3) begins when $\sigma_{\theta\theta}$ reaches a critical value, specific to the material. These statements imply that the crack will propagate in a radial direction where the tangential stress is at a maximum and there is no shear stress.

A second mixed-mode cracking theory was proposed by Sih (1974). This theory, the $S\theta_{min}$ theory, describes crack growth in terms of a critical value of the strain-energy-density factor, S_{cr}. The theorem states that when the strain-energy-density, S, reaches this critical value that propagation will initiate. Specifically, the theory hypothesizes that crack extension occurs 1) where dU/dV (given below) has a minimum value 2) when $S(\theta_0)$ reaches a critical value S_{cr}. The expressions for the stress field are given below:

$$S = \frac{1}{2} h(\varepsilon_{xx}\sigma_{xx} + \varepsilon_{yy}\sigma_{yy} + 2\varepsilon_{xy}\sigma_{xy})$$
$$\frac{dU}{dV} = \frac{1}{r}(\frac{S}{\pi}) \qquad (6)$$

where S = varying intensity of the strain energy density around the crack tip
dU/dV = strain energy density variation near the crack tip
ε_{ij} = strain tensor
σ_{ij} = stress tensor
h = thickness

In my analysis, I use the strain energy density computed by COMSOL Multiphysics based on the elastic stress field solution.

Although Lonsdale (1988) and Lonsdale et al. (1992) described the IR as a small westward propagating rift opening at 15mm/yr with a V-shaped eastern end, further surveying showed that the eastern half of the IR narrows Eastward, suggesting both Eastward and Westward propagation of the rift (Klein et al., 2005). Westward propagation of the IR may be related to the need to maintain a connection with the fast-spreading EPR while Eastward propagation represents the initial development of the rift as a crack from the EPR.

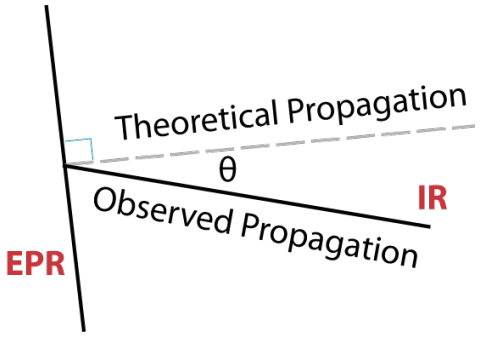

Figure 23. The observed relative angles between the East Pacific Rise (EPR) and Incipient Rift (IR) at the 2° 40' N RRR triple junction at the Northern Galapagos triple junction. In the absence of the CNR, Linear Elastic Fracture Mechanics theory suggests that the IR should propagate along the theoretical propagation path. The observed propagation of the IR follows a NW-SE trend.

It is clear from maps of the IR and other secondary rifts to the North of the CNR that they are not strictly perpendicular to plate motion. The IR strikes roughly S98°E whereas the CNR strikes at N277°W. Figure 23 shows the approximate geometric configuration of the relative positions between the EPR and IR. Extinct secondary rifts also strike ESE. Eastward propagation of an isolated crack should be perpendicular to the spreading direction, i.e., along a S96°E azimuth.

I propose that the stress perturbation due to the presence CNR favors crack propagation at an angle from the spreading-normal direction. This would explain the consistent rift strike between 95° to 115°. I analyze the stresses around the crack tip in the model to determine the most likely direction of propagation of the IR using theoretical crack propagation criteria (Erdogan and Sih, 1963).

In order to better understand why these secondary rifts are propagating to the observed SE direction, I sampled the stresses along a circle near the IR tip and determined the theoretical preferred direction of propagation with the criteria given in Equation 5. These three crack propagation criteria are 1) $\sigma\theta_{max}$ (or hoop stress theory in literature): a criterion that indicates that a crack will naturally propagate to a point with the highest value of $\sigma_{\theta\theta}$ 2) $\tau_{r\theta} = 0$ for Pure Mode I cracking where the tension is greatest and 3) $S\theta_{min}$ direction where the minimum strain energy on any plane at that specific angle is located. The diameter of the sampling circle is 0.07 around the rift tip. These models calculated these cracking criteria with varying circle radius to evaluate the effect of length scale on rift propagation azimuth.

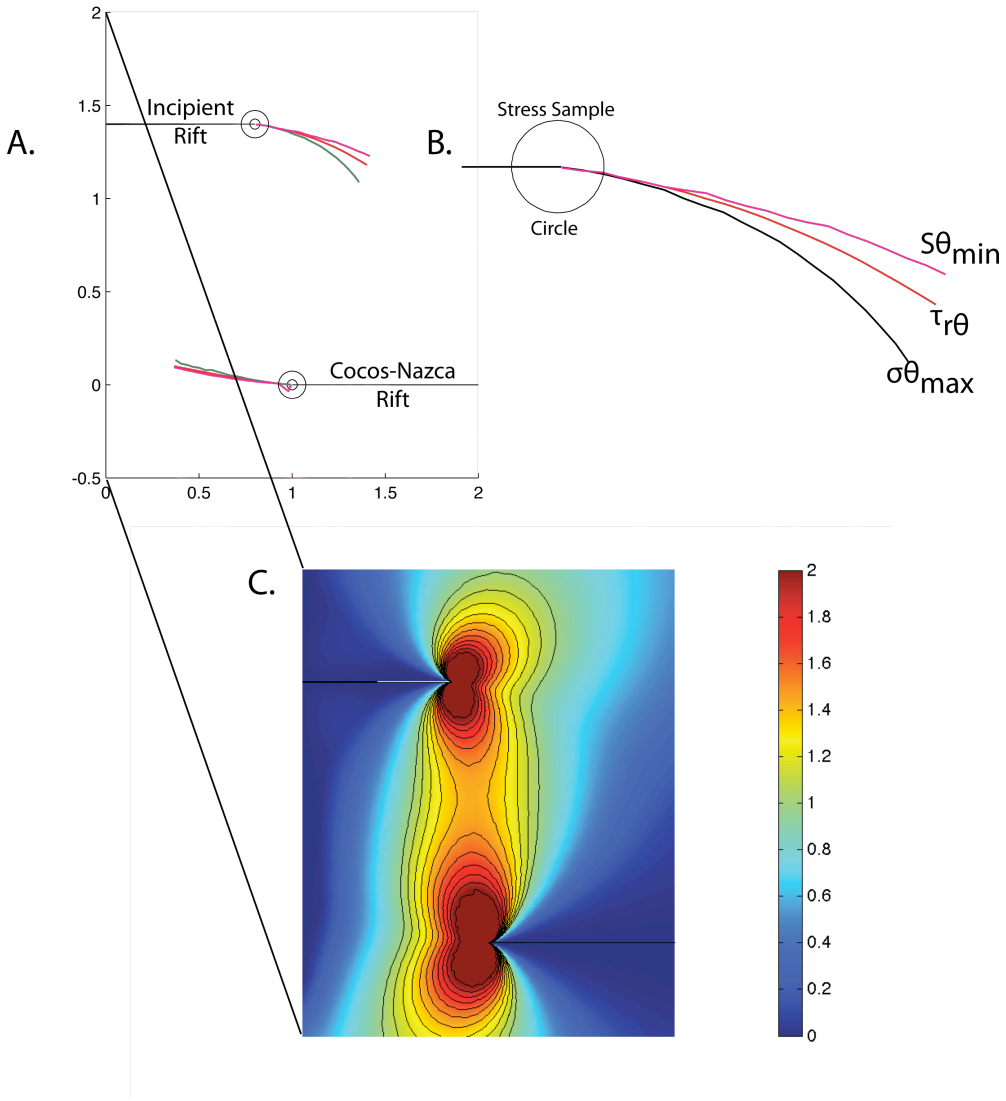

Figure 24. A. Model boundaries showing the geometric relationships between the IR-like ellipse at a length of 0.8 with the CNR-like ellipse. B. Closer view of the IR tip with the stress sample circle where measurements were taken of the stress fields surrounding the crack tip. Dark green/black line is the theoretical propagation line for the $\sigma_{\theta\theta}$ crack criteria, red for $\tau_{r\theta}$ criteria, magenta for the $S\theta_{min}$ criteria. Contours are mapped at 0.2 stress enhancement.

For this study, the IR Attached model is used where the IR is located at + 1.4 along the EPR, close to the actual location of the IR with respect to the CNR rift tip. The direction of propagation determined from fracture mechanics is then compared to the measured azimuths of the secondary rifts. Figure 24 shows the IR-CNR positions with the model along the stress sample circle. The colored lines – dark green, red, and

magenta – indicate the calculated direction of propagation for an IR that has a length of 0.8. The figure shows that the $\sigma\theta_{max}$, $\tau_{r\theta}$ and $S\theta_{min}$ predict similar rift propagation directions and agree with the azimuth observations.

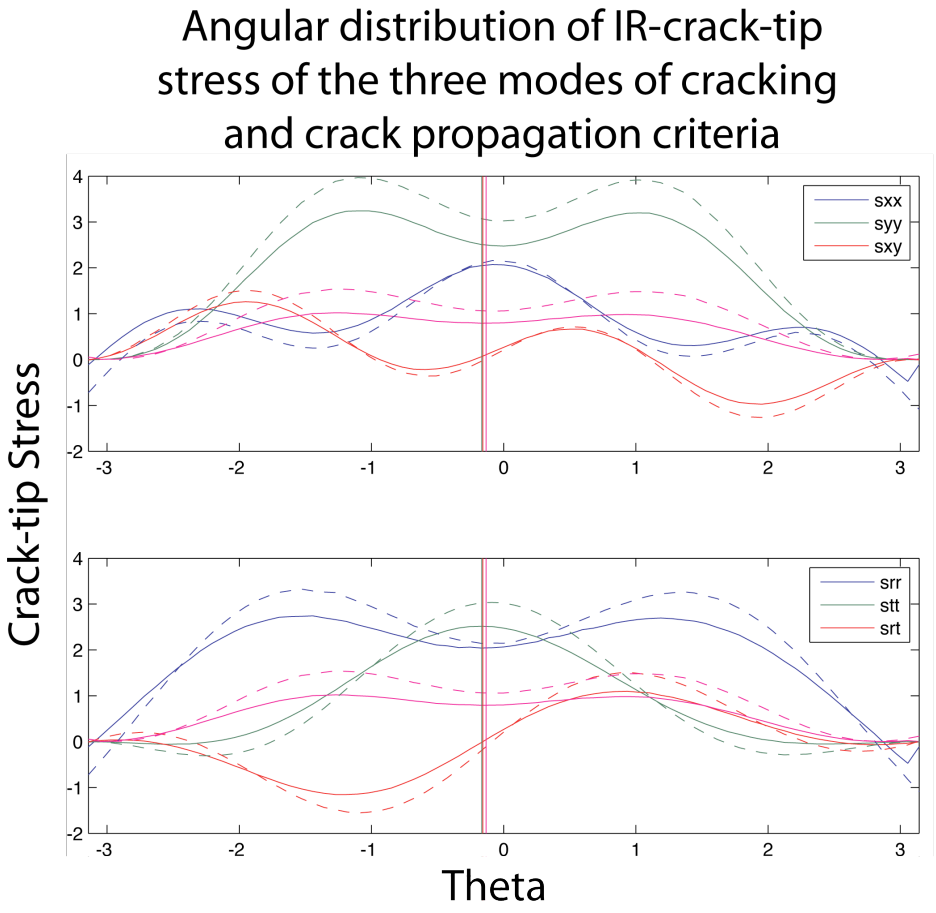

Figure 25. Stress profiles of σ_{xx}, σ_{yy}, and τ_{xy}, (top graph) and $\sigma_{\theta\theta}$, σ_{rr}, and $\tau_{r\theta}$ (bottom graph) along a small circle around the tip of IR (solid lines) and the CNR (dashed lines). Vertical lines represent the propagation direction according to each of the three criteria. Dark green line refers to the $\sigma_{\theta\theta}$ criterion, red line refers to the $\tau_{r\theta}$ criterion, and magenta line refers to the $S\theta_{min}$ The profiles are for an IR length of 0.8 and indicates that the IR would propagate at an azimuth of 99.7° for the $\sigma_{\theta\theta}$ criterion, and 99.1° for the $\tau_{r\theta}$, and 97.6° for the $S\theta_{min}$ criterion.

Figure 25 shows the profiles for the radial stresses surrounding the IR crack tip. Vertical lines signify the theta angle where the crack should propagate using the three criteria. All three of the crack criteria, $\sigma\theta_{max}$, $\tau_{r\theta}$, and the $S\theta_{min}$ criteria are in good agreement with each other and indicate that under the influence of the CNR tip, the IR should propagate to the ESE as noted by the negative theta angle. Figure 26

shows a graphical representation of this angular propagation as a function of IR length. For a distance of 0.8 from the IR tip, propagation would be along an azimuth of ~ 98-100°. This measurement is in good agreement with the GIS analysis of the secondary rifts discussed in Section 3.2.

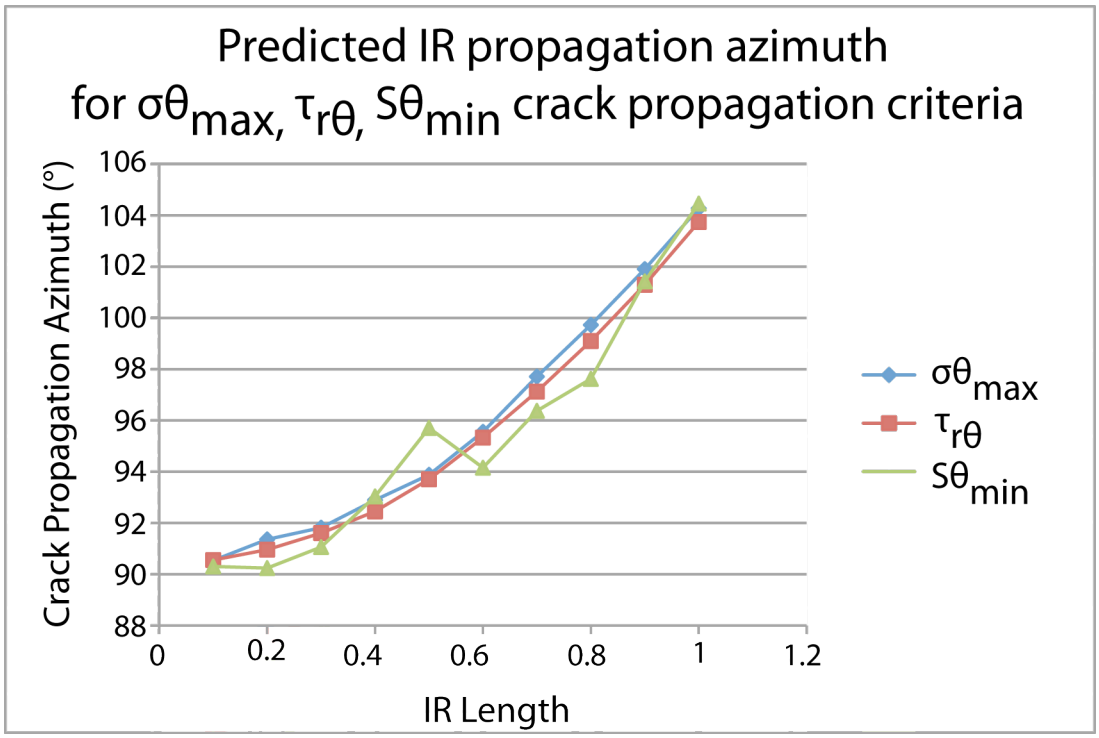

Figure 26. Crack propagation azimuth as a function of IR length. When the IR is small, there is less of an influence from the regional stress field controlled by the location of the CNR. Without the presence of the CNR the IR is expected to propagate at 90°, normal to the direction of the EPR strike. When the IR grows, the CNR influence increase that creates a greater SE propagation.

Chapter 6: Modeling of the Rodriguez Triple Junction

Although considered kinematically stable, Ridge-Ridge-Ridge (RRR) triple junctions often display a complex sequence of short-lived rifts and no direct connection between the ridges (Schouten et al., 2008). I use the GTJ and RTJ RRR triple junctions as stability end-members. My study of the GTJ shows that the mechanics of crack interaction can explain the apparent instability of many RRR triple junctions. In contrast, the RTJ in the Indian Ocean is characterized by a simple geometric configuration (Figure 27). The Central, Southeast, and Southwest Indian Ridges appear to be directly connected, and lack evidence for secondary rifts such as those found at the GTJ (Sauter, 1997). I propose that the mechanics of crack interaction can explain why the RTJ has been stable over millions of years when the GTJ has not. I propose that the mechanical stability of RRR triple junctions is a function of the angle between the various ridges involved in the triple junction. Following the modeling methods described earlier, I developed several numerical models of the stress field in an elastic plate under tension, with cracks representing rifts in the vicinity of a RRR triple junction to explore RRR triple junction stability.

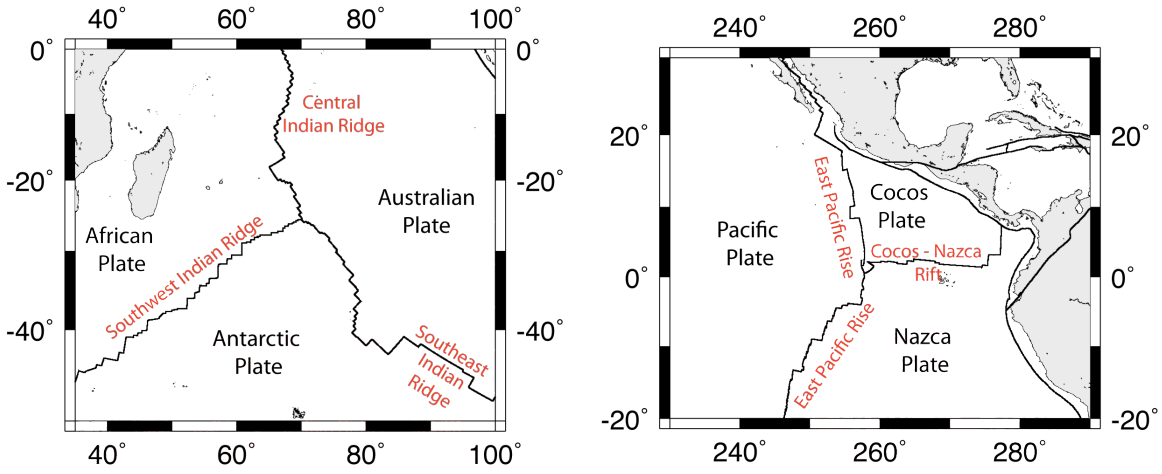

Figure 27. Regional maps of the RTJ and GTJ. These RRR triple junctions are end members in terms of stability where the RTJ features a direct connection between the major ridges involved and at the GTJ, there is a lack of connection between the major ridges. Ridge azimuth and triple junction geometry are proposed to contribute to a RRR triple junction's mechanical stability.

6.1 Modeling Methods

This section of my work reveals how the angles between the major ridges of a triple junction control the stress field interaction. Specifically, I examine whether direction connection between the slowest branch of the RRR triple junction (the CNR at the GTJ or the SWIR at the RTJ) and the faster ridges would be either mechanically prohibited or promoted for different angles between the faster ridges. For these models, I first assume a simplified geometry for the GTJ and RTJ-like models that is symmetrical with respect to the slowest ridge in order to focus on the effect the geometry of the two faster ridges. For simplicity, I adopt a 105° angle separating the SWIR for the CIR and the SEIR (β=15° in Figure 28). The simplifying assumption of a symmetrical configuration is removed in section 6.2.2. The current geometry of the GTJ suggests that the CNR is indeed oriented perpendicular to the EPR, but at the RTJ, the SWIR intersects kinked CIR and SEIR ridge segments (Figure 29).

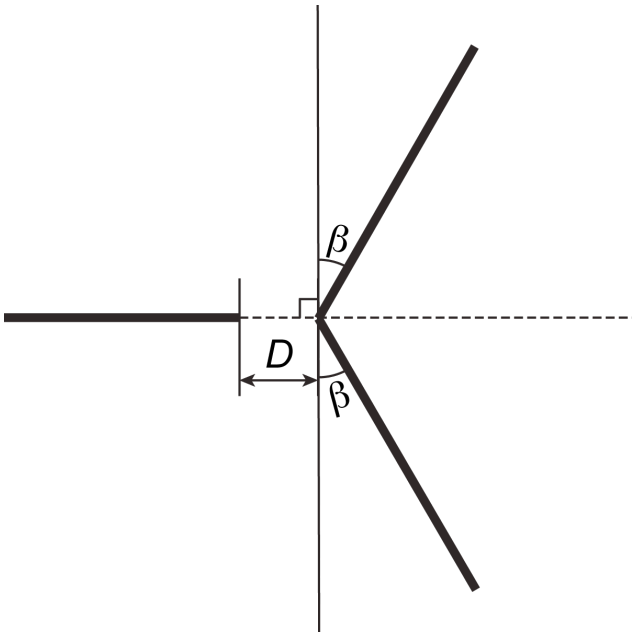

Figure 28: General geometry of a symmetric RRR triple junction, with 2β the kink angle between the two faster ridges. I test triple junction stability by disconnecting the third ridge by a distance *D* and solving for the stress field due to in-plate tension. If maximum tension along the still continuous ridge is at the kink, ahead of the detached rift, the detached rift may reconnect. Otherwise, a sequence of secondary rift may form.

Following the model construction method described earlier in Section 4.2.2, I set up symmetrical models with different 2β angles between the two faster ridges (Figure 28). The GTJ and RTJ are represented by the 2β≈0° and 2β=30° models, respectfully, where 2β=15° presents an intermediate configuration. Figure 29 shows the end member models superimposed on the bathymetry of their respective triple junction. The relative velocity of the plates is computed to be compatible with the orientation of the ridges (Figure 27) and is imposed on the model boundaries not identified as rifts. All the rifts in these models are stress free.

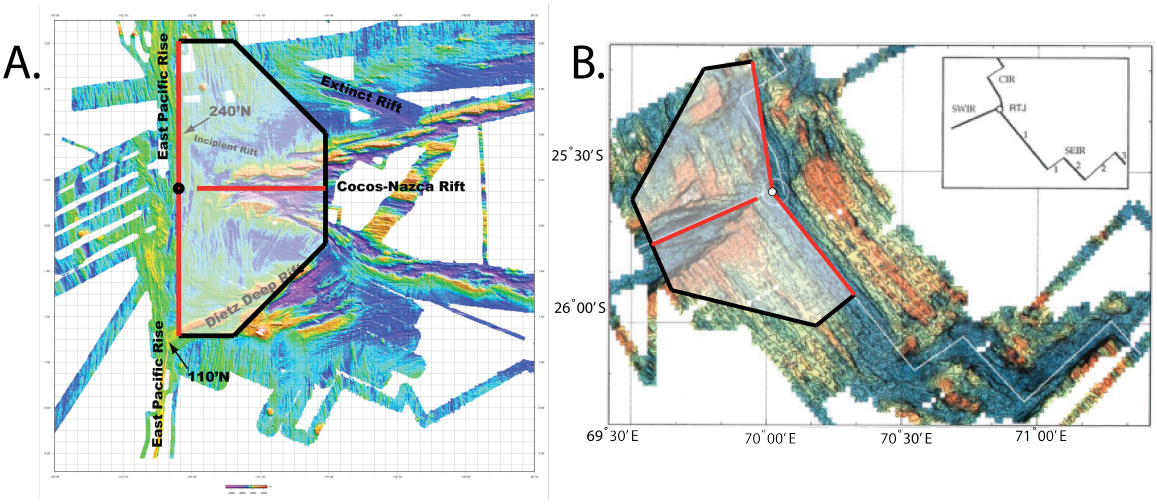

Figure 29: The geometry of the symmetrical models used in the study overlain on the bathymetry of the GTJ and RTJ. A: 0° for the GTJ B: 15° for the RTJ. Bathymetric data from D.K. Smith (personal communication, 2009) for the GTJ and from Honsho et al., (1996) for the RTJ.

6.1.1 Ridge Geometry and Velocity

For a given RRR triple junction, there is a direct relationship between azimuths, spreading directions and velocities of the ridges, as given by the velocity triangle for this triple junction. A velocity triangle represents the relative velocities of the three plates involved at a given triple junction. Assuming that spreading is symmetric, ridges are represented as lines bisecting each of the segments of the triangle. Any point moving along a ridge will have a velocity along that line. The triple junction velocity is the point at which the three ridges velocity lines intersect (Figure 30). The long-term kinematic stability of a triple junction is due to the existence of a single point representing the triple junction.

RRR triple junctions typically feature two faster ridges, represented in Figure 30 as the U1 and U2 vectors, a slower third ridge, with opening velocity U3. The geometry of a specific RRR triple junction depends upon the ratio of ridge spreading

velocities, U1/U3 and U2/U3. In the simplified symmetric model shown in Figure 30, U1 = U2 > U3, leading to a geometrically symmetric and kinematically stable triple junction.

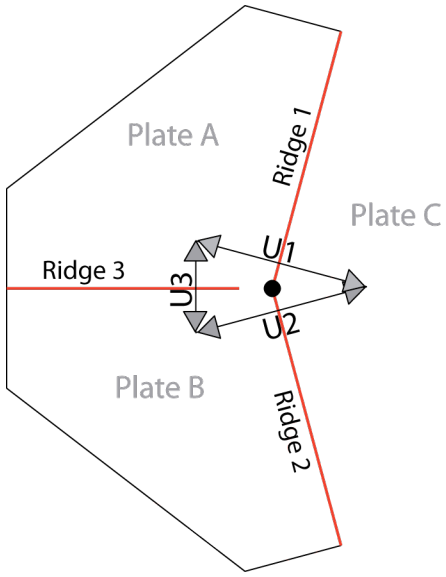

Figure 30. Schematic of the simplified symmetric RRR triple junction explaining how the ridges' velocities dictate the overall geometry and stability of a RRR triple junction. Velocity vectors whose length is representative of the ridge's full-spreading rate cross the ridges at right angles.

6.2 Modeling Results

6.2.1 Symmetric Models

Figure 31 presents the stress enhancement maps and Figure 32 presents the associated profiles taken along the faster ridges for three triple junction geometries with increasing kink angle β. For $2\beta \approx 0°$ configuration, as in the GTJ-specific models of Chapter 4, a zone of reduced tension forms between the detached crack tip and the continuous ridge, prohibiting direct rift connection. The two peaks of tensile stress enhancement develop at approximately $\pm$ 1.35*D* and control the development of a sequence of short-lived secondary rifts (Chapter 4).

The pair of stress enhancement maxima is observed again for the $2\beta = 15°$, the intermediate configuration, but their separation decreases: they are closer to the kink between the faster ridges from which the slower ridge detached from the triple junction (Figure 33). Although the position of these maxima changes, their amplitude is similar to the 0° case (Figure 34). However, a third local maximum of stress enhancement develops at the kink proper. For this intermediate model, the central peak of stress enhancement is of lower amplitude than the side peaks (Fig. 31). When $2\beta = 15°$, the stress amplitudes for the side peaks are similar to the amplitude observed at 0°. Therefore, rifts detaching at a RRR triple junction with this particular geometry may be able to reattach to the original triple junction point or a new crack could form at one of the side peaks. When the kink in the continuous ridges is increased to $2\beta \geq 15°$ the central stress enhancement maximum begins to dominate the stress field. The symmetrical double peak that dominated the $\beta \approx 0°$ model is barely visible on the shoulder of the central peak. I suggest that the presence of this zone of enhanced tension ahead of the slower ridge would facilitate a direct connection between the ridges at this triple junction and will be further elucidated upon in Section 7.3. The 2β angle was varied in these symmetrical models and the resulting profiles can be seen in Figure 32 and maps in Appendix C.

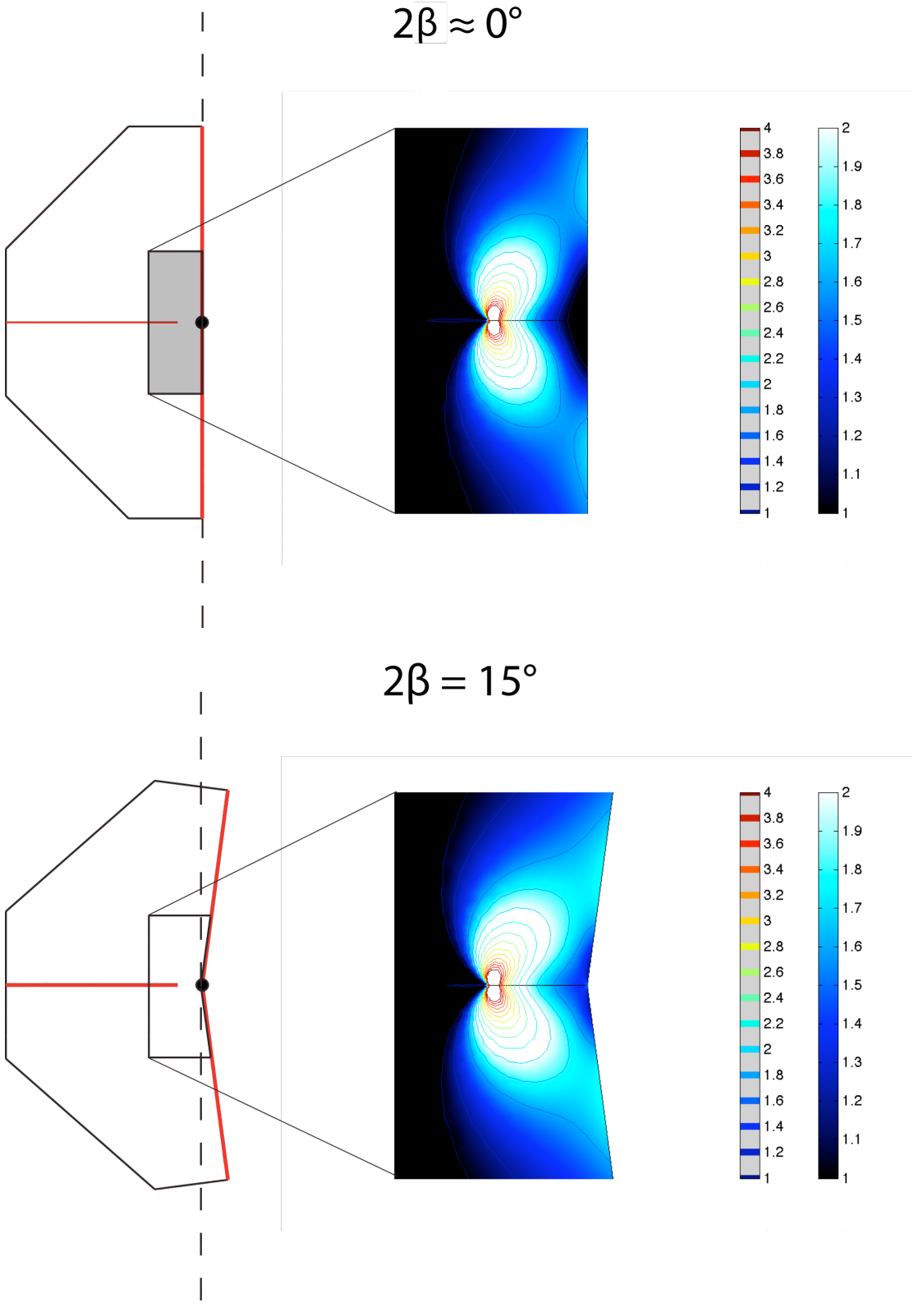
2β ≈ 0°
4
3.8
3.6
3.4
3.2
3
2.8
2.6
2.4
2.2
2
1.8
1.6
1.4
1.2
1
2
1.9
1.8
1.7
1.6
1.5
1.4
1.3
1.2
1.1
1
2β = 15°
4
3.8
3.6
3.4
3.2
3
2.8
2.6
2.4
2.2
2
1.8
1.6
1.4
1.2
1
2
1.9
1.8
1.7
1.6
1.5
1.4
1.3
1.2
1.1
1

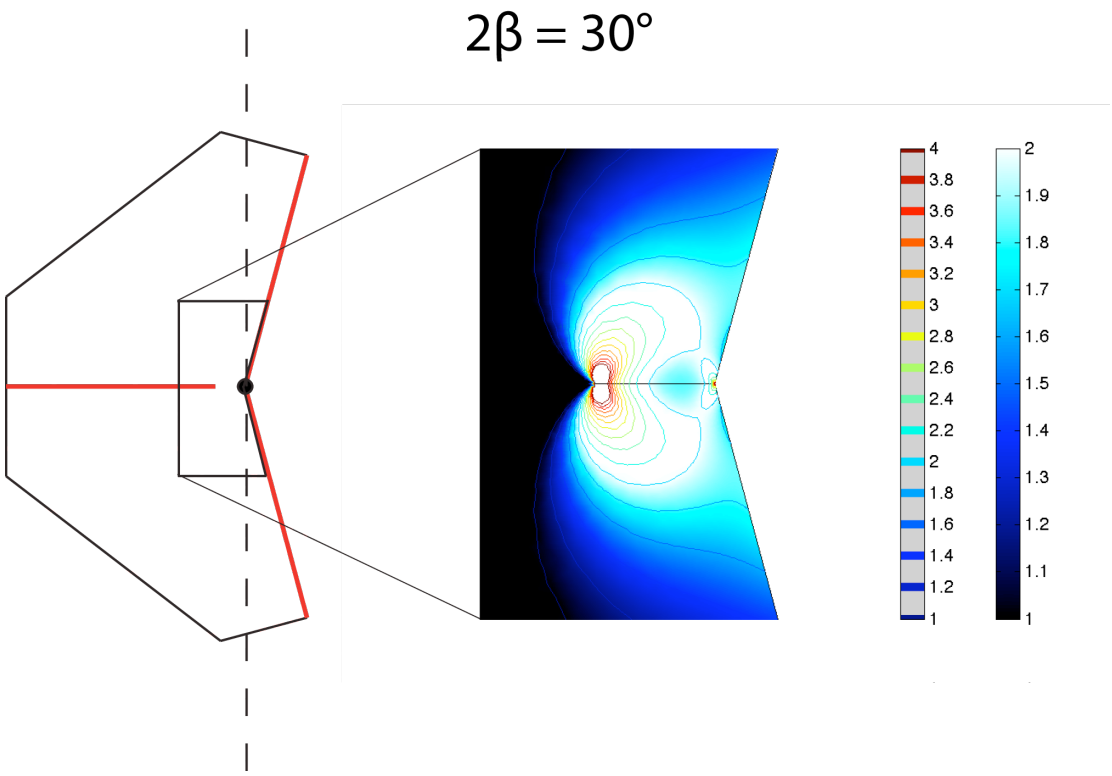

Figure 31. Results of the symmetrical RRR modeling for the GTJ (2β ≈ 0°) an intermediate case (2β = 15°) and RTJ (2β = 30°) where 180°-β is the angle between the two segments of the continuous ridge marking the right boundary of the models. Left: Geometry of the entire model. Rifts (red lines) are kept stress-free. Right: Map of stress enhancements of a restricted portion of the models where contours are at 0.2 increments. When 2β ≈ 0°, reconnection is prohibited and secondary rifts form offset along the major ridges. Increasing 2β decreases the amplitude and position of these side peaks and tension increases at the point of rift detachment facilitating a reconnection between ridges.

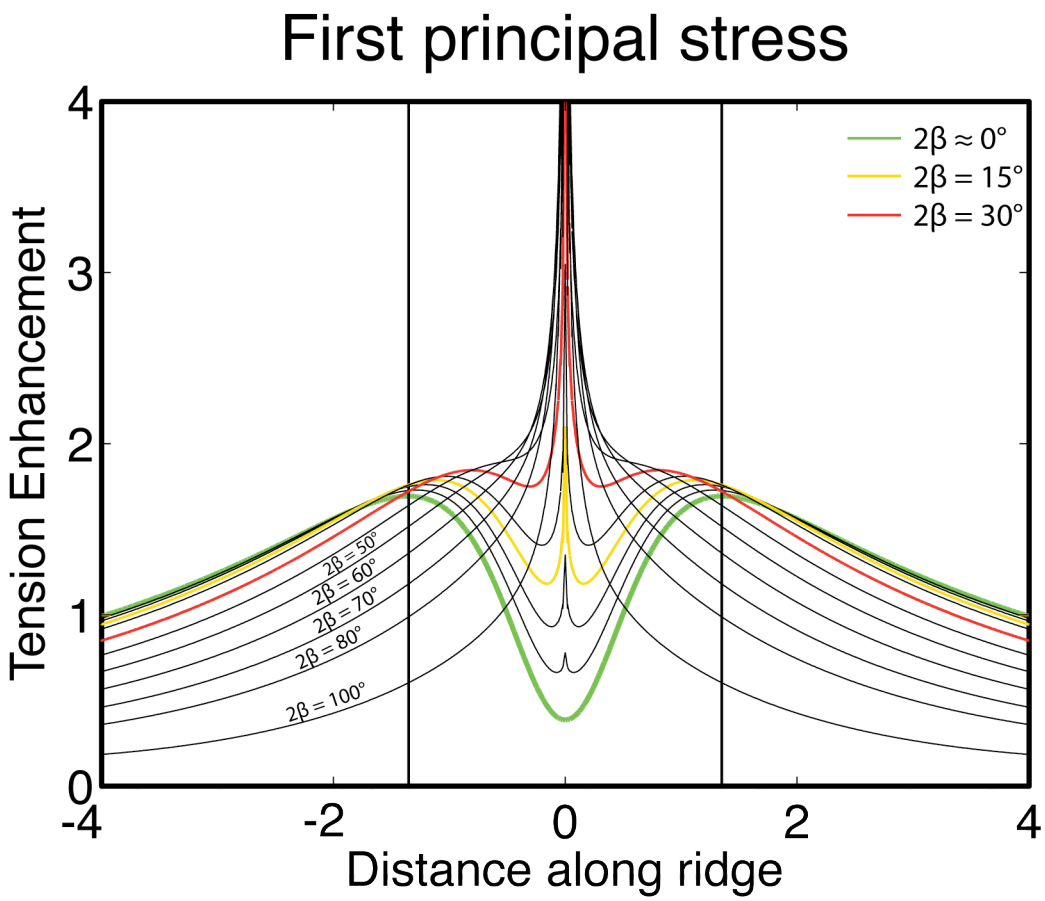

Figure 32. Profiles of stress enhancement along the right boundary of each model. 0 is at the junction between the two connected segments. The vertical black lines at 1.35 indicate the peak location of the 2β≈0° model, for reference. The models in Figure 31 are shown by the green, yellow, and red lines. Rift reconnection is prohibited with 2β values of < 7.5° and is promoted by 2β values over 10°. This suggests that the geometry of the triple junction, specifically the angles between the major ridges control its overall kinematic stability.

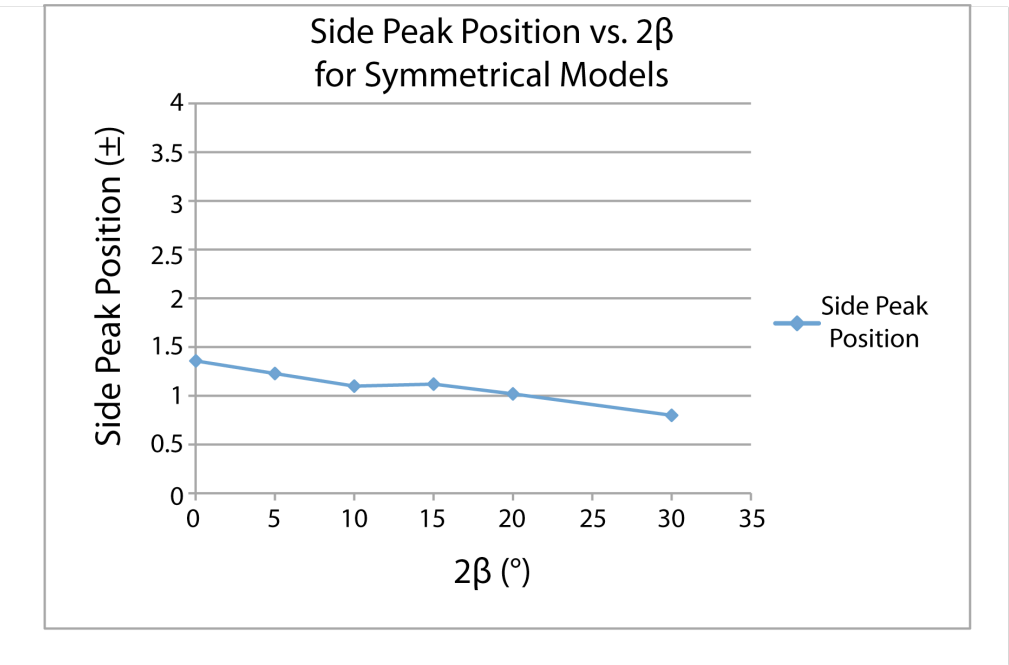

Figure 33. Location of the side peaks against kink angle 2β in symmetric models. Both peaks migrate slightly towards the point of rift detachment before merging into the larger central peak for β>30°.

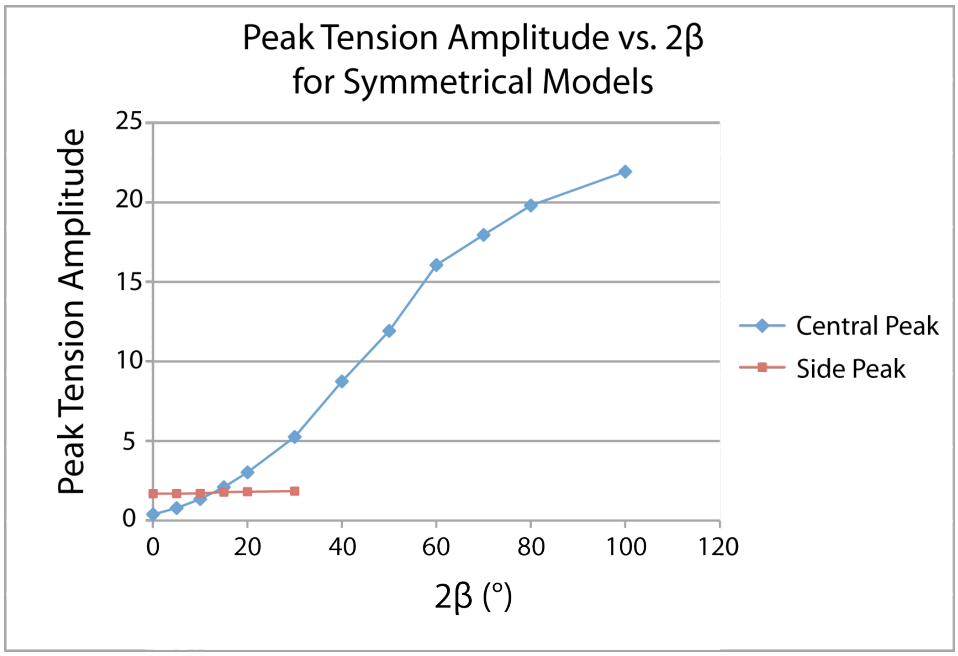

Figure 34. Amplitude of the central peak and side stress enhancement peaks against kink angle 2β. The amplitude for the side peaks does not vary significantly in the 0-30° range but they cannot be identified beyond 30°, when they coalesce into the stress enhancement at 0. The central peak amplitude increases continually with increasing kink angle.

6.2.2 Asymmetric Models

To precisely represent the geometry of the RTJ, it is not sufficient to include the different azimuth between the CIR and SEIR. The SEIR and CIR are composed of several ridge segments in the triple junction vicinity (Honsho et al., 1996). My own mapping of the RTJ as well as previous studies suggest that the RTJ is asymmetrical (West et al., 1995; Honsho et al., 1996) (Figure 34), motivating me to examine the effect of asymmetry in the ridge configuration on the stress field. The general configuration of Figure 28 can be generalized by defining an asymmetry angle α as shown in Figure 36. I explored a limited range of α for the 2β=15° and 2β=20° models to address the importance of RRR asymmetry on RRR stability. In these asymmetric models, α rotates the faster ridges, changing the angle between the major ridges to produce an asymmetric triple junction.

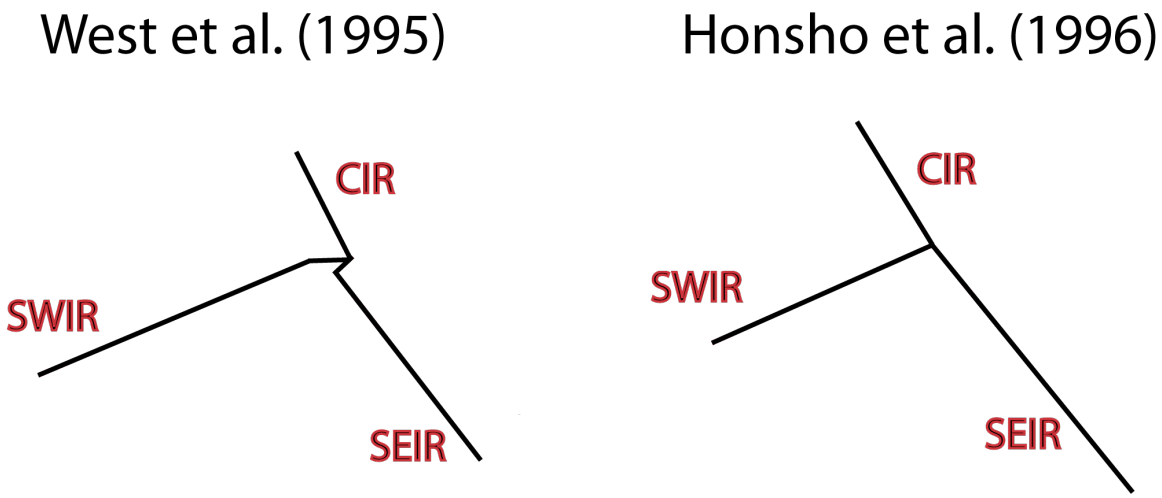

Figure 35. Schematic representation of the ridges at the Rodriguez Triple Junction from previous studies. Observations indicate that while the geometry of the RTJ is relatively simple, asymmetry exists between the SWIR, CIR, and SEIR and segmentation of the CIR and SWIR ridge crests leads to alternative, scale-dependent values estimates of the angle between the ridges.

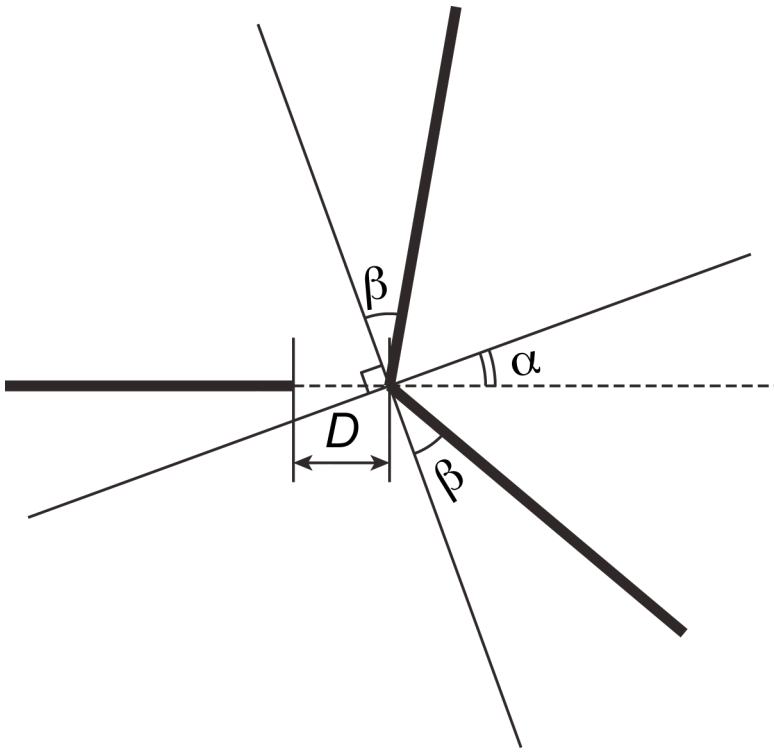

Figure 36. General asymmetric geometry of a RRR triple junction, where α is the asymmetry angle and 2β is the kink angle I test triple junction stability by disconnecting the third ridge by a distance *D* and solving for the stress field due to in-plate tension. If maximum tension along the still continuous ridge is at the kink, ahead of the detached rift, the detached rift may reconnect. Otherwise, a sequence of secondary rifts may form.

Figure 37 shows the model boundaries and corresponding stress enhancement maps for β=10° and α=0°, 5°, and 10°. In the last case, the northern ridge is perpendicular to the detach ridge. Profiles taken along the ridges can be seen in Figure 38. The three stress enhancement maxima are reported in Figure 39 and the position of the side peaks in Figure 40. The central peak is always located at the junction between the two faster ridges.

Figure 39 shows that the amplitudes of the side peaks vary little with an increase in asymmetry, although the stress profile itself becomes clearly asymmetric (Figure 38). Both peaks migrate north along the ridge as asymmetry increases (Figure 40). The central peak magnitude is hardly affected by asymmetry (Figure 39). Although asymmetry does have an effect on the stress field, the magnitude of stress

amplitude at 0 remains larger than that of the side peaks in this model series. Thus, rift reattachment at the point representing the previous triple junction is favored for $\beta=10°$ regardless of obliquity.

For a smaller kink angle of $\beta=7.5°$ the amplitude of the central peak is not much larger than that of the side peaks in the symmetric models of Section 6.2.1 (Figure 34). Figure 41 to 44 show the same information as Figure 37 to 40, but for $2\beta=15°$. Asymmetry moves the side peaks slightly to the north (Figure 44), and increases slightly the amplitude of the Northern peak (Figure 43). In the same time, the amplitude of the central peak decreases with increasing asymmetry (Figure 43) so that at the maximum asymmetry considered here, it is not clear whether reconnection between the ridges is indeed possible or if a series of secondary rifts will develop along the northern branch.

Thus, it appears that when the angle between the fastest ridges is close to the transition for which the central peak dominates, asymmetry in the ridge configuration can reduce the central peak to the point where a sequence of secondary rifts is possible. Asymmetry plays such a role only for a restricted range of kink angle β. Nevertheless, the kink angle predicted at the RTJ based on plate velocities is 7.5°, which is at this transition. Then, a change of triple junction asymmetry at the RTJ, as is associated with short-lived changes in segmentation evident in the triple junction geology (West et al., 1995) could lead to change in the triple junction stability. Mitchell (1991) reported an area of lineations that crosscut Central Indian Ridge-generated abyssal hills to the North of the SWIR. This is the region where secondary rifts would be expected based on the direction of asymmetry currently observed at the

RTJ. Thus, the RTJ appears to be at the limit of RRR triple junction stability, with an increase of asymmetry or a decrease of kink angle sufficient to trigger a series of secondary cracks out of the CIR, albeit not as well developed as at the Northern GTJ.

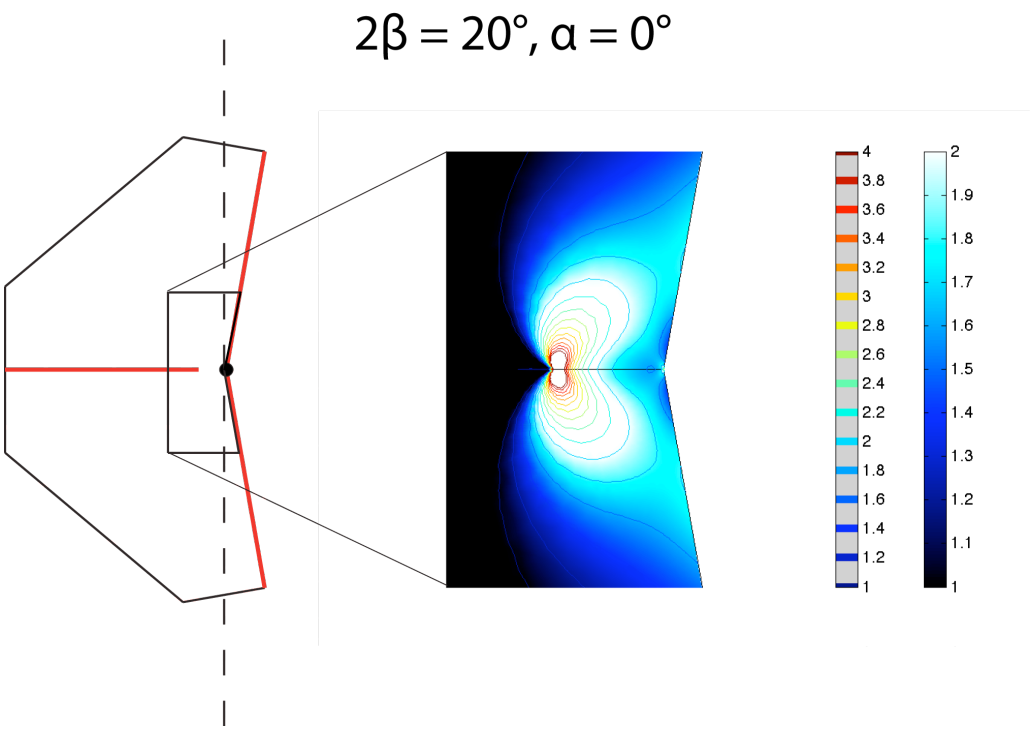

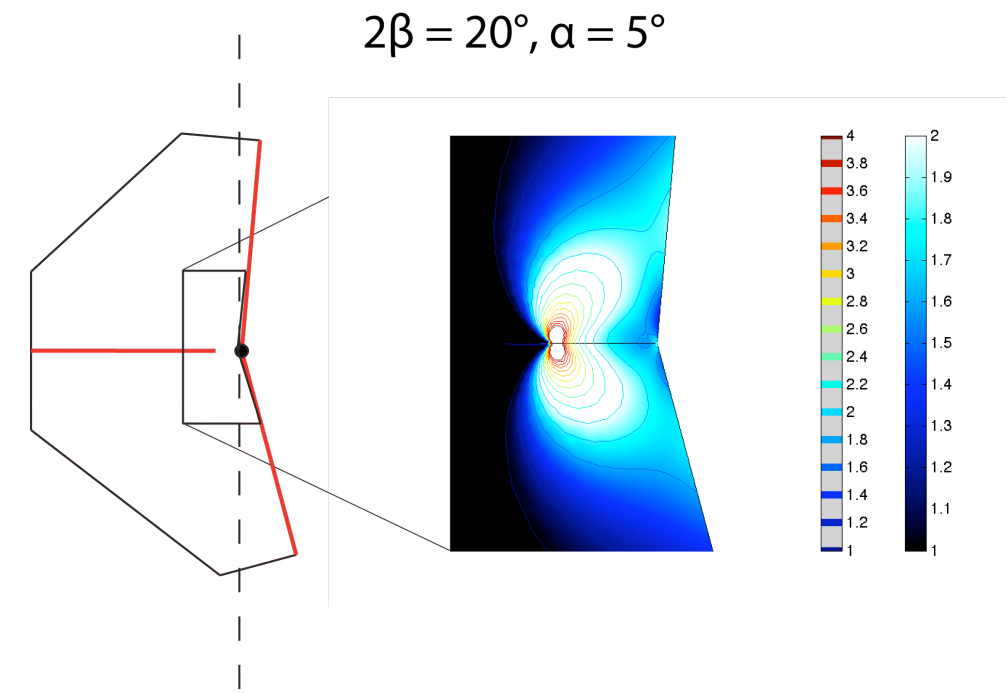

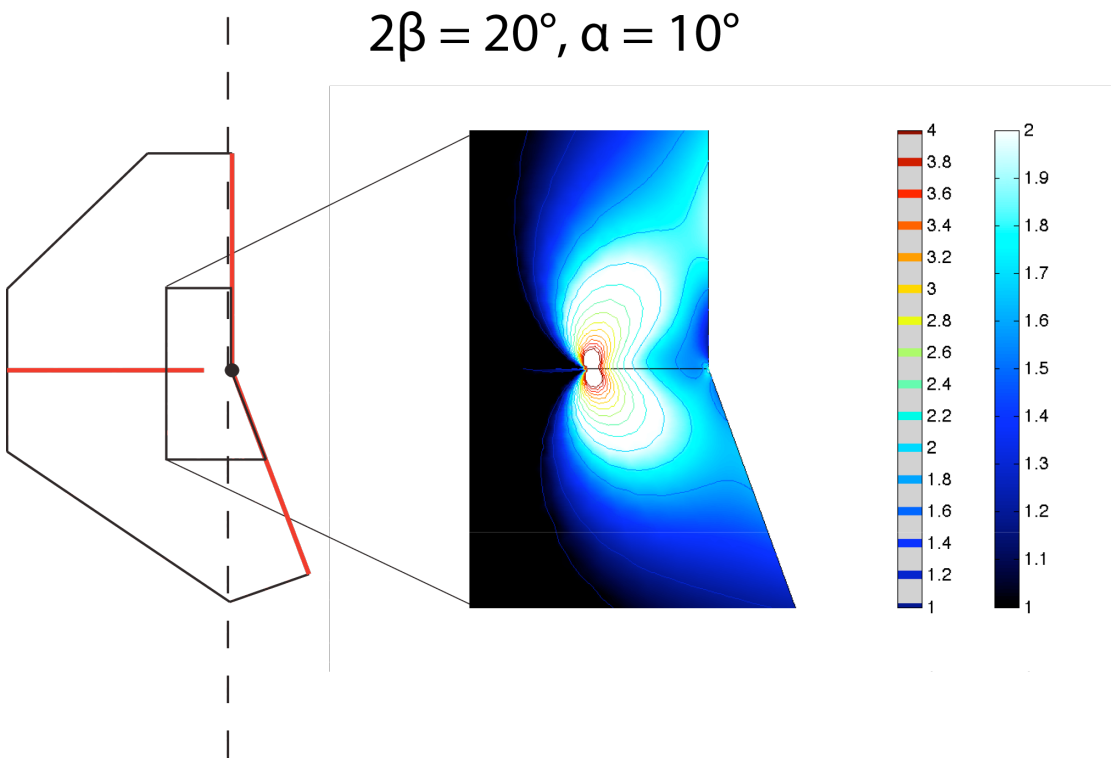

Figure 37. Stress enhancement maps and model geometries for the 2β = 20° models as in Figure 31 but for α=0°, 5°, and 10°.

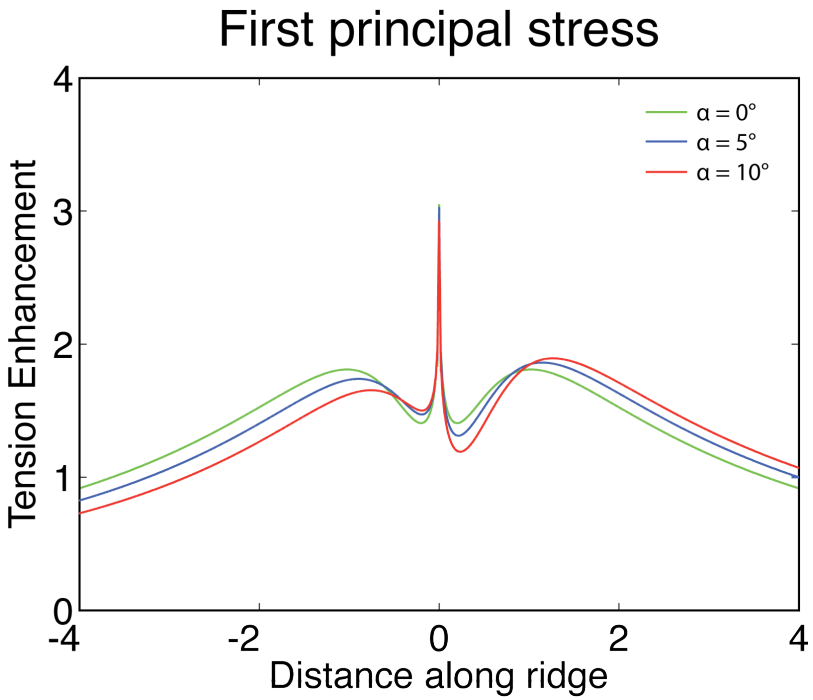

Figure 38. Stress profiles taken along the ridges for the models in Figure 37. In each case, the amplitude of the central peak is greater than that of the side peaks, implying that the RRR triple junction can remain connected.

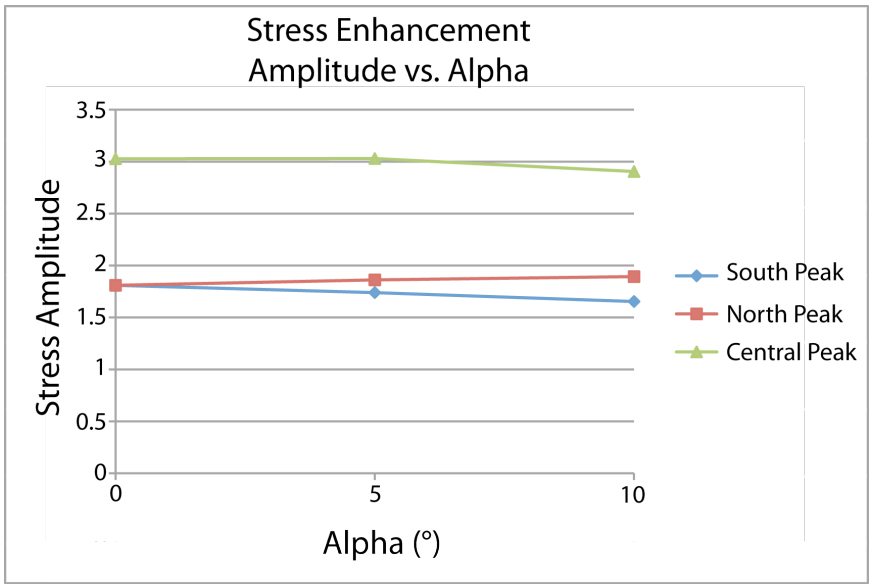

Figure 39. Amplitude of the south peak, north peak, and central peak of the stress enhancement profiles of Figure 38 against asymmetry angle. Little change in overall amplitude is noted. Because the central peak has a much greater amplitude than the side peaks, it always dominates the stress pattern. Asymmetry at this scale does prevent the disconnected rift from reattaching.

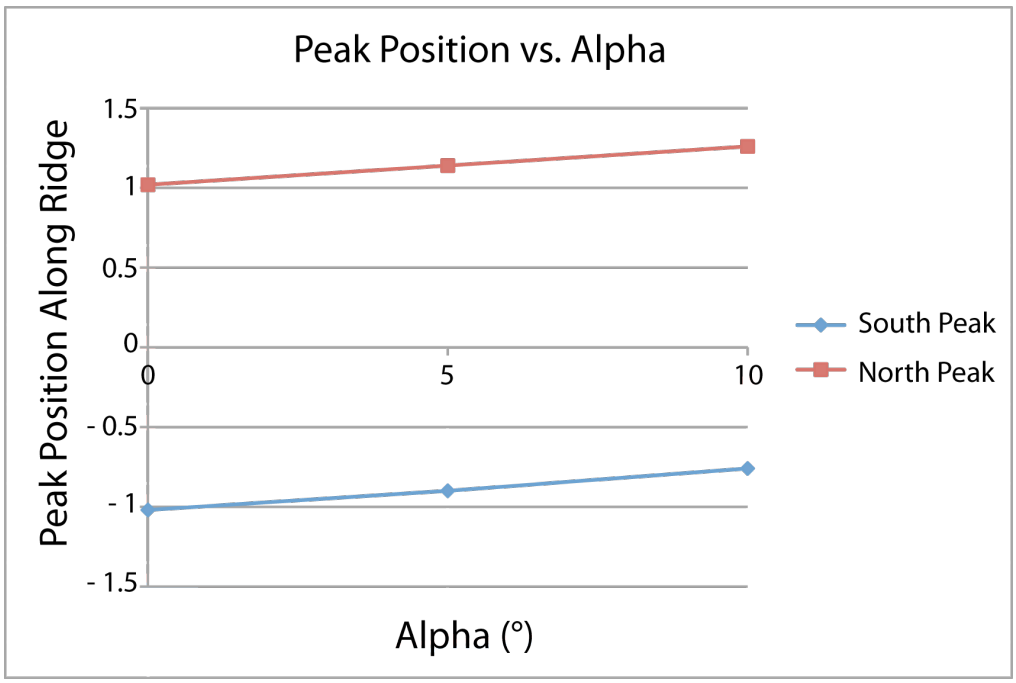

Figure 40. Side peak positions as a function of asymmetry angle. When the asymmetry between the angles is increased, both peaks migrate to the north slightly, reflecting the growing skew of the stress enhancement profiles in Figure 38.

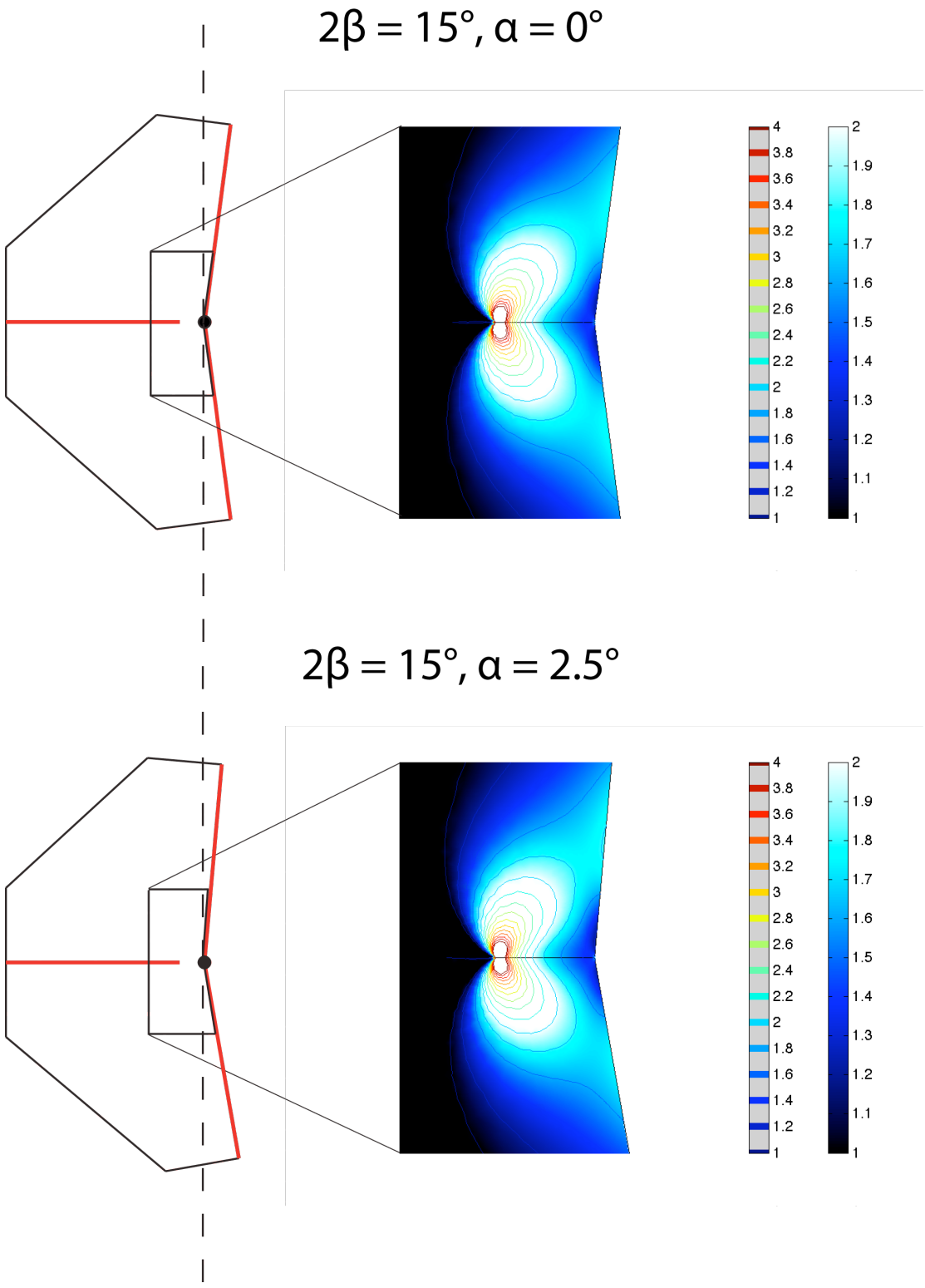
2β = 15°, α = 0°
4
3.8
3.6
3.4
3.2
3
2.8
2.6
2.4
2.2
2
1.8
1.6
1.4
1.2
1
2
1.9
1.8
1.7
1.6
1.5
1.4
1.3
1.2
1.1
1
2β = 15°, α = 2.5°
4
3.8
3.6
3.4
3.2
3
2.8
2.6
2.4
2.2
2
1.8
1.6
1.4
1.2
1
2
1.9
1.8
1.7
1.6
1.5
1.4
1.3
1.2
1.1
1

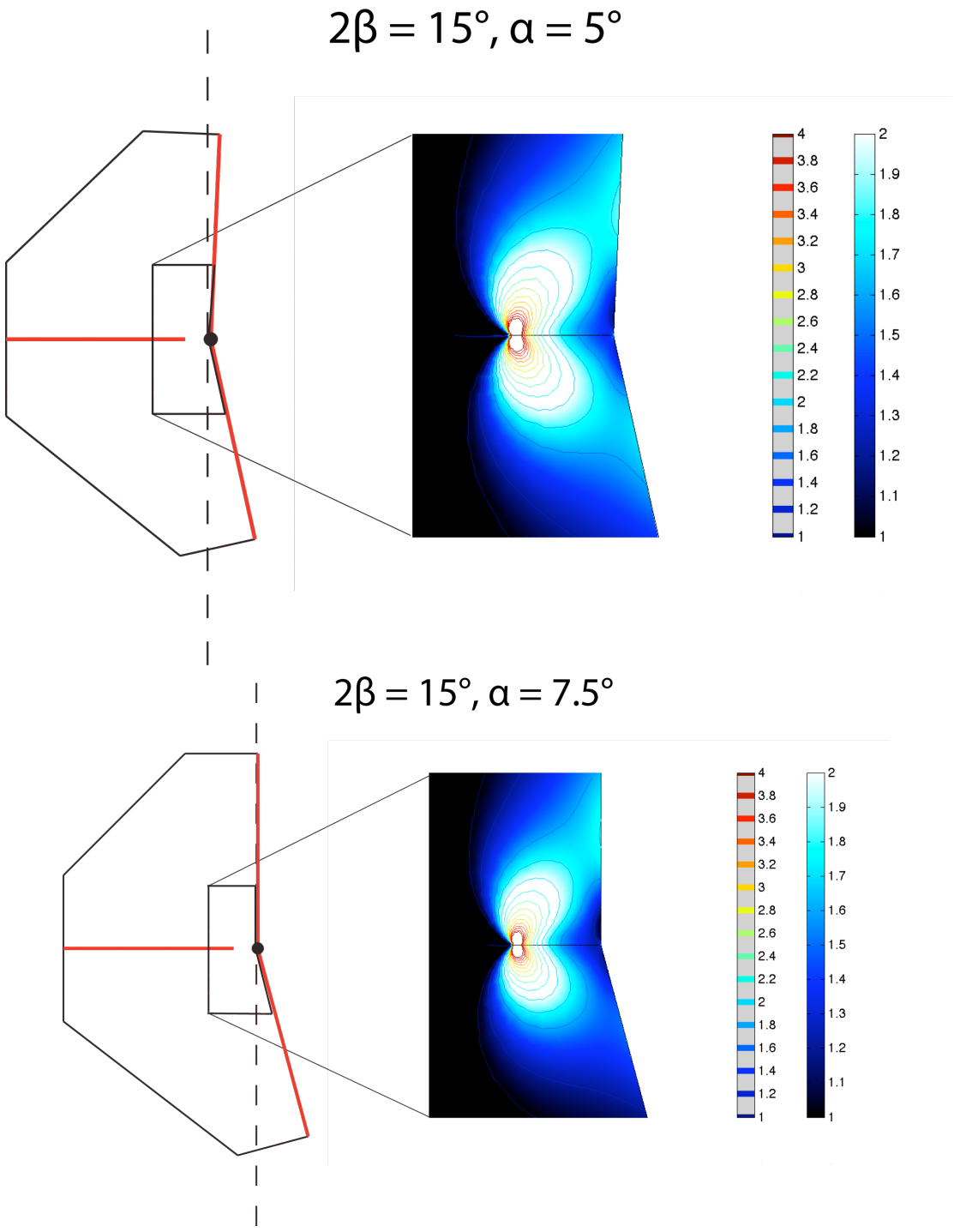

Figure 41. Stress enhancement maps and model geometries, as for Figure 37 but for 2β=15° and α=0°, 2.5°, 5°, and 7.5°.

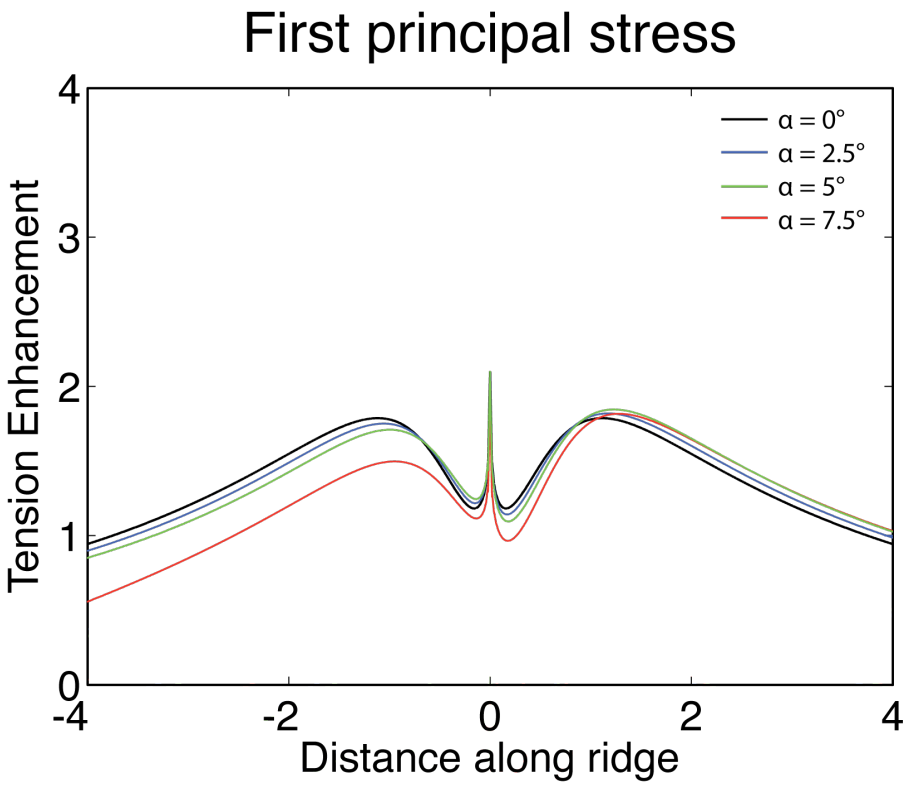

Figure 42. Stress profiles taken along the ridges for the models of Figure 41. In each of these cases, the central peak has a higher magnitude than the side peaks, although barely so for α=θ=7.5°.

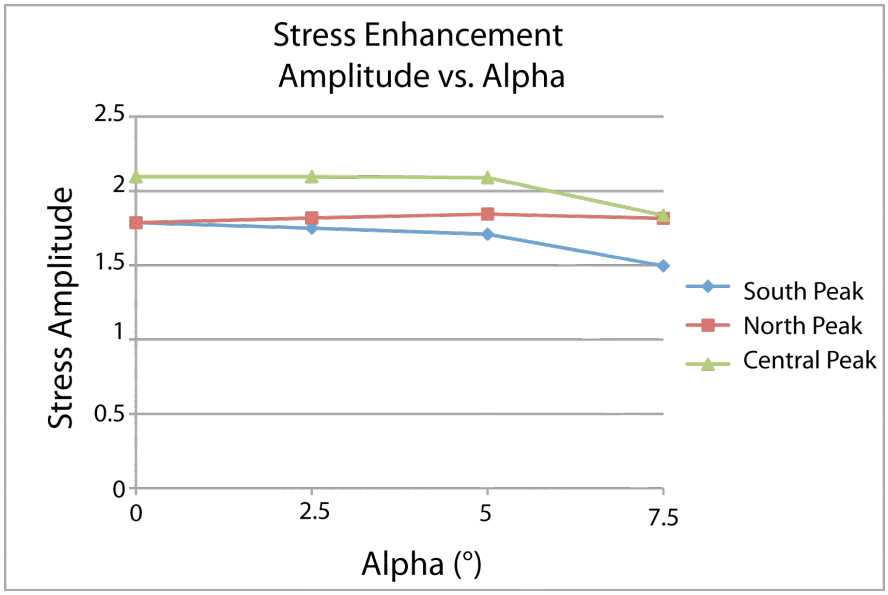

Figure 43. Same as Figure 39 but for the stress enhancement profiles of Figure 42. Asymmetry decreases slightly the amplitude of the central peak and increases slightly the amplitude of the North peak, which can cause a loss of connectivity between the ridges for extreme obliquity.

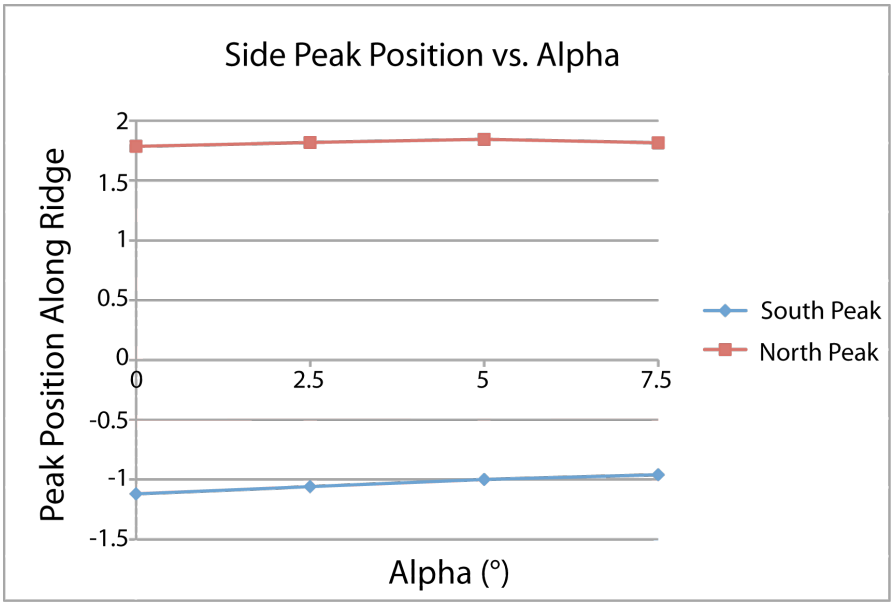

Figure 44. Same as Figure 40 but for the stress enhancement profiles of Figure 42. Like the previous asymmetry model ($2\beta = 20°$), the northern and southern peaks migrate North as asymmetry increases.

Chapter 7: Discussion

7.1 Mechanical Model of the Northern Galápagos Triple Junction

Data obtained from the geospatial database and modeling described in Chapter 4 provide insight into the kinematic history of CNR-EPR interaction, needed to better understand the evolution of the northern GTJ. This in turn helps with piecing together a kinematic evolution of a complex ridge-ridge-ridge triple junction.

The modeling results help understanding mechanically the evolution of rifting at the 2°40' N triple junction, in particular the succession of rift scars found to the northeast of the IR. These secondary rifts likely formed as cracks propagating away from the EPR at locations controlled by the position of the tip of the CNR.

My numerical models document the fundamental interaction that take places when a relatively small crack, perpendicular to the direction of extension, is close to a larger crack parallel to the direction of extension. For application to the GTJ, the larger crack represents the EPR, while the smaller crack stands for the CNR, the IR, or any of the older secondary rifts observed to the NE of the 2°40'N triple junction.

Numerical models, in which the geometry and locations of various rifts are varied in the general triple junction vicinity, constrain the factors that have led to the consistent location of secondary rift at the northern triple junction. The results indicate that once a rift has become detached from the East Pacific Rise, a zone of reduced tension forms at the rift tip prohibiting reconnection. Instead, two peaks of tensile stress enhancement form along the East Pacific Rise and are offset from the

detached rift indicating where a new crack is likely to form. I suggest that the magnitude of tensile stress enhancement is controlled by the gap between the detached rift and the East Pacific Rise, but the presence of the Cocos-Nazca Rift controls the location of new rifts along the ridge of the East Pacific Rise. Therefore, I infer that the sequence of ancient rifts at the 2°40' N triple junction represents the natural consequence of rift disconnection events and their position reflects the history of the gap between the EPR and the Cocos-Nazca Rift.

GIS analysis of the selected mapped rifts found northeast of 2°40' N all follow similar ESE-striking azimuths. The propagation at an angle from the EPR is due in part to the vicinity of the CNR tip. When the propagation direction models were analyzed, all three propagation criteria agreed well with what is observed through spatial analysis.

7.2 Evolution of the Northern Galápagos Triple Junction

The fundamental stress enhancement pattern that arises from the interaction between the CNR and the EPR includes a zone of reduced tension ahead of the rift tip. Stress is redistributed in a symmetric pattern on either side of the projection of the rift tip along the side of the larger rift, producing two stress maxima. The separation of these stress maxima scales with *D*, the gap between the two rifts. As expected from standard elasticity, similar patterns can be superposed for every rift in a given region. However, if rifts enter in contact, the result is a wide zone of stress reduction, which scales with the length of the smaller rift.

As the CNR approaches the EPR, the stress maxima described above will produce zones of cracking along the EPR, from which I assume a first secondary rift

is generated. The rift will propagate eastward, away from the EPR, in agreement with the morphology of the rift at its eastern end (Klein et al., 2005). Westward propagation of the IR (Lonsdale, 1988; Klein et al., 2005) may be related to the need to maintain a connection with the fast-spreading EPR. As long as the secondary rift remains connected to the EPR, stress is strongly reduced along the EPR, preventing the generation of additional rifts. At that stage, the gap between the EPR and the tip of the CNR can change without influencing secondary rift development.

To explain the generation of not only one, but a sequence of secondary rifts at the Northern GTJ, we must assume that at some point, the secondary rift becomes disconnected from the EPR. There could be several reasons for such disconnection. Spreading at the EPR requires the constant formation of new faults and magma conduits linking the EPR and the secondary rift. The connection could be lost during an episode of reduced magmatism or as new faults are generated. Alternatively, lateral propagation of dikes (Lonsdale, 1977; Fialko et al, 1998; Gregg et al., 2007), sills (Fialko, 2001), or abyssal hill – related faults (Edwards et al., 1991; MacDonald et al., 1996) may truncate the secondary rift. Once the connection with the EPR is lost, a zone of reduced tension forms along the EPR at the level of the detached secondary rift, which prevents reconnection with the EPR. The disconnected secondary rift becomes inactive and is rafted away from the EPR by the motion of the Cocos plates. However, a double peak of stress enhancement develops along the EPR, enabling new crack to form. The disconnected rift can be considered a parent rift and the new cracks may form a daughter rift along the EPR.

Because the gap between the parent rift and the EPR is likely small, the intensity of the local stress enhancement pattern is strong and dominates over the stress pattern generated by the CNR (Figure 13C). Thus, it may be thought that the sequence of secondary rifts detaching from the EPR and spawning new rifts at the EPR takes a life of its own. Why then, would the location of the current IR appear related to the gap between the EPR and the CNR (Schouten et al., 2008)? The answer lies in the asymmetry between the two stress enhancement peaks observed in Figure 14. The stress field is the superposition of a regional field controlled by the CNR and a local field controlled by the detached rift. At the scale of the local field, the regional stress field is smooth and acts as tilted baseline on which the local field stands (Figure 14). Thus, if the detached rift is north of a critical location that corresponds to peak in the regional stress field, the daughter rift is generated south of the parent rift, a left-stepping sequence of secondary rifts (Figure 16). Conversely, if the detached rift is south of that same critical location, the daughter rift is generated north of the parent rift, a right-stepping sequence of secondary rifts. Overall, the regional stress enhancement maximum acts as an attractor for the sequence of secondary rifts.

In detail, the transition from right-stepping to left-stepping rift sequence also features a region where the rift sequence may oscillate. Because there is a finite offset between parent and daughter rift, the product of a right-stepping event may be in the region where it will generate a left-stepping rift, and vice versa. In this case the detaching rifts produce alternatively left and right offsets with little or no long-term secondary rift migration. If the CNR tip is at a distance D from the EPR and the distance from the detached rift and EPR is $0.2D$, the oscillation window is located

between 0.91*D* and 1.35*D* (Figure 16). If the distance between the detached rift and the EPR is only 0.1*D*, the oscillation window is narrower and closer to the projection of the CNR along the EPR, from 0.94*D* to 1.20*D* (Figure 17). Thus, the distance between the detached rift tip and the EPR influences the width of the rift stability window and the magnitude of stress enhancement while the regional stress field, created by presence of the CNR tip, controls its overall location along the EPR.

Interestingly, very few right-stepping events are observed in the sequence of secondary rifts that marks the 2°40'N triple junction on the Cocos plate. One explanation could be that the CNR is continuously propagating toward the EPR, thus always moving the window of stability southward, and forcing only left-stepping events. However, there is a time interval, from 2.5 to 2 Ma, during which the distance between secondary rifts and the scarp marking the trace of the CNR tip has increased steadily (Schouten et al., 2008). The scaling relations described here would imply that the CNR retreated during that period. During that time, instead of a right-stepping rift sequence, I observe the presence of a single, pronounced rift, dubbed the Extinct Rift (ER, Klein et al., 2005; Schouten et al., 2008). The tip of the ER marks the furthest distance between the secondary rifts and the trace of the CNR tip. It is possible that it erased a right-stepping sequence, that led to the ER, or even that is reused these structure, explaining the exceptional longevity and relief of the ER. Left-stepping sequences are more easily preserved because the parent rift is rafted away from the daughter rift as part of the Cocos plate. The opposite relation would exist on the Nazca plate, where right-stepping sequences, corresponding to progressive advance of the CNR tip, would be more easily preserved than left-stepping sequences.

Approximately 25 secondary rifts have been mapped between the IR and ER (Klein et al., 2005) (Schouten et al., 2008). As the proposed age of the ER is 2 Ma, it can be inferred that detachment events occur roughly every 80,000 years. From 2 Ma to 1 Ma, the rift tips have migrated southward very rapidly, likely following an episode of rapid westward migration of the CNR tip. During that time, the triple junction was more unstable and the rift were abandoned more quickly than over the last 1 Ma. Rifts with poorly defined graben are inferred to be short-lived rifts that were quickly abandoned and detached from the EPR.

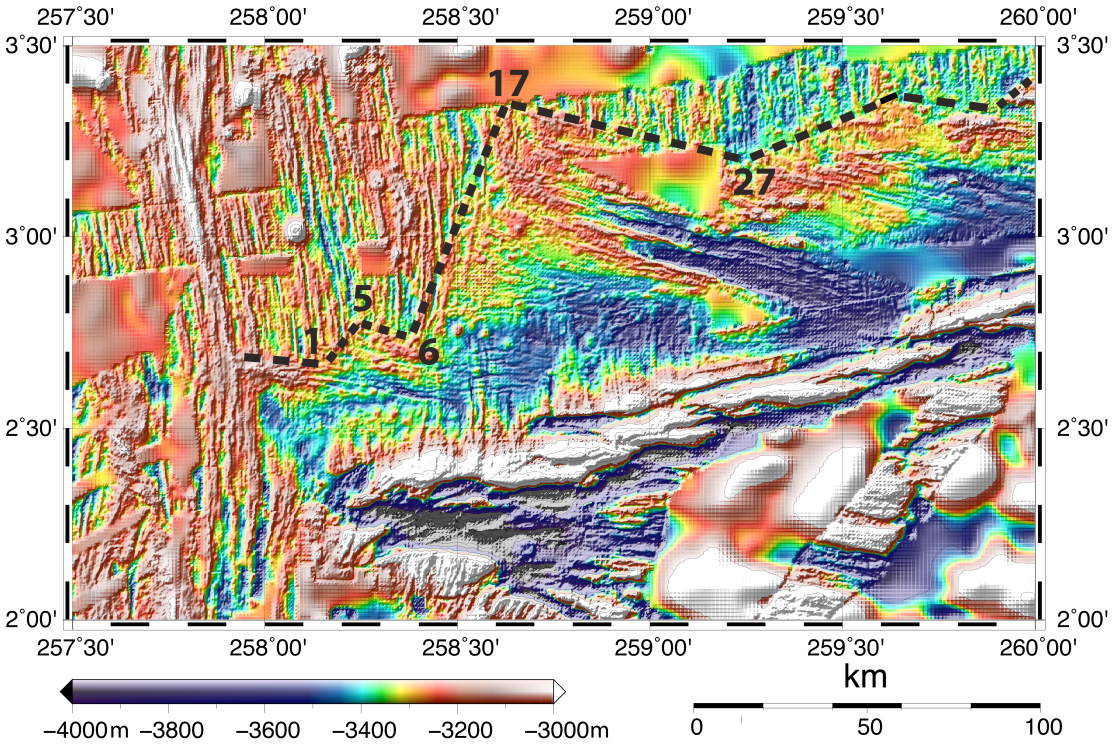

Figure 45. Bathymetry of the N GTJ with the limits of the secondary rifts outlined by dashed lines. Points refer to the GIS point analysis (refer to Figure 6). These secondary rifts record the relationship between the propagating CNR with the EPR. As the CNR approaches the EPR, complex stress interaction creates left-stepping rifts as seen between Points 1-5 and 6-17.

The GIS analysis of the rifts shows that the active IR is ~ 25 km long and propagating at ~ S98°E. Similar lengths and azimuths are noted for the next two

youngest detached secondary rifts. As noted in Section 5.4 the angular propagation is directly related to the length of the IR. The initial propagation angle of a new rift forming at 2° 40’ N would be at or close to 90°. As the rift grows, the influence of the CNR tip becomes greater thereby creating a higher angle of propagation to the SE. It can be imagined that the IR will not propagate much farther distance-wise than the offset distance from the EPR to the CNR tip. The longer extinct rifts found to the NE of the N. GTJ triple junction might reflect a time when the CNR tip was much farther away from the EPR. Figure 45 shows the outline of the secondary rifts with points reflecting the limits of select rifts. Between points 27 and 17 there appears to be a long jump to the northeast, unusual considering most of these rift jumps have been smaller and to the southeast, Perhaps rifts 17 to 27 represented a time when the CNR was receding from the EPR. Points 17 to 6 highlight a time when the EPR was encroaching on the EPR. The jump azimuth is consistent during this time and jump distances are similar, perhaps representing a period of consistency in the kinematics. Again, a relatively larger jump to the northwest is seen between points 5 and 6.

Also observed in these rifts are topographic highs that transition into valleys as the rift matures. The western sides of these rifts are actually volcanic ridges that taper into depressions. Perhaps these young cracks initiate as ridges and are being magmatically fed by the EPR. As the rift lengthens Eastward, the rift becomes magma starved and forms a depression. In the Extinct Rift, it appears there has been a series of overprinted rifts forming the region of low seafloor topography. Interestingly, immediately after the Extinct Rift is a long ridge of volcanically-high topography (Points 7 – 8 in the Figure 45).

Overall, it appears that because there is a lack of a direct connection between the EPR and CNR because of rift azimuths, the complex seafloor at the Northern GTJ can be associated with the kinematic history of the propagating CNR. The length, azimuth, offset distances and jump azimuths all reflect the relationships between the westward propagating CNR and EPR and record its kinematic history.

7.3 Stability of Ridge-Ridge-Ridge Triple Junctions

The series of models in Figures 31 and their stress profiles in Figure 32 indicate that the geometry between the ridges plays a significant role in the stability of a RRR triple junction. At the RTJ, the difference in azimuth between the CIR and SEIR is such that even if the slower-spreading SWIR detaches from the triple junction, a new crack will generate at the former triple junction and facilitate reconnection. By contrast, at the GTJ, where the EPR passes essentially straight through the triple junction, a zone of stress reduction develops between the detached CNR and the EPR, preventing reconnection. A sequence of secondary short-lived rifts develops instead. Thus, within a RRR triple junction, the position and orientation of the major spreading appears to control its mechanical stability.

The other three observed RRR triple junctions, the Bouvet Triple Junction in the South Atlantic, the Azores Triple Junction in the North Atlantic, and the Easter Island Triple Junction in the Eastern Pacific each display unique angular geometries, kinematic histories and tectonic features including zones of distributed deformation (Sclater et al., 1976; Searle, 1980; Bird and Naar, 1994; Luis et al., 1994; Ligi et al., 1997; Bird et al., 1998; Ligi et al., 1999; Mitchell and Livermore, 1998 (Figure 46). For example, geophysical studies of the Bouvet Triple Junction (BTJ) suggest that

this RRR triple junction actually existed as a junction between one ridge and two transforms (RFF) for at least the past 20 My. (Johnson et al., 1973; Sclater et al., 1976) and perhaps as long as 60-65 My. (Lawyer, 1984). Here, the Southern Mid-Atlantic Ridge is offset from the South American – Antarctic Ridge and the SWIR by a pair of transform faults, therefore defining the triple junction as a RFF triple junction (Figure 46C). The three major ridges involved with this triple junction do not meet at a point. The geometry and symmetrical spreading rates of the ridges involved allow for either a RFF or a RRR to exist as a kinematically-stable triple junction (Kleinrock and Morgan, 1988). They suggest that the BTJ prefers a RFF geometry based on the local tensile stress directions that, in the case of the Bouvet Triple Junction, can split a single ridge into two separate ridges, causing a RRR to evolve into a RFF. However, this assertion is challenged by Mitchell and Livermore (1998), who classify the BTJ as neither a RFF nor a RRR based on more recent marine geophysical surveying of the triple junction. Their mapping dataset, along with one collected by Ligi et al. (1997) suggest that the Southern Mid-Atlantic Ridge connects with the South American – Antarctic Ridge by an obliquely opening rift that overlaps the western edge of the SWIR known as the Spiess Ridge. Their higher resolution mapping shows that there is no evidence for a transform fault within this complex triple junction.

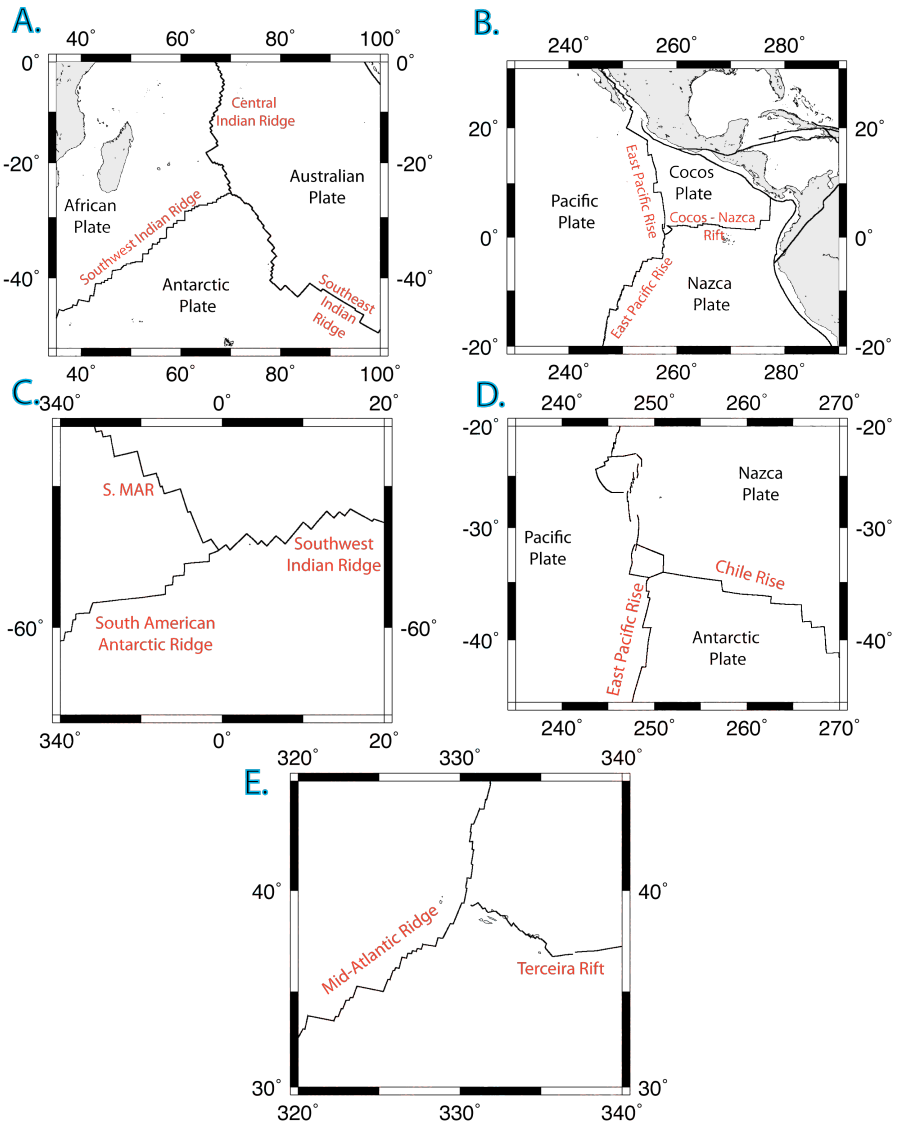

Figure 46. Regional maps of the five observed RRR triple junctions on Earth. A) The Rodriguez Triple Junction in the Central Indian Ocean, the most stable of the RRR triple junctions with an estimated kink angle of 2β=30°. Kinematic stability is proposed to be due to the velocities of the ridges and their subsequent geometry. B) The Galápagos Triple Junction in the Eastern Pacific Ocean (2β≈0°). At this RRR triple junction, the westward propagating CNR does not directly connect to the EPR. Due to the regional stress field created by the orthogonal configuration between ridges and the position of the CNR tip, two smaller RRR triple junctions are found at 1° 10'N and 2° 40'N along the EPR. C. The Bouvet Triple Junction (BTJ) in the Southern Atlantic. This triple junction oscillates between a RRR configuration with a RFF configuration and has been stable for 20 – 65 Myr. Due to the asymmetry of the ridges, the triple junction involving the three ridges do not meet at a point, making it difficult to constrain a kink angle, further suggesting a RFF configuration. D. The Easter Island or Juan Fernandez Triple Junction (ETJ)(2β≈5°). This triple junction sustains its stability through a complex interaction of a microplate and propagating rifts. The EPR ridge crest runs straight through this triple junction where it connects the Chile Rise transform fault by a smaller spreading center. E. The Azores Triple Junction (ATJ)(2β≈5°). Considered a RRF triple junction, the ATJ lacks a direct connection between the oblique Terceira Rift with the Mid-Atlantic Rift joined by the Gloria Transform Fault.

The other two RRR triple junctions currently in existence are the Azores Triple Junction (ATJ) and Easter Island Triple Junction (ETJ). Both of these triple junctions are more accurately described as joining two ridges and one transform (RRF). The transform involved in these triple junctions is commonly an offset in the third ridge. At the ATJ, the three plate boundaries do not meet at a point and contain zones of distributed deformation where the Gloria Transform Fault terminates westwards at oblique Terceira Rift. The Azores hotspot is also located at the termination of the Gloria Transform Zone. The Terceira Rift lacks a direct connection to the Mid-Atlantic Ridge (Vogt and Jung, 2004) therefore defining it as a RRF (Figure 46E). However, Fournier et al. (2008) suggest that the RRF configuration will be unstable and can only exist for a short period of time before evolving into a RFF configuration unless the RRF includes two perpendicular ridges (McKenzie and Morgan, 1969). In the case of the ATJ, the RFF configuration does not exist due to the transform fault involved in the triple junction evolving into a spreading center (Fournier et al., 2008) and because of the influence of the Azores Hotspot (Vogt and Jung, 2004).

The Easter Island Triple Junction (ETJ), also called Juan Fernandez Triple Junction, is classified as a RRF triple junction where the EPR meets the Chile Transform Fault (Figure 46D). Like the GTJ, located 3,000 km to the north along the EPR, the ETJ features a microplate, the Juan Fernandez Microplate, and contains complex seafloor features such as rotated abyssal hill fabric, and overlapping spreading centers bordering the microplates (Larson et al., 1992; MacDonald and Fox, 1983; Lonsdale 1983; Lonsdale, 1985. Fournier et al. (2008) suggest this triple

junction is not correctly classified as a RFF because of the formation of a spreading ridge that developed at the western end of the Chile Transform Fault.

While these triple junctions are the most relatively stable types of triple junctions, we can see that each of the five currently observed RRR triple junctions, the GTJ and ETJ in the Eastern Pacific Ocean, the RTJ in the Central Indian Ocean, the BTJ in the Southern Atlantic Ocean and the ATJ in the Northern Atlantic Ocean all feature unique kinematic histories that have led to their current configuration. Transient tectonic features include propagating rifts, rift axis jumping, rift detachment episodes, the accretion and formation of microplates, and evolving plate boundaries including transitions between RRR, RRF, and RFF configurations (Fournier et al., 2008). In part, these transitions arise from the segmentation of the ridges involved in the triple junction and migration of the triple junction along the ridge. For example, the Chile Rise features a long transform and short spreading segment next to the triple junction. The character of the RTJ depends on the details of segmentation of the CIR and SEIR. The mechanical instability that I document here for the Northern GTJ occasionally adds to the complexity of triple junctions by generating a series of short-lived rifts slightly off the triple plate-scale triple junction. Thus, RRR triple junctions represent very rapidly evolving plate boundaries that can lead to the seafloor complexity noted in the vicinity of the triple junctions.

Chapter 8: Summary

Recent studies of the Galápagos triple junction have shown it to be a tectonically complex ridge-ridge-ridge triple junction in which the Cocos-Nazca Rift never connects to the East Pacific Rise, but a sequence of secondary rifts has been spawned at the northern triple junction, currently marked by the Incipient Rift at 2°40 N. Approximately 25 extinct secondary rifts can be identified, among which the Extinct Rift, evaluated to be 2 My old, is the most prominent. Each one of these rifts is interpreted to be a scar of a short-lived former RRR triple junction. Each rift was detached from the East Pacific Rise and then rafted away by the motion of the Pacific and Cocos plates. This study uses several numerical models of the stress field in an elastic plate under tension, with cracks representing rifts in the vicinity of a RRR triple junction and GIS spatial analysis to characterize fully the factors that control RRR triple junction's stability. My mechanical models suggest that once tension is reduced between the tip of secondary rift and the East Pacific Rise, reconnection is mechanically prevented. However, once a rift detaches, an asymmetric double peak of stress enhancement develops along the EPR, generating a new secondary rift, slightly offset from the previous one.

Whether the new rifts are located to the south or north of the previous one is controlled by the distance between the Cocos-Nazca Rift tip and the EPR, D. A window of stability along the EPR exists at approximately $1.1\pm0.2D$ from the projection of the tip of the Cocos-Nazca Rift on the East Pacific Rise. The width of

this oscillation window is controlled by the distance between the detached rift tip and EPR. When a rift disconnects south of this stability window, the new crack will form offset to the right of the disconnected rift. These right-stepping rifts create a northward migration along the East Pacific Rise. When a rift disconnects north of the stability window, the new rift will form to the south creating a left-stepping rift sequence. Rifts disconnecting within this stability window are successively right-or left-stepping, with little or no long-term migration. I suggest that this sequence of extinct rifts found to the northeast of the 2°40' N triple junction represents a series of rift disconnection events and their position records period during which the Cocos-Nazca Rift approached the East Pacific Rise. A right-stepping sequence may have been erased by subsequent rifting, especially the Extinct Rift, which marks the last time when the gap between the Cocos-Nazca Rift and the East Pacific Rise was maximum.

The Central, Southeast, and Southwest Indian Ridges appear to be directly connected, and lack evidence for transient secondary rifts similar to those found at the GTJ (Sauter, 1997). I propose that the stability of RRR triple junctions, principally whether secondary rifts are generated or a direct connection between the spreading centers is favored, can be understood based on the mechanics of crack interaction. The difference between the GTJ and RTJ stems from the difference in the angle between the two faster ridges. At the GTJ, the EPR is essentially straight through the triple junction. In that case, tension is maximal along the EPR slightly away from where the tip CNR would connect to the EPR, preventing direct connection and favoring short-lived secondary rifts instead. At the RTJ, the angle between the Central

and Southeast Indian Ridges concentrates stress at the triple junction and favors a direct connect between the three ridges.

Although Ridge-Ridge-Ridge triple junctions are kinematically stable, rift junctions are mechanically unstable, generating a rapidly evolving and complex plate boundary. It is clear that although the kinematics of RRR triple junctions are notably stable, mechanical interaction between the rifts leads to instability, which can explain why these specific triple junction tectonics are remarkably complex.

Appendices A-E

The following appendices contain data and figures that were used throughout this study. Appendix A contains data collected during the geospatial analyses using ArcGIS and MATLAB to constrain information regarding the relative positions of the secondary rifts found at the Northern Galápagos Triple Junction. Appendix B consists of quantitative data measured from the numerical models using COMSOL and MATLAB. Appendix C contains the stress enhancement maps of the symmetrical models discussed in Section 6.2.1. Appendices D and E contains the complete numerical scripts built with COMSOL and MATLAB.

Appendix A: GIS Database

The following tables in Appendix A contain information on secondary rift lengths, azimuths, relative offsets, and the mapped geospatial data points. Table A1 refers to the GIS mapping of secondary rifts found northeast of the GTJ 2°40' N triple junction shown in Figure 5 in Section 3.1. Table A2 includes data regarding the Incipient Rift and relative offsets from adjacent rift scars shown in Figures 20 and 21 of Section 5.3. Table A3 contains geospatial information of all data points used in the GIS mapping shown in Figure 5 discussed in Chapter 3.

Table A1: Rift length and azimuth of N. GTJ secondary rifts (Figures 5 and 7)

Length (km)	Azimuth (°)	Points
59.8	99	0-1-2
28.6	106	3-4
19.3	111	5-6
66.9	107	7-8
80.1	109	22-23
65.2	116	21-20
78.4	107	24-25
77.6	112	16-15
71.4	114	17-18
26.3	118	29-28
25.1	114	27-19
45.3	111	14-13
11.9	99	11-12
11.8	96	9-10

Table A2: Relative rift positions of the Incipient and adjacent secondary rifts (Figures 20 and 21)

Point Offset	Distance (km)	Jump Azimuth (°)
3-0	30.6	261
5-3	9.9	237
26-5	22.2	273
21-7	15.0	195
16-21	13.8	249
17-16	8.8	358

Table A3: Geospatial information of all collected GIS data points

Point	Long (W)	Lat (N)	Long (E)
0	-102.08	2.66	257.92
1	-101.86	2.62	258.14
2	-101.55	2.57	258.45
3	-101.81	2.70	258.19
4	-101.56	2.63	258.44
5	-101.74	2.75	258.26
6	-101.58	2.69	258.42
7	-101.42	3.06	258.58
8	-100.84	2.88	259.16
9	-100.05	3.35	259.95
10	-99.94	3.34	260.06
11	-100.20	3.29	259.80
12	-100.10	3.28	259.90
13	-100.33	3.05	259.67
14	-100.71	3.19	259.29
15	-100.62	2.97	259.38
16	-101.27	3.23	258.73
17	-101.27	3.31	258.73
18	-100.68	3.04	259.32
19	-100.59	3.07	259.41
20	-100.86	2.94	259.14
21	-101.38	3.19	258.62
22	-101.06	2.97	258.94
23	-100.38	2.74	259.62
24	-101.10	3.05	258.90
25	-100.43	2.84	259.57
26	-101.53	2.74	258.47
27	-100.80	3.17	259.20
28	-100.67	3.07	259.33
29	-100.88	3.18	259.12

Appendix B: Model Data Tables

The following data contained in Appendix B refer to data collected from the geodynamic models constructed in COMSOL Multiphysics and analyzed in this study. Table B1 contains data on the model boundary and scaling study discussed in Section 4.2.3 and shown in Figures 9 and 10. Table B2 contains information regarding how the width and center of the rift stability window varies as a function of the detached rift distance from the East Pacific Rise. Tables B3 and B4 refer to the model integrity study exploring how the CNR's elliptical dimensions affected the base model's amplitude and position. Table B5 contains data on the tension amplitude of the center peak with side peak tension amplitude and position of symmetric models in Section 6.2.1 (Figure 32). Tables B6 and B7 refer to similar data collected on the asymmetric models in Section 6.2.2. B8 contains values of the crack propagation criteria angle vs. Incipient Rift length discussed in Section 5.4.

Table B1: Collected data on the model boundary and scaling study (Figures 9 and 10)

Dimensions	Amplitude (S)	Position (S)	Amplitude (N)	Position (N)
2x8	1.482	-1.015	1.481	1.034
3x8	1.341	-1.194	1.341	1.196
4x8	1.292	-1.254	1.292	1.261
5x8	1.270	-1.313	1.270	1.293
6x8	1.259	-1.313	1.258	1.293
7x8	1.252	-1.314	1.252	1.325
8x8	1.248	-1.314	1.247	1.325
12x8	1.242	-1.313	1.242	1.325
6x1				
6x2				
6x3	1.119	-1.200	1.119	1.200
6x4	1.113	-1.284	1.113	1.277
6x5	1.137	-1.250	1.136	1.253
6x6	1.170	-1.260	1.170	1.261
6x7	1.212	-1.286	1.212	1.301
6x8	1.259	-1.313	1.258	1.293
6x9	1.310	-1.320	1.309	1.309
6x10	1.363	-1.287	1.363	1.333

Table B2: Detached rift distance and stability window data (Figures 18 and 19)

X_IR	Center	Width (+/-)
0.2	1.122	0.24
0.18	1.127	0.21
0.16	1.123	0.18
0.14	1.101	0.15
0.12	1.131	0.15
0.1	1.065	0.12
0.08	1.112	0.09
0.06	1.083	0.09
0.04	1.022	0.06
0.02	0.9764	0.04
0.001	discretization	0.0015

Table B3: Tension amplitude and position data versus CNR Length

CNR Length	Amplitude (S)	Position (S)	Amplitude (N)	Position (N)
5	1.259	-1.313	1.258	1.293
4	1.112	-2.388	1.112	2.392
3	1.097	-3.200	1.097	3.200
2	1.081	-3.200	1.081	3.200
1	1.081	-3.200	1.081	3.200
0.5	1.076	-3.200	1.076	3.200
0.25	1.080	-3.200	1.079	3.200

Table B4: Tension amplitude and position data versus elliptical width of the CNR

Ellipse Width	Amplitude (S)	Position (S)	Amplitude (N)	Position (N)
1	1.686	-1.521	1.686	1.519
0.1	1.697	-1.360	1.697	1.358
0.01	1.695	-1.360	1.695	1.358
0.002	1.693	-1.359	1.693	1.358
0.001	1.691	-1.360	1.691	1.358
0.0001	1.679	-1.380	1.679	1.390

Table B5: Tension amplitude of the center peak with side peak tension amplitude and position of symmetric models in Section 6.2.1 (Figure 32)

(2β)	Central Amplitude	Side Amplitude	Side Position (+/-)
0.02	0.386	1.693	1.358
5	0.781	1.690	1.228
10	1.351	1.702	1.099
15	2.097	1.787	1.120
20	3.027	1.809	1.020
30	5.256	1.845	0.800
40	8.744		
50	11.920		
60	16.064		
70	17.958		
80	19.805		
100	21.933		

Table B6: Asymmetric model values (2β = 20°) of northern and southern peak tension amplitude and position (Figures 37 – 40)

Alpha	Amplitude (S)	Position (S)	Amplitude (N)	Position (N)
0	1.809	-1.020	1.809	1.020
5	1.739	-0.900	1.861	1.140
10	1.653	-0.760	1.893	1.260

Table B7: Asymmetric model values (2β = 15°) of northern and southern peak tension amplitude and position (Figures 41 – 44)

Alpha	Amplitude (S)	Position (S)	Amplitude (N)	Position (N)
0	1.787	1.120	1.787	1.120
2.5	1.750	-1.060	1.819	1.180
5	1.709	-1.000	1.845	1.240
7.5	1.497	-0.960	1.816	1.280

Table B8: Crack propagation criteria angle vs. Incipient Rift length (Section 5.4)

IR Length	$\sigma_{r\theta}$ (°)	$\sigma_{r\theta}$ (°)	S(θ)min (°)
0.1	90.5	90.6	90.3
0.2	91.4	91.0	90.2
0.3	91.8	91.6	91.1
0.4	92.9	92.5	93.0
0.5	93.9	93.7	95.7
0.6	95.6	95.3	94.2
0.7	97.7	97.1	96.4
0.8	99.7	99.1	97.6
0.9	101.9	101.3	101.4
1	104.3	103.7	104.5

Appendix C: Symmetry Model Stress Enhancement Maps

Symmetry stress enhancement maps for 2β=5, 10, 20, 40, 50, 60, 70, 80, and 100° discussed in Section 6.2.1. Maps show that when 2β ≥15°, tensile stress enhancement at the point of triple junction detachment will promote a reconnection between the major ridges forming the RRR triple junction.

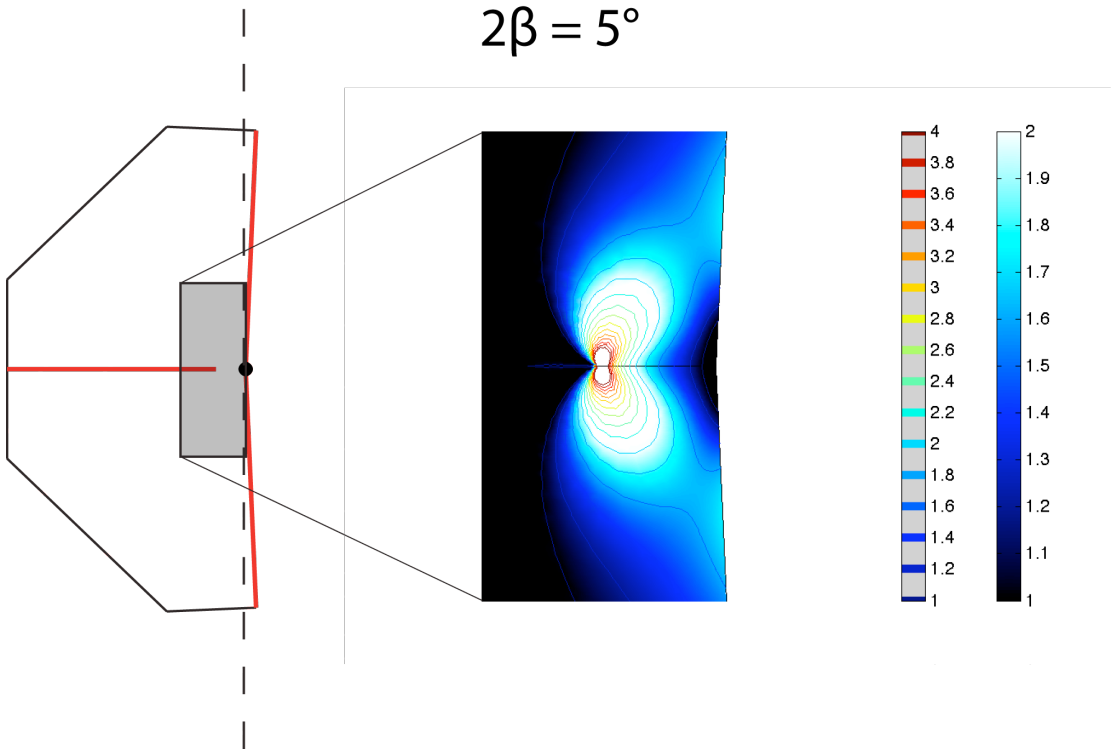

$2\beta = 10°$

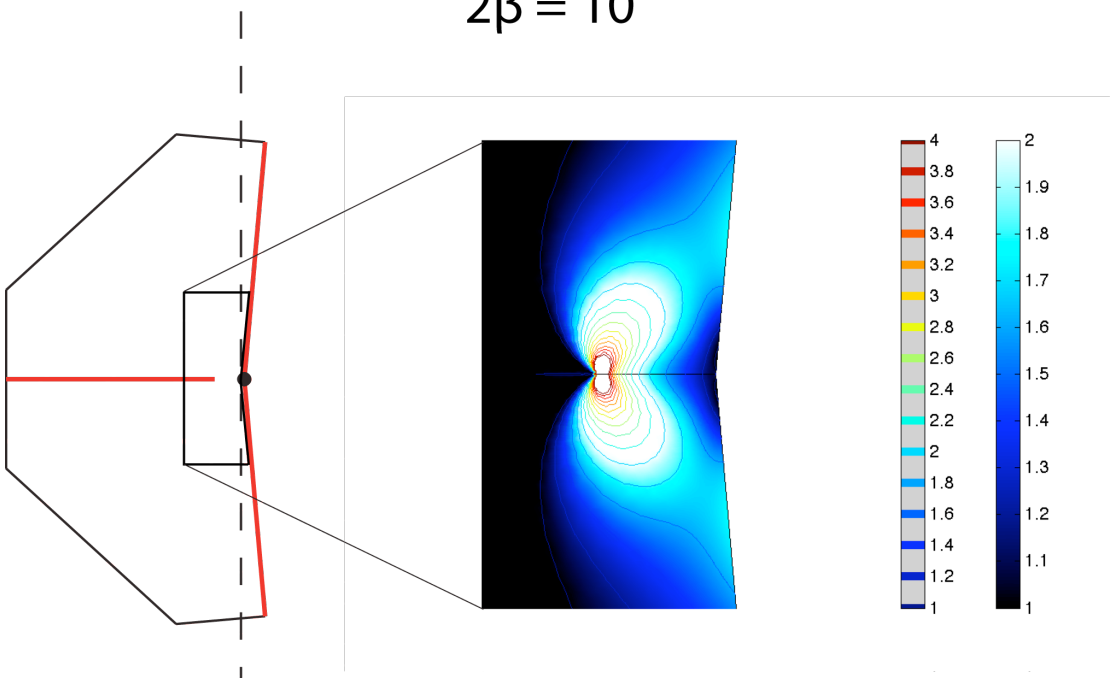

$2\beta = 20°$

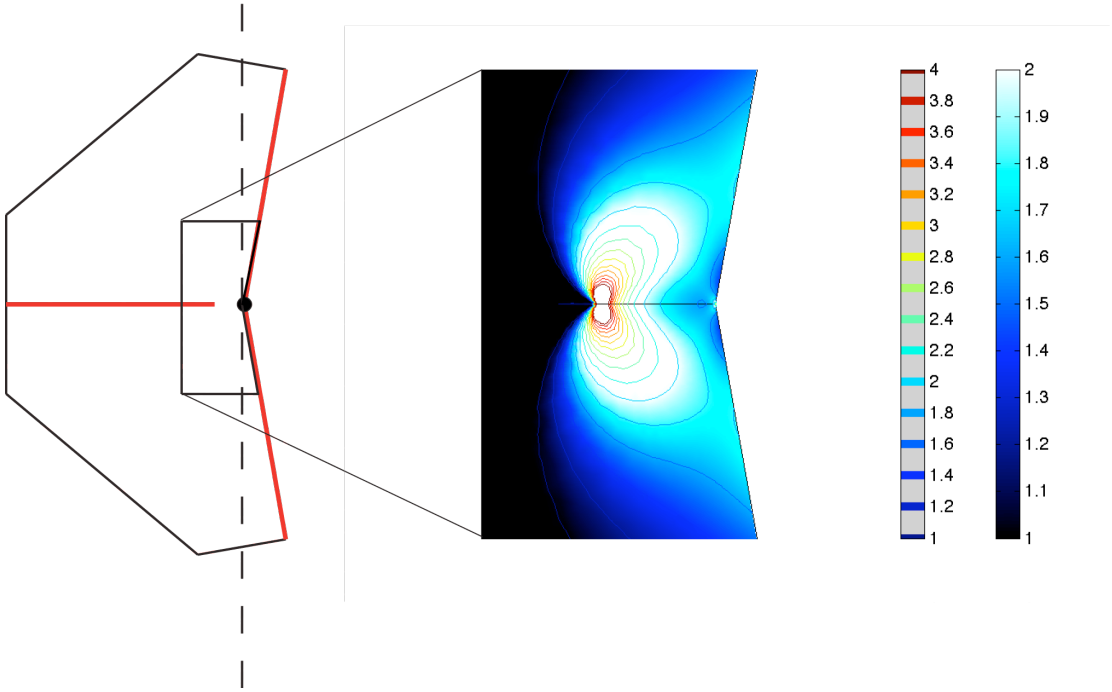

$2\beta = 40°$

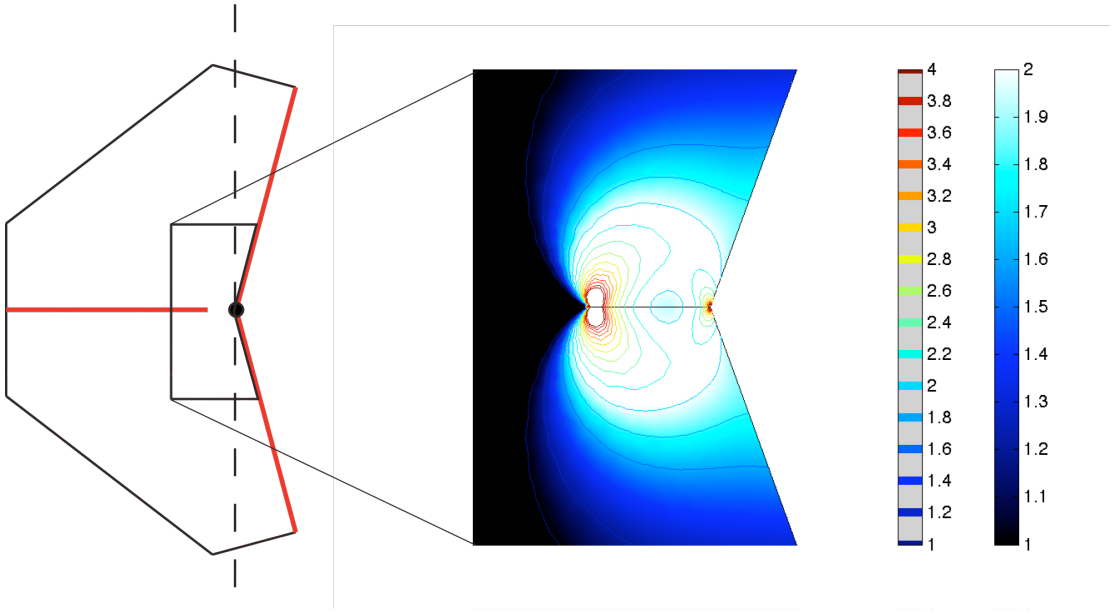

$2\beta = 50°$

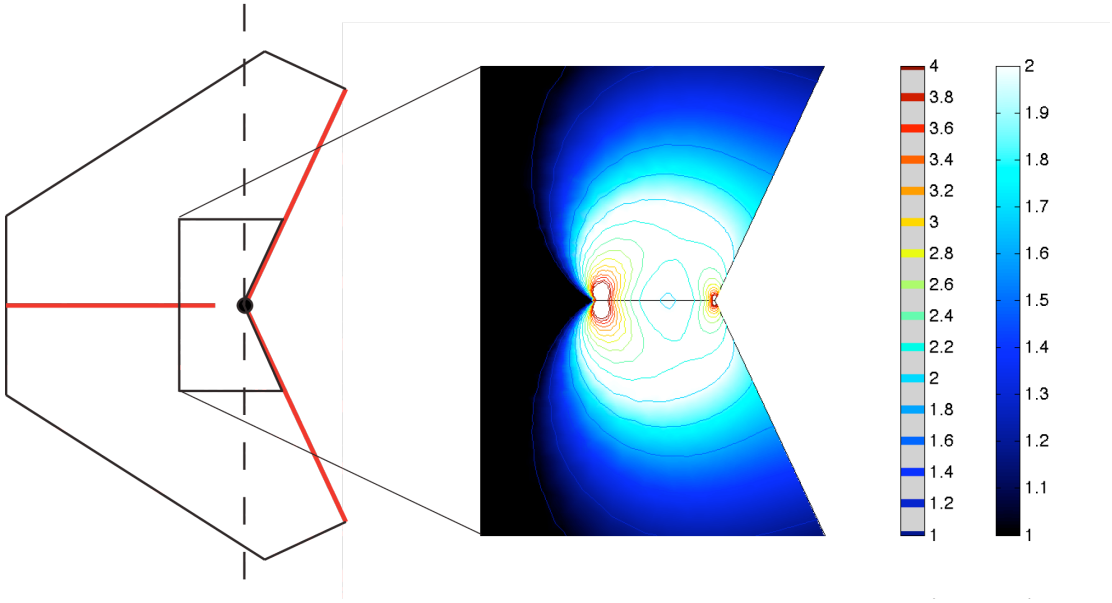

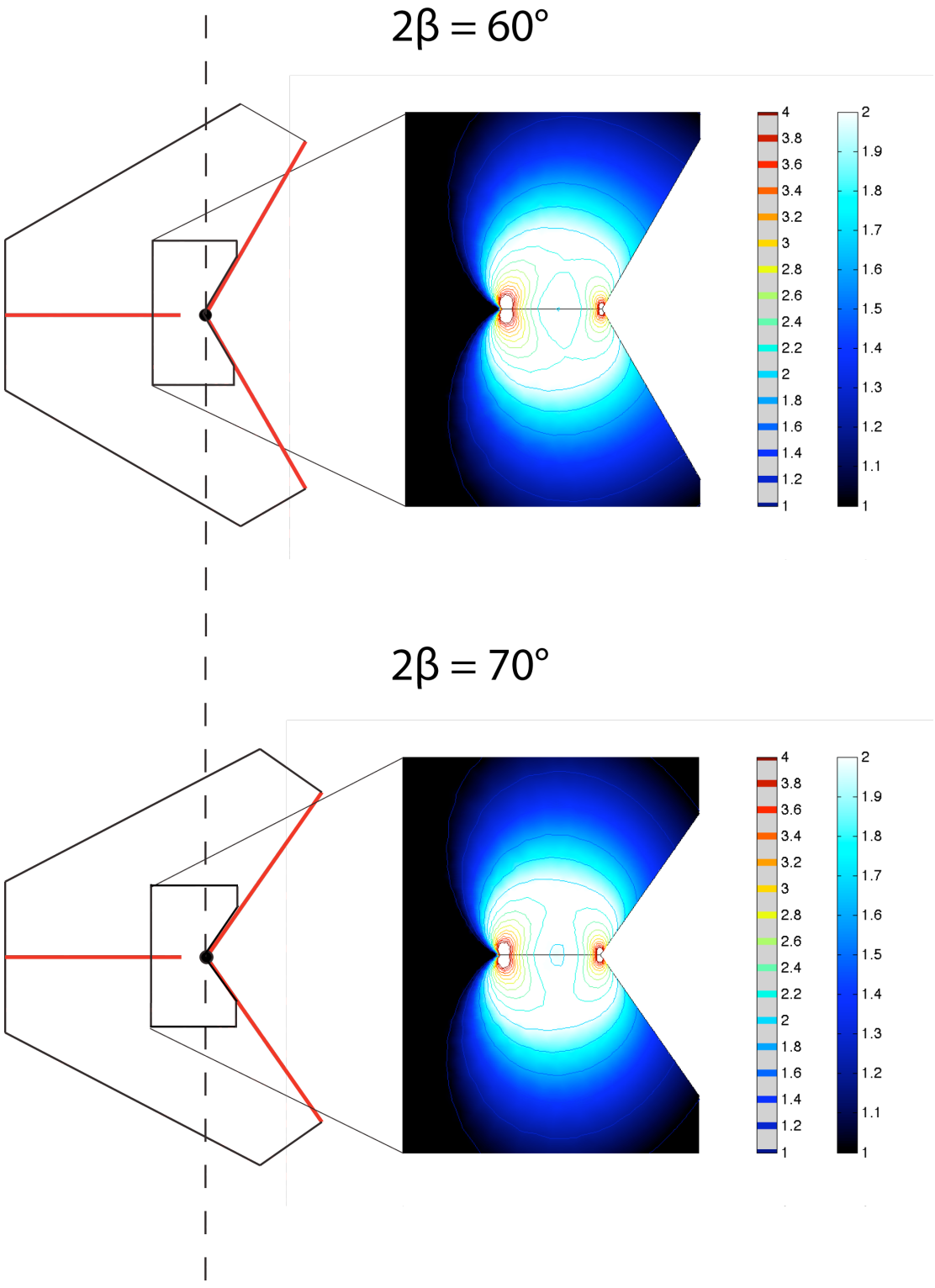
2β = 60°
4
3.8
3.6
3.4
3.2
3
2.8
2.6
2.4
2.2
2
1.8
1.6
1.4
1.2
1
2
1.9
1.8
1.7
1.6
1.5
1.4
1.3
1.2
1.1
1
2β = 70°
4
3.8
3.6
3.4
3.2
3
2.8
2.6
2.4
2.2
2
1.8
1.6
1.4
1.2
1
2
1.9
1.8
1.7
1.6
1.5
1.4
1.3
1.2
1.1
1

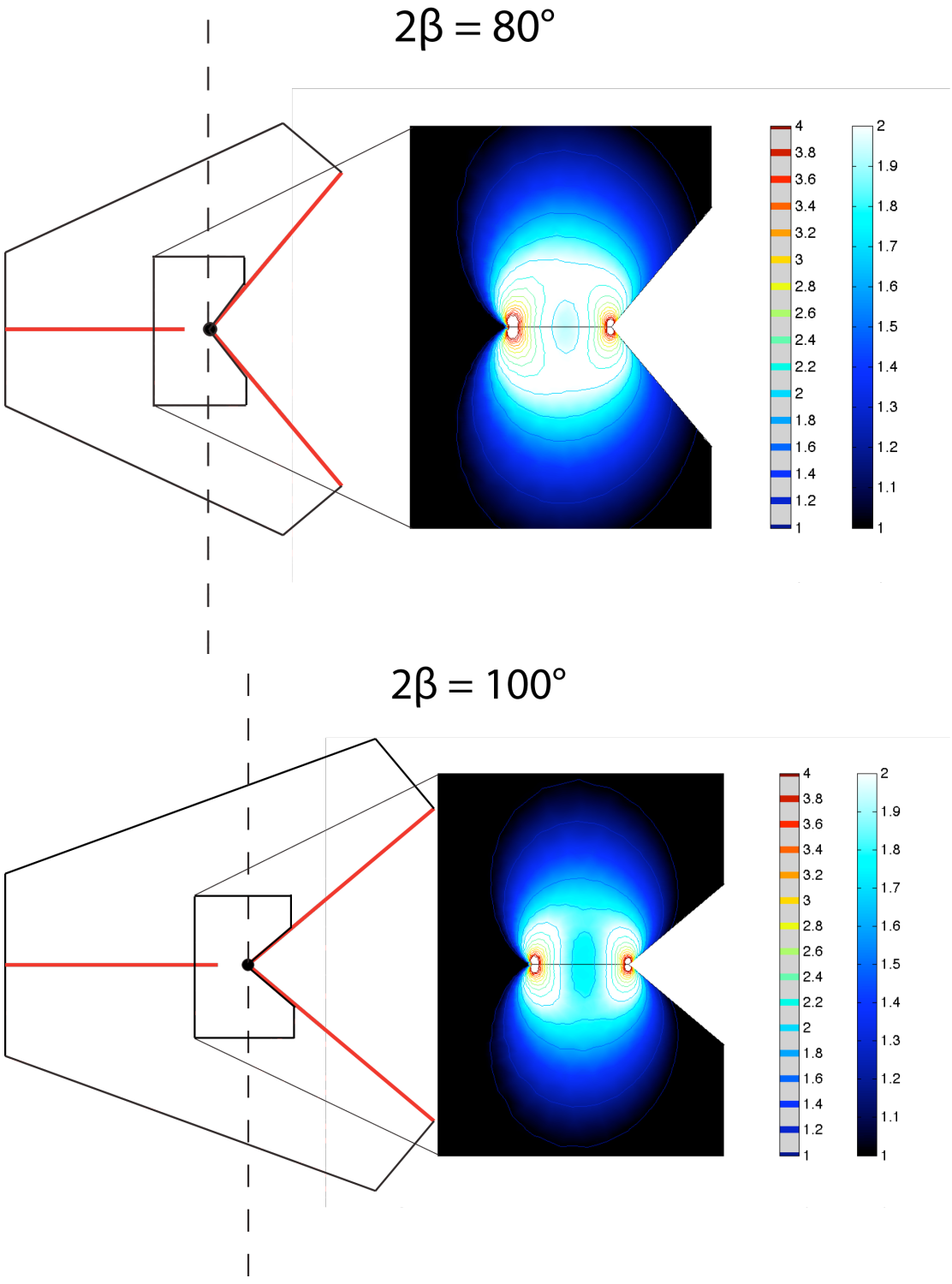
2β = 80°
4
3.8
3.6
3.4
3.2
3
2.8
2.6
2.4
2.2
2
1.8
1.6
1.4
1.2
1
2
1.9
1.8
1.7
1.6
1.5
1.4
1.3
1.2
1.1
1
2β = 100°
4
3.8
3.6
3.4
3.2
3
2.8
2.6
2.4
2.2
2
1.8
1.6
1.4
1.2
1
2
1.9
1.8
1.7
1.6
1.5
1.4
1.3
1.2
1.1
1

Appendix D: MATLAB and COMSOL Scripts for Rift Interaction

Base model
model393Hnd.m

```
% COMSOL Multiphysics Model M-file
% Generated by COMSOL 3.4 (COMSOL 3.4.0.249, $Date: 2007/10/23 11:46:22 $)

figure(1)

flclear fem

% COMSOL version
clear vrsn
vrsn.name = 'COMSOL 3.4';
vrsn.ext = '';
vrsn.major = 0;
vrsn.build = 249;
vrsn.rcs = '$Name: v34p $';
vrsn.date = '$Date: 2007/10/23 11:46:22 $';
fem.version = vrsn;

% Constants
fem.const.yr2s=365.24*24*3600;
% fem.const.VEPR=0;
fem.const.W=6; %width of plate
fem.const.H=8; %height of plate
fem.const.D=1; %distance triple junction to CNR tip
fem.const.U=fem.const.H/2; %Displacement of N bdy
fem.const.WCNR=0.002; % opening width of CNR
fem.const.LCNR=fem.const.W-fem.const.D; %lenght of CNR
% fem.const.dt=100*1000*fem.const.yr2s;

%% Geometry
g1=rect2(fem.const.W,fem.const.H,'base','corner','pos',{'0',-fem.const.H/2},'rot','0');
%define plate

%g2=ellip2(0.8,.02,'base','center','pos',{0,'1.4'},'rot','0'); % define IR
g6=ellip2(fem.const.LCNR,fem.const.WCNR,'base','center','pos',{fem.const.W,'0'},'r
ot','0'); % define CNR
g7=geomcomp({g1,g6},'ns',{'g1','g6'},'sf','g1-g6','edge','none'); %remove CNR from
plate
%g8=geomcomp({g7,g2},'ns',{'g7','g2'},'sf','g7-g2','edge','none'); %remove IR from
plate
```

```
% Analyzed geometry
clear s
s.objs={g7};
s.name={'CO1'};
s.tags={'g7'};

fem.draw=struct('s',s);
fem.geom=geomcsg(fem);

clf;
% geomplot(fem)

 % Initialize mesh
fem.mesh=meshinit(fem, ...
   'hauto',5, ...
   'hmaxedg',[1;0.06]);
% meshplot(fem)

%% (Default values are not included)

% Application mode 1
clear appl
appl.mode.class = 'SmePlaneStress';
appl.module = 'SME';
appl.gporder = 4;
appl.cporder = 2;
appl.assignsuffix = '_smps';
clear bnd
bnd.Rx = {0,0,0}; %Displacement in x-dir
bnd.Hx = {0,1,1}; %Force in x-dir
bnd.constrcond = {'free','displacement','displacement'};
bnd.Ry = {0,'-U','U'}; %Displacement in y-dir
bnd.Hy = {0,1,1}; %Force in y-dir
% bnd.ind = [1,2,3,2,3,1,1];
bnd.ind = [1,2,3,2,3,1,1];

appl.bnd = bnd;
clear equ
% equ.rho = 3300;
equ.nu = 0.25;
equ.thickness = 0.2;
equ.E = 1;
equ.ind = [1];
appl.equ = equ;
fem.appl{1} = appl;
fem.frame = {'ref'};
```

```
fem.border = 1;
clear units;
units.basesystem = 'SI';
fem.units = units;

% ODE Settings
clear ode
clear units;
units.basesystem = 'SI';
ode.units = units;
fem.ode=ode;
% Multiphysics
fem=multiphysics(fem);

%% Solve problem

 % Extend mesh
fem.xmesh=meshextend(fem);

% Solve problem
fem.sol=femstatic(fem, ...
   'solcomp',{'u','v'}, ...
   'outcomp',{'u','v'});

% Save current fem structure for restart purposes
fem0=fem;

% Plot solution
figure(3); clf
% subplot 211

postplot(fem, ...
   'tridata',{'min(s1_smps,2)','cont','internal','unit','Pa'}, ...
   'tridlim',[0 2], ...
   'trimap','jet(1024)');
hold on;
postplot(fem, ...
   'contdata',{'min(s1_smps,2)','cont','internal','unit','Pa'}, ...
   'contlevels',[1:.1:2], ...
   'contbar','off',...
   'contmap',[0 0 0]);

axis equal; axis tight;
axis([0,1.2,-2,2])
box on;
set(gca,'visible','off')
```

```
figure(2); clf
% subplot 212
% Plot in cross-section or along domain
H=postcrossplot(fem,1,[0 0;-3 3], ...
   'lindata','s1_smps', ...
   'linxdata',{'y','unit','m'});
xlabel('Distance along EPR','fontsize',18)
ylabel('Tension Enhancement','fontsize',18)
title('First principal stress','fontsize',24)
set(gca,'fontsize',18)
set(H,'linewidth',2)
axis([-3 3 0 2])
box on; grid off
hold on;
%plot([1,1]*1.3*fem.const.D/1000, [0,2],'k','linewidth',1);
%plot(-[1,1]*1.3*fem.const.D/1000, [0,2],'k','linewidth',1)
xlim([-3,3]); ylim([0,2]);
plot([1,1]*-1.35, [0,4],'k','linewidth',1);
plot([1,1]*1.35, [0,4],'k','linewidth',1);
```

IR Attached Models
IRAttached_nd.m

```
% COMSOL Multiphysics Model M-file
% Generated by COMSOL 3.4 (COMSOL 3.4.0.249, $Date: 2007/10/23 11:46:22 $)

flclear fem

% COMSOL version
clear vrsn
vrsn.name = 'COMSOL 3.4';
vrsn.ext = '';
vrsn.major = 0;
vrsn.build = 249;
vrsn.rcs = '$Name: v34p $';
vrsn.date = '$Date: 2007/10/23 11:46:22 $';
fem.version = vrsn;

% Constants
fem.const.yr2s=365.24*24*3600;
%fem.const.VEPR=0;
fem.const.VCNR=1;
fem.const.W=6; %width of plate
```

```
fem.const.H=8; %height of plate
fem.const.D=1; %distance triple junction to CNR tip
fem.const.U=fem.const.H/2; %Displacement of N bdy
fem.const.WCNR=0.002; % opening width of CNR
fem.const.LCNR=fem.const.W-fem.const.D; %length of CNR
%fem.const.dt=100*1000*fem.const.yr2s;
fem.const.Wir=0.4;

Yall=linspace(0.1,3.1,51); nY=length(Yall)
for i=1:nY; %.2:.5:3;
   fem.const.Yir=Yall(i);
   disp(sprintf('Working on Yi=%g',Yall(i)));

 %% Geometry
   g1=rect2(fem.const.W,fem.const.H,'base','corner','pos',{'0',-fem.const.H/2},'rot','0');
%define plate

   g2=ellip2(2*fem.const.Wir,.002,'base','center','pos',{0,fem.const.Yir},'rot','0'); %
define IR

g6=ellip2(fem.const.LCNR,fem.const.WCNR,'base','center','pos',{fem.const.W,'0'},'r
ot','0'); % define CNR
   g7=geomcomp({g1,g6},'ns',{'g1','g6'},'sf','g1-g6','edge','none'); %remove CNR
from plate
   g8=geomcomp({g7,g2},'ns',{'g7','g2'},'sf','g7-g2','edge','none'); %remove IR from
plate
  % Analyzed geometry
   clear s
   s.objs={g8};
   s.name={'CO1'};
   s.tags={'g8'};

   fem.draw=struct('s',s);
   fem.geom=geomcsg(fem);
  % Initialize mesh
   fem.mesh=meshinit(fem, ...
      'hauto',5, ...
      'hmaxedg',[1;0.06;3;0.06]);

   % Application mode 1
   clear appl
   appl.mode.class = 'SmePlaneStress';
   appl.module = 'SME';
   appl.gporder = 4;
   appl.cporder = 2;
   appl.assignsuffix = '_smps';
```

```
clear bnd
bnd.Rx = {0,0,0}; %Displacement in x-dir
bnd.Hx = {0,1,1}; %Force in x-dir
bnd.constrcond = {'free','displacement','displacement'};
bnd.Ry = {0,'-U','U'}; %Displacement in y-dir
bnd.Hy = {0,1,1}; %Force in y-dir
% bnd.ind = [1,2,3,2,3,1,1];
%          1 2 3 4 5 6 7 8 9 0
bnd.ind = [1,2,1,3,2,3,1,1,1,1];

appl.bnd = bnd;
clear equ
%equ.rho = 3300;
equ.nu = 0.25;
equ.thickness = .2;
equ.E = 1;
equ.ind = [1];
appl.equ = equ;
fem.appl{1} = appl;
fem.frame = {'ref'};
fem.border = 1;
clear units;
units.basesystem = 'SI';
fem.units = units;

% ODE Settings
clear ode
clear units;
units.basesystem = 'SI';
ode.units = units;
fem.ode=ode;
% Multiphysics
fem=multiphysics(fem);

%% Solve problem

% Extend mesh
fem.xmesh=meshextend(fem);

% Solve problem
fem.sol=femstatic(fem, ...
    'solcomp',{'u','v'}, ...
    'outcomp',{'u','v'});

% Save current fem structure for restart purposes
fem0=fem;
```

```
   Hm=-fem.const.H/2*.8; Yr=fem.const.Yir; HM=fem.const.H/2*.8;
   [Amax(i,:),ymax(i,:)]=FindMax(fem,Hm,Yr,HM);
 end

%%
   figure(3); clf;
   subplot(211)
   plot(Yall,ymax);
   title('Position of Tensile Stress Enhancement','fontsize',22)

   hold on; plot(Yall,Yall,'k--')
   ylim([Hm,HM])
   subplot(212)
   plot(Yall,Amax)
   title('Amplitude of Tensile Stress Enhancement','fontsize',22)
```

IR Detached
model_393HIR_Near_nd.m

```
% COMSOL Multiphysics Model M-file
% Generated by COMSOL 3.4 (COMSOL 3.4.0.249, $Date: 2007/10/23 11:46:22 $)

flclear fem

% COMSOL version
clear vrsn
vrsn.name = 'COMSOL 3.4';
vrsn.ext = '';
vrsn.major = 0;
vrsn.build = 249;
vrsn.rcs = '$Name: v34p $';
vrsn.date = '$Date: 2007/10/23 11:46:22 $';
fem.version = vrsn;

% Constants
fem.const.yr2s=365.24*24*3600;
%fem.const.VEPR=0;
fem.const.VCNR=1;
fem.const.W=6; %width of plate
fem.const.H=8; %height of plate
fem.const.D=1; %distance triple junction to CNR tip
fem.const.U=fem.const.H/2; %Displacement of N bdy
fem.const.WCNR=0.002; % opening width of CNR
fem.const.LCNR=fem.const.W-fem.const.D; %lenght of CNR
```

```
%fem.const.dt=100*1000*fem.const.yr2s;
fem.const.Wir=0.4;
Yall=linspace(0.1,2.9,50); nY=length(Yall);
for i=1:nY; %.2:.4:3;
   fem.const.Yir=Yall(i);
   disp(sprintf('Working on Yi=%g',Yall(i)));

 %% Geometry
   g1=rect2(fem.const.W,fem.const.H,'base','corner','pos',{'0',-fem.const.H/2},'rot','0');
%define plate

   g2=ellip2(0.4,.002,'base','center','pos',{0.5,fem.const.Yir},'rot','0'); % define IR

g6=ellip2(fem.const.LCNR,fem.const.WCNR,'base','center','pos',{fem.const.W,'0'},'r
ot','0'); % define CNR
   g7=geomcomp({g1,g6},'ns',{'g1','g6'},'sf','g1-g6','edge','none'); %remove CNR
from plate
   g8=geomcomp({g7,g2},'ns',{'g7','g2'},'sf','g7-g2','edge','none'); %remove IR from
plate

   % Analyzed geometry
   clear s
   s.objs={g8};
   s.name={'CO1'};
   s.tags={'g8'};

   fem.draw=struct('s',s);
   fem.geom=geomcsg(fem);

   clf;
   geomplot(fem)

 %% Initialize mesh
   fem.mesh=meshinit(fem, ...
      'hauto',5, ...
      'hmaxedg',[1;0.06]);
   meshplot(fem)

   %% (Default values are not included)

   % Application mode 1
   clear appl
   appl.mode.class = 'SmePlaneStress';
   appl.module = 'SME';
   appl.gporder = 4;
   appl.cporder = 2;
```

```
appl.assignsuffix = '_smps';
clear bnd
% Type 1: Free
% Type 2: Nazca plate
% Type 3: Cocos plate
bnd.Rx = {0,0,0}; %Displacement in x-dir
bnd.Hx = {0,1,1}; %Force in x-dir
bnd.constrcond = {'free','displacement','displacement'};
bnd.Ry = {0,'-U','U'}; %Displacement in y-dir
bnd.Hy = {0,1,1}; %Force in y-dir
% base model: CNR only
% bnd.ind = [1,2,3,2,3,1,1];
% IR model: CNR + open IR
% bnd.ind = [1,2,1,3,2,3,1,1,1,1];
% IR_detached: CNR + closed IR
%          1 2 3 4 5 6 7 8 9 0
bnd.ind = [1,2,3,2,3,1,1,1,1,1,1];

appl.bnd = bnd;
clear equ
%equ.rho = 3300;
equ.nu = 0.25;
equ.thickness = 0.2;
equ.E = 1;
equ.ind = [1];
appl.equ = equ;
fem.appl{1} = appl;
fem.frame = {'ref'};
fem.border = 1;
clear units;
units.basesystem = 'SI';
fem.units = units;

% ODE Settings
clear ode
clear units;
units.basesystem = 'SI';
ode.units = units;
fem.ode=ode;
% Multiphysics
fem=multiphysics(fem);

%% Solve problem


% Extend mesh
```

```
    fem.xmesh=meshextend(fem);

    % Solve problem
    fem.sol=femstatic(fem, ...
      'solcomp',{'u','v'}, ...
      'outcomp',{'u','v'});

    % Save current fem structure for restart purposes
    fem0=fem;


    Hm=-fem.const.H/2*.8; Yr=fem.const.Yir; HM=fem.const.H/2*.8;
    [Amax(i,:),ymax(i,:)]=FindMax(fem,Hm,Yr,HM);

end

%%
    figure(3); clf;
    subplot(211)
    plot(Yall,ymax);
    title('Peak Position of Stress Enhancement','fontsize',22)

    hold on; plot(Yall,Yall,'k--')
    ylim([0,HM])


    subplot(212)
    plot(Yall,Amax)
    title('Peak Amplitude of Stress Enhancement','fontsize',22)
```

Uncertainty for Base Model
model393H_nd_res1_006.m

```
% COMSOL Multiphysics Model M-file
% Generated by COMSOL 3.4 (COMSOL 3.4.0.249, $Date: 2007/10/23 11:46:22 $)

figure(1)

flclear fem

% COMSOL version
clear vrsn
vrsn.name = 'COMSOL 3.4';
vrsn.ext = '';
vrsn.major = 0;
vrsn.build = 249;
```

```
vrsn.rcs = '$Name: v34p $';
vrsn.date = '$Date: 2007/10/23 11:46:22 $';
fem.version = vrsn;

% Constants
fem.const.yr2s=365.24*24*3600;
% fem.const.VEPR=0;
fem.const.W=6; %width of plate
fem.const.H=8; %height of plate
fem.const.D=1; %distance triple junction to CNR tip
fem.const.U=fem.const.H/2; %Displacement of N bdy
fem.const.WCNR=0.002; % opening width of CNR
fem.const.LCNR=fem.const.W-fem.const.D; %lenght of CNR
% fem.const.dt=100*1000*fem.const.yr2s;

%% Geometry
g1=rect2(fem.const.W,fem.const.H,'base','corner','pos',{'0',-fem.const.H/2},'rot','0');
%define plate

%g2=ellip2(0.8,.02,'base','center','pos',{0,'1.4'},'rot','0'); % define IR
g6=ellip2(fem.const.LCNR,fem.const.WCNR,'base','center','pos',{fem.const.W,'0'},'r
ot','0'); % define CNR
g7=geomcomp({g1,g6},'ns',{'g1','g6'},'sf','g1-g6','edge','none'); %remove CNR from
plate
%g8=geomcomp({g7,g2},'ns',{'g7','g2'},'sf','g7-g2','edge','none'); %remove IR from
plate

% Analyzed geometry
clear s
s.objs={g7};
s.name={'CO1'};
s.tags={'g7'};

fem.draw=struct('s',s);
fem.geom=geomcsg(fem);

clf;
% geomplot(fem)

%% Initialize mesh
   fem.mesh=meshinit(fem, ...
      'hauto',5, ...
      'hmaxedg',[1;0.06]);
   meshplot(fem)
   %% (Default values are not included)
```

```
% Application mode 1
clear appl
appl.mode.class = 'SmePlaneStress';
appl.module = 'SME';
appl.gporder = 4;
appl.cporder = 2;
appl.assignsuffix = '_smps';
clear bnd
bnd.Rx = {0,0,0}; %Displacement in x-dir
bnd.Hx = {0,1,1}; %Force in x-dir
bnd.constrcond = {'free','displacement','displacement'};
bnd.Ry = {0,'-U','U'}; %Displacement in y-dir
bnd.Hy = {0,1,1}; %Force in y-dir
% bnd.ind = [1,2,3,2,3,1,1];
bnd.ind = [1,2,3,2,3,1,1];

appl.bnd = bnd;
clear equ
% equ.rho = 3300;
equ.nu = 0.25;
equ.thickness = 0.2;
equ.E = 1;
equ.ind = [1];
appl.equ = equ;
fem.appl{1} = appl;
fem.frame = {'ref'};
fem.border = 1;
clear units;
units.basesystem = 'SI';
fem.units = units;

% ODE Settings
clear ode
clear units;
units.basesystem = 'SI';
ode.units = units;
fem.ode=ode;
% Multiphysics
fem=multiphysics(fem);

%% Solve problem


% Extend mesh
fem.xmesh=meshextend(fem);
```

```
    % Solve problem
    fem.sol=femstatic(fem, ...
       'solcomp',{'u','v'}, ...
       'outcomp',{'u','v'});

    % Save current fem structure for restart purposes
    fem0=fem;
 Hm=-fem.const.H/2*.8; Yr=0;%fem.const.Yir;
    HM=fem.const.H/2*.8;
    [Amax(j,:),ymax(j,:)]=FindMax(fem,Hm,Yr,HM);
 %%
figure(3); clf;
subplot(211)

fill([0.001,0.001,1,1,0.001],1.3+0.02*[1,-1,-1,1,1],[1,1,1]*0.75)
hold on;
plot(R,abs(ymax));
plot([1,1]*0.06,[0,2],'k');
set(gca,'xscale','log')
title('Peak Position of Stress Enhancement','fontsize',22)
box on
% hold on; plot(Yall,Yall,'k--')
% ylim([Hm,HM])
ylim([1.15,1.45]);
subplot(212)
hold on;
fill([0.001,0.001,1,1,0.001],1.259+0.002*[1,-1,-1,1,1],[1,1,1]*0.75)
plot(R,Amax)
plot([1,1]*0.06,[0,2],'k');
set(gca,'xscale','log')
title('Peak Amplitude of Stress Enhancement','fontsize',22)
ylim([1.24,1.28]);
box on
```

Uncertainty for IR Detached Model
model_393H_IRDetached_1_nd_res1.m

```
% COMSOL Multiphysics Model M-file
% Generated by COMSOL 3.4 (COMSOL 3.4.0.249, $Date: 2007/10/23 11:46:22 $)

flclear fem

% COMSOL version
clear vrsn
vrsn.name = 'COMSOL 3.4';
```

```
vrsn.ext = '';
vrsn.major = 0;
vrsn.build = 249;
vrsn.rcs = '$Name: v34p $';
vrsn.date = '$Date: 2007/10/23 11:46:22 $';
fem.version = vrsn;

% Constants
fem.const.yr2s=365.24*24*3600;
%fem.const.VEPR=0;
fem.const.VCNR=1;
fem.const.W=6; %width of plate
fem.const.H=8; %height of plate
fem.const.D=1; %distance triple junction to CNR tip
fem.const.U=fem.const.H/2; %Displacement of N bdy
fem.const.WCNR=0.002; % opening width of CNR
fem.const.LCNR=fem.const.W-fem.const.D; %lenght of CNR
%fem.const.dt=100*1000*fem.const.yr2s;
fem.const.Wir=.4;

%% Geometry
g1=rect2(fem.const.W,fem.const.H,'base','corner','pos',{'0',-fem.const.H/2},'rot','0');
%define plate

g2=ellip2(.4,.002,'base','center','pos',{.665,'1.61'},'rot','0'); % define IR
g6=ellip2(fem.const.LCNR,fem.const.WCNR,'base','center','pos',{fem.const.W,'0'},'r
ot','0'); % define CNR
g7=geomcomp({g1,g6},'ns',{'g1','g6'},'sf','g1-g6','edge','none'); %remove CNR from
plate
g8=geomcomp({g7,g2},'ns',{'g7','g2'},'sf','g7-g2','edge','none'); %remove IR from
plate

% Analyzed geometry
clear s
s.objs={g8};
s.name={'CO1'};
s.tags={'g8'};

fem.draw=struct('s',s);
fem.geom=geomcsg(fem);

clf;
geomplot(fem)


%% Initialize mesh
```

```
R=10.^[linspace(-3,0,9)]; nR=length(R)
for j=1:nR %0.06:0.02:0.12
%     fem.const.mesh=R(j)

    fem.mesh=meshinit(fem, ...
       'hauto',5, ...
       'hmaxedg',[1;R(j)]);
    meshplot(fem)

    %% (Default values are not included)

    % Application mode 1
    clear appl
    appl.mode.class = 'SmePlaneStress';
    appl.module = 'SME';
    appl.gporder = 4;
    appl.cporder = 2;
    appl.assignsuffix = '_smps';
    clear bnd
    bnd.Rx = {0,0,0}; %Displacement in x-dir
    bnd.Hx = {0,1,1}; %Force in x-dir
    bnd.constrcond = {'free','displacement','displacement'};
    bnd.Ry = {0,'-U','U'}; %Displacement in y-dir
    bnd.Hy = {0,1,1}; %Force in y-dir
    % bnd.ind = [1,2,3,2,3,1,1];
    bnd.ind = [1,2,3,2,3,1,1];

    appl.bnd = bnd;
    clear equ
    % equ.rho = 3300;
    equ.nu = 0.25;
    equ.thickness = 0.2;
    equ.E = 1;
    equ.ind = [1];
    appl.equ = equ;
    fem.appl{1} = appl;
    fem.frame = {'ref'};
    fem.border = 1;
    clear units;
    units.basesystem = 'SI';
    fem.units = units;

    % ODE Settings
    clear ode
    clear units;
    units.basesystem = 'SI';
```

```
    ode.units = units;
    fem.ode=ode;
    % Multiphysics
    fem=multiphysics(fem);

    %% Solve problem
 % Extend mesh
    fem.xmesh=meshextend(fem);

    % Solve problem
    fem.sol=femstatic(fem, ...
       'solcomp',{'u','v'}, ...
       'outcomp',{'u','v'});

    % Save current fem structure for restart purposes
    fem0=fem;

    Hm=-fem.const.H/2*.8; Yr=0;%fem.const.Yir;
    HM=fem.const.H/2*.8;
    [Amax(j,:),ymax(j,:)]=FindMax(fem,Hm,Yr,HM);

end

%%
figure(3); clf;
subplot(211)

fill([0.001,0.001,1,1,0.001],1.3+0.02*[1,-1,-1,1,1],[1,1,1]*0.75)
hold on;
plot(R,abs(ymax));
plot([1,1]*0.06,[0,2],'k');
set(gca,'xscale','log')
title('Peak Position of Stress Enhancement','fontsize',22)
box on
% hold on; plot(Yall,Yall,'k--')
% ylim([Hm,HM])
ylim([1.15,1.45]);



subplot(212)
hold on;
fill([0.001,0.001,1,1,0.001],1.26+0.01*[1,-1,-1,1,1],[1,1,1]*0.75)
plot(R,Amax)
plot([1,1]*0.06,[0,2],'k');
set(gca,'xscale','log')
```

```
title('Peak Amplitude of Stress Enhancement','fontsize',22)
ylim([1.2,1.3]);
box on
```

Rift Propagation

model_IRattached1.4D_propagation.m

```
% COMSOL Multiphysics Model M-file
% Generated by COMSOL 3.4 (COMSOL 3.4.0.249, $Date: 2007/10/23 11:46:22 $)

flclear fem

% COMSOL version
clear vrsn
vrsn.name = 'COMSOL 3.4';
vrsn.ext = '';
vrsn.major = 0;
vrsn.build = 249;
vrsn.rcs = '$Name: v34p $';
vrsn.date = '$Date: 2007/10/23 11:46:22 $';
fem.version = vrsn;

% Constants
fem.const.yr2s=365.24*24*3600;
%fem.const.VEPR=0;
fem.const.VCNR=1;
fem.const.W=6; %width of plate
fem.const.H=8; %height of plate
fem.const.D=1; %distance triple junction to CNR tip
fem.const.U=fem.const.H/2; %Displacement of N bdy
fem.const.WCNR=0.002; % opening width of CNR
fem.const.LCNR=fem.const.W-fem.const.D; %length of CNR
%fem.const.dt=100*1000*fem.const.yr2s;
fem.const.Wir=0.4;

%% Geometry
g1=rect2(fem.const.W,fem.const.H,'base','corner','pos',{'0',-fem.const.H/2},'rot','0');
%define plate

g2=ellip2(2*fem.const.Wir,.002,'base','center','pos',{0,1.4},'rot','0'); % define IR
g6=ellip2(fem.const.LCNR,fem.const.WCNR,'base','center','pos',{fem.const.W,'0'},'r
ot','0'); % define CNR
g7=geomcomp({g1,g6},'ns',{'g1','g6'},'sf','g1-g6','edge','none'); %remove CNR from
plate
g8=geomcomp({g7,g2},'ns',{'g7','g2'},'sf','g7-g2','edge','none'); %remove IR from
```

plate

```
% Analyzed geometry
clear s
s.objs={g8};
s.name={'CO1'};
s.tags={'g8'};

fem.draw=struct('s',s);
fem.geom=geomcsg(fem);

 % Initialize mesh
fem.mesh=meshinit(fem, ...
    'hauto',2, ...
    'hmaxedg',[1;0.06;3;0.06]);

%% (Default values are not included)
 % Application mode 1
clear appl
appl.mode.class = 'SmePlaneStress';
appl.module = 'SME';
appl.gporder = 4;
appl.cporder = 2;
appl.assignsuffix = '_smps';
clear bnd
bnd.Rx = {0,0,0}; %Displacement in x-dir
bnd.Hx = {0,1,1}; %Force in x-dir
bnd.constrcond = {'free','displacement','displacement'};
bnd.Ry = {0,'-U','U'}; %Displacement in y-dir
bnd.Hy = {0,1,1}; %Force in y-dir
bnd.ind = [1,2,1,3,2,3,1,1,1,1];
appl.bnd = bnd;
clear equ
%equ.rho = 3300;
equ.nu = 0.25;
equ.thickness = .2;
equ.E = 1;
equ.ind = 1;
appl.equ = equ;
fem.appl{1} = appl;
fem.frame = {'ref'};
fem.border = 1;
clear units;
units.basesystem = 'SI';
fem.units = units;
```

```
% ODE Settings
clear ode
clear units;
units.basesystem = 'SI';
ode.units = units;
fem.ode=ode;
% Multiphysics
fem=multiphysics(fem);

%% Solve problem
% Extend mesh
fem.xmesh=meshextend(fem);

% Solve problem
fem.sol=femstatic(fem, ...
   'solcomp',{'u','v'}, ...
   'outcomp',{'u','v'});

% Save current fem structure for restart purposes
fem0=fem;
%
% Plot solution
figure(1); clf
% subplot 211

postplot(fem, ...
   'tridata',{'min(s1_smps,2)','cont','internal','unit','Pa'}, ...
   'tridlim',[0 2], ...
   'trimap','jet(1024)');
hold on;
postplot(fem, ...
   'contdata',{'min(s1_smps,2)','cont','internal','unit','Pa'}, ...
   'contlevels',1:.1:2, ...
   'contbar','off',...
   'contmap',[0 0 0]);

axis equal; axis tight;
axis([0,2,-0.5,2])
box on;
set(gca,'visible','off')
```

StressSampleCircle.m

```
function [sxx,syy,sxy,srr,stt,srt,str,x0,y0,th0,x1,y1,th1,xn,yn,thn]=...
   StressSampleCircle(fem,xt,yt,r,theta)
```

```
warning off
x=xt+r*cos(theta);
y=yt+r*sin(theta);

p=[x(:)';y(:)'];
[sxx,syy,sxy,str] = postinterp(fem, 'sx_smps', 'sy_smps', 'sxy_smps','Ws_smps', p);
srr=sxx.*(cos(theta).^2)+syy.*(sin(theta).^2)+2*sxy.*cos(theta).*sin(theta);
stt=sxx.*(sin(theta).^2)+syy.*(cos(theta).^2)-2*sxy.*cos(theta).*sin(theta);
srt=(-sxx+syy).*sin(theta).*cos(theta)+sxy.*(cos(theta).^2-sin(theta).^2);

thinit=mean(theta);
th0=fsolve(@(th)interp1(theta,srt,th),thinit,optimset('display','off'));
x0=xt+r*cos(th0);
y0=yt+r*sin(th0);

% th1=fsolve(@(th)interp1((theta(1:end-1)+theta(2:end))/2,diff(stt),th),...
%     thinit,optimset('display','off'));
th1=fsolve(@(th)interp1(theta,gradient(stt),th),...
   thinit,optimset('display','off'));
% th1=fzero(@(th)interp1(theta,gradient(stt,mean(diff(theta))),th),...
%     thinit+[-1,1]*pi/4,optimset('display','off'));
x1=xt+r*cos(th1);
y1=yt+r*sin(th1);

% sn=(sxx+syy+((sxx-
syy).*(sxx.^2+syy.^2).^(1/2)+4*sxy.^2)./((sxx.^2+syy.^2+4*sxy.^2).^(1/2)))/2;
% thn=fsolve(@(th)interp1((theta(1:end-1)+theta(2:end))/2,diff(str),th),...
%     thinit,optimset('display','off'));
thn=fsolve(@(th)interp1(theta,gradient(str),th),...
   thinit,optimset('display','off'));
xn=xt+r*cos(thn);
yn=yt+r*sin(thn);
warning on

return
```

Propagation.m

```
%% sample small crack
n=75;
theta=linspace(-pi,pi,n);
R=[0.01:0.05:1]*2/3;
xIR=0.8;yIR=1.4;cIR=0.8;
xCNR=1;yCNR=0;cCNR=5;
%
```

```
clear x0IR y0IR th0IR x0CNR y0CNR th0CNR
clear x1IR y1IR th1IR x1CNR y1CNR th1CNR
clear xnIR ynIR thnIR xnCNR ynCNR thnCNR
clear sxxIR syyIR sxyIR srrIR sttIR srtIR
clear sxxCNR syyCNR sxyCNR srrCNR sttCNR srtCNR
clear strIR strCNR
for ir=1:numel(R);
   r=R(ir);%1-10^(-ir);

[sxxIR(1:n,ir),syyIR(1:n,ir),sxyIR(1:n,ir),srrIR(1:n,ir),sttIR(1:n,ir),srtIR(1:n,ir),strIR(
1:n,ir),...

x0IR(ir),y0IR(ir),th0IR(ir),x1IR(ir),y1IR(ir),th1IR(ir),xnIR(ir),ynIR(ir),thnIR(ir)]=...
      StressSampleCircle(fem,xIR,yIR,r,theta);

[sxxCNR(1:n,ir),syyCNR(1:n,ir),sxyCNR(1:n,ir),srrCNR(1:n,ir),sttCNR(1:n,ir),srtCN
R(1:n,ir),strCNR(1:n,ir),...

x0CNR(ir),y0CNR(ir),th0CNR(ir),x1CNR(ir),y1CNR(ir),th1CNR(ir),xnCNR(ir),ynC
NR(ir),thnCNR(ir)]=...
      StressSampleCircle(fem,xCNR,yCNR,r,theta+pi);
   % disp(sprintf('for IR: [x,y,th]_0=[%g,%g,%g]; for CNR: [x,y,th]=[%g,%g,%g]',...
   %     x0IR,y0IR,rad2deg(th0IR),x0CNR,y0CNR,rad2deg(th0IR)));
end
%
figure(1);
clf;
geomplot(fem,'submode','off');
hold on;
plot(x0IR,y0IR,'r','linewidth',2);
plot(x0CNR,y0CNR,'r','linewidth',2);
plot(x1IR,y1IR,'color',[0,0.5,0],'linewidth',2);
plot(x1CNR,y1CNR,'color',[0,0.5,0],'linewidth',2);
plot(xnIR,ynIR,'m','linewidth',2);
plot(xnCNR,ynCNR,'m','linewidth',2);
axis equal;axis([0,2,-0.5,2]);

%%
ir=3;
figure(1);
plot(xIR+R(ir)*cos(theta),yIR+R(ir)*sin(theta),'k');
plot(xCNR+R(ir)*cos(theta),yCNR+R(ir)*sin(theta),'k');
figure(2); clf
hold on;
subplot(211)
hold
```

```
plot(theta,[sxxIR(:,ir),syyIR(:,ir),sxyIR(:,ir)]')
plot(theta,strIR(:,ir)','m')
plot(theta,[sxxCNR(:,ir),syyCNR(:,ir),sxyCNR(:,ir)]','--')
plot(theta,strCNR(:,ir)','m--')
YL=get(gca,'ylim');
plot(th0IR(ir)*[1,1],YL,'r');plot(th0CNR(ir)*[1,1],YL,'r--');
plot(th1IR(ir)*[1,1],YL,'color',[0,0.5,0]);plot(th1CNR(ir)*[1,1],YL,'--
','color',[0,0.5,0]);
plot(thnIR(ir)*[1,1],YL,'m');plot(thnCNR(ir)*[1,1],YL,'m--');
legend('sxx','syy','sxy')
box on
set(gca,'xlim',[-1,1]*pi);
%
subplot(212)
hold on;
plot(theta,[srrIR(:,ir),sttIR(:,ir),srtIR(:,ir)]')
plot(theta,strIR(:,ir)','m')
plot(theta,[srrCNR(:,ir),sttCNR(:,ir),srtCNR(:,ir)]','--')
plot(theta,strCNR(:,ir)','m--')
YL=get(gca,'ylim');
plot(th0IR(ir)*[1,1],YL,'r');plot(th0CNR(ir)*[1,1],YL,'r--');
plot(th1IR(ir)*[1,1],YL,'color',[0,0.5,0]);plot(th1CNR(ir)*[1,1],YL,'--
','color',[0,0.5,0]);
plot(thnIR(ir)*[1,1],YL,'m');plot(thnCNR(ir)*[1,1],YL,'m--');
legend('srr','stt','srt')
box on
set(gca,'xlim',[-1,1]*pi);
%%
if 1==0
   KI=(pi*c)^(1/2);
   a = KI./((2*pi*r).^(1/2));

   % Mode I Equations
   fxx=((cos(theta./2)).*(1-sin(theta./2).*(sin(3*theta./2))));
   fyy=((cos(theta./2)).*(1+sin(theta./2).*(sin(3*theta./2))));
   fxy=((sin(theta./2)).*(cos(theta./2)).*(cos(3*theta./2)));

   figure(3); clf
   subplot(211)
   % plot(theta,[sxx;syy;sxy])
   hold on;
   % plot(theta,a*[fxx;fyy;fxy],'k--')
   plot(theta,[fxx;fyy;fxy])
   legend('fxx','fyy','fxy')
   set(gca,'xlim',[-1,1]*pi);
   %
```

```
    fxr=fxx.*cos(theta)+fxy.*sin(theta);
    fyr=fxy.*cos(theta)+fyy.*sin(theta);
    fxt=-fxx.*sin(theta)+fxy.*cos(theta);
    fyt=-fxy.*sin(theta)+fyy.*cos(theta);
    frr=fxr.*cos(theta)+fyr.*sin(theta);
    frt=fxt.*cos(theta)+fyt.*sin(theta);
    ftt=-fxt.*sin(theta)+fyt.*cos(theta);

    % frr=cos(theta/2).*(1+(sin(theta)).^2);
    % ftt=cos(theta/2).^2;
    % frt=cos(theta/2).*sin(theta);

    subplot(212)
    plot(theta,[frr;ftt;frt]);
    legend('frr','ftt','frt')

    set(gca,'xlim',[-1,1]*pi);
    % end
end
```

Appendix E: MATLAB and COMSOL Scripts for RRR Triple Junction Stability

Find maximum values: calculates the maximum stress value(s) and its position(s) along a free boundary
FindMax.m

```
function [Amax,ymax]=FindMax(fem,Hm,Yr,HM);

% Hm=-fem.const.H/2*.8; Yr=fem.const.Yir; HM=fem.const.H/2*.8;

v1=linspace(Hm,Yr,10000); %y vector of sampling points
v2=v1*0; %x vector of sampling points
A=postinterp(fem,'s1_smps',[v2;v1]);
[Amax(1),Imax] = max(A);
ymax(1) = v1(Imax);

v1=linspace(HM,Yr); %y vector of sampling points
v2=v1*0; %x vector of sampling points
A=postinterp(fem,'s1_smps',[v2;v1]);
[Amax(2),Imax] = max(A);
ymax(2) = v1(Imax);
```

Ridge geometry and velocity script: relates ridge azimuth with ridge opening rate
RRRgeomAZ.m

```
function
[PR1,PR2,PR3,P1R2,P1R3,P2R1,P2R3,P3R1,P3R2,VP1,VP2,VP3]=RRRgeomAz(ar
2,ar3,U1)
ar1=pi/2;
% azimuths of plates
ap1=-pi/2+ar2+ar3;
ap2= pi/2+ar3-ar2;
ap3= pi/2-ar3+ar2;
% Velocity wrt triple junction
U=-U1/(2*cos(ap3));
% Velocities of each plate;
VP1=U*[sin(ap1),cos(ap1)];
VP2=U*[sin(ap2),cos(ap2)];
VP3=U*[sin(ap3),cos(ap3)];
% Full spreading rate of ridges
U2=norm(VP3-VP1);
U3=norm(VP2-VP1);
```

```
% Central velocity of ridges
VR1=(VP2+VP3)/2;
VR2=(VP3+VP1)/2;
VR3=(VP1+VP2)/2;

%
th=linspace(0,2*pi,100);
ls=linspace(-1,1,100)*2*max([U1,U2,U3]);
%VP3=; %AUS
figure(1); clf; axis equal; hold on;
plot(VP1(1),VP1(2),'ob');
plot(VP1(1)+U2*cos(th),VP1(2)+U2*sin(th),'b'); %possibility for VP3 using VP1
% plot(VP1(1)+U2*cos(a31),VP1(2)+U2*sin(a31),'og'); %solution for VP3 using
VP1
% plot(VP2(1)+U1*cos(a32),VP2(2)+U1*sin(a32),'xm'); %solution for VP3 using
VP1

plot(VP2(1),VP2(2),'or');
plot(VP2(1)+U1*cos(th),VP2(2)+U1*sin(th),'r'); %possibility for VP3 using VP2

plot(VP3(1),VP3(2),'og');
% plot triangle
plot([VP1(1),VP2(1),VP3(1),VP1(1)],[VP1(2),VP2(2),VP3(2),VP1(2)],'k')
%
plot(VR1(1)+ls*sin(ar1),VR1(2)+ls*cos(ar1),'m');
plot(VR2(1)+ls*sin(ar2),VR2(2)+ls*cos(ar2),'m');
plot(VR3(1)+ls*sin(ar3),VR3(2)+ls*cos(ar3),'m');

%%
LR=8;
LP=3;

PR1=-LR*[sin(ar1),cos(ar1)];
PR2=-LR*[sin(ar2),cos(ar2)];
PR3=LR*[sin(ar3),cos(ar3)];

P1R2=PR2-LP*[-cos(ar2),sin(ar2)];
P3R2=PR2-LP*[cos(ar2),-sin(ar2)];
P2R3=PR3-LP*[cos(ar3),-sin(ar3)];
P1R3=PR3-LP*[-cos(ar3),+sin(ar3)];
P3R1=PR1-LP*[-cos(ar1),sin(ar1)];
P2R1=PR1-LP*[cos(ar1),-sin(ar1)];

figure(2); clf;axis equal; hold on;
%plot 3 ridges:
plot([0,PR1(1)],[0,PR1(2)],'r');
```

```
plot([0,PR2(1)],[0,PR2(2)],'r');
plot([0,PR3(1)],[0,PR3(2)],'r');


plot([P1R2(1),P3R2(1)],[P1R2(2),P3R2(2)],'b')
plot([P2R3(1),P1R3(1)],[P2R3(2),P1R3(2)],'b')
plot([P3R1(1),P2R1(1)],[P3R1(2),P2R1(2)],'b')

fill([P1R2(1),PR2(1),0,PR3(1),P1R3(1),P1R2(1)],...
   [P1R2(2),PR2(2),0,PR3(2),P1R3(2),P1R2(2)],...
   'b')
fill([P2R3(1),PR3(1),0,PR1(1),P2R1(1),P2R3(1)],...
   [P2R3(2),PR3(2),0,PR1(2),P2R1(2),P2R3(2)],...
   'r')
fill([P3R1(1),PR1(1),0,PR2(1),P3R2(1),P3R1(1)],...
   [P3R1(2),PR1(2),0,PR2(2),P3R2(2),P3R1(2)],...
   'g')
quiver((P1R2(1)+P1R3(1))/2,(P1R2(2)+P1R3(2))/2,VP1(1),VP1(2),'k')
quiver((P2R3(1)+P2R1(1))/2,(P2R3(2)+P2R1(2))/2,VP2(1),VP2(2),'k')
quiver((P3R1(1)+P3R2(1))/2,(P3R1(2)+P3R2(2))/2,VP3(1),VP3(2),'k')
```

Symmetry Stability Models
RTJ_geomodel_thesis_15.m

```
%Symmetric Models
x=deg2rad(15);
a=deg2rad(0);
[PR1,PR2,PR3,P1R2,P1R3,P2R1,P2R3,P3R1,P3R2,U1,U2,U3]=RRRgeomAz(-
x,x,1);

% Width of ellipse
Ew=0.002;
dt = 1/abs((U2(2)-U3(2))/(PR2(2)-PR3(2)));

%% COMSOL Multiphysics Model M-file
% Generated by COMSOL 3.4 (COMSOL 3.4.0.248, $Date: 2007/10/10 16:07:51 $)

flclear fem

% COMSOL version
clear vrsn
vrsn.name = 'COMSOL 3.4';
vrsn.ext = '';
vrsn.major = 0;
vrsn.build = 248;
vrsn.rcs = '$Name:  $';
```

```
vrsn.date = '$Date: 2007/10/10 16:07:51 $';
fem.version = vrsn;

% Geometry
% store azimuth
fem.const.anorth=x-a;
fem.const.asouth=pi-x-a;

% parr={point2(0,0)};
% g1=geomcoerce('point',parr);
carr={curve2([0,PR1(1)],[0,PR1(2)],[1,1]), ...
   curve2([PR1(1),P2R1(1)],[PR1(2),P2R1(2)],[1,1]), ...
   curve2([P2R1(1),P2R3(1)],[P2R1(2),P2R3(2)],[1,1]), ...
   curve2([P2R3(1),PR3(1)],[P2R3(2),PR3(2)],[1,1]), ...
   curve2([PR3(1),0],[PR3(2),0],[1,1])};
g2=geomcoerce('solid',carr); %construct plate 2
carr={curve2([0,PR1(1)],[0,PR1(2)],[1,1]), ...
   curve2([PR1(1),P3R1(1)],[PR1(2),P3R1(2)],[1,1]), ...
   curve2([P3R1(1),P3R2(1)],[P3R1(2),P3R2(2)],[1,1]), ...
   curve2([P3R2(1),PR2(1)],[P3R2(2),PR2(2)],[1,1]), ...
   curve2([PR2(1),0],[PR2(2),0],[1,1])};
g3=geomcoerce('solid',carr); %construct plate 1
carr={curve2([0,PR3(1)],[0,PR3(2)],[1,1]), ...
   curve2([PR3(1),P1R3(1)],[PR3(2),P1R3(2)],[1,1]), ...
   curve2([P1R3(1),P1R2(1)],[P1R3(2),P1R2(2)],[1,1]), ...
   curve2([P1R2(1),PR2(1)],[P1R2(2),PR2(2)],[1,1]), ...
   curve2([PR2(1),0],[PR2(2),0],[1,1])};
g1=geomcoerce('solid',carr); %construct plate 3
%
g4=ellip2((-1-PR1(1))/1,Ew,'base','center','pos',{PR1(1),PR1(2)},'rot','0'); %rift
ellipse
%
g5=geomcomp({g2,g3},'ns',{'g2','g3'},'sf','g2+g3','edge','none'); %combined 3 plates
g6=geomcomp({g4,g5},'ns',{'g4','g5'},'sf','g5-g4','edge','none'); %model geometry
with 3 plates

% Geometry objects
clear s

s.objs={g6};
s.name={'Pl'};
s.tags={'g6'};

fem.draw=struct('s',s);
fem.geom=geomcsg(fem);
```

```
figure(2); clf;
geomplot(fem,'edgelabels','on','submode','off'); axis equal;

%% Initialize and refine mesh for 15
refedg=0.02;
fem.mesh=meshinit(fem, ...
   'hauto',3,...
   'hmaxedg',[9, refedg, 8, refedg]);
% meshplot(fem)

% Application mode 1
clear appl
appl.mode.class = 'SmePlaneStress';
appl.module = 'SME';
appl.gporder = 4;
appl.cporder = 2;
appl.assignsuffix = '_smps';
clear bnd
bnd.Rx = {0,U2(1)*dt,U3(1)*dt};
bnd.Hx = {0,1,1};
bnd.constrcond = {'free','displacement','displacement'};
bnd.Ry = {0,U2(2)*dt,U3(2)*dt};
bnd.Hy = {0,1,1};
%% Boundary Conditions

bnd.ind = [3,3,2,2,1,3,2,1,1,1,1];
%boundary [1,2,3,4,5,6,7,8,9,0,1];

%%
appl.bnd = bnd;
clear equ
equ.nu=0.25;
equ.E=1;
appl.equ = equ;
fem.appl{1} = appl;
fem.border = 1;

% Multiphysics
fem=multiphysics(fem);

% Extend mesh
fem.xmesh=meshextend(fem);

% Solve problem
fem.sol=femstatic(fem, ...
```

```
            'solcomp',{'u','v'}, ...
            'outcomp',{'u','v'});

% Save current fem structure for restart purposes
fem0=fem;


%% Plot Results
%Stress enhancement map

figure(3); clf;
% Plot solution
postplot(fem, ...
   'tridata',{'max(min(mises_smps,2.0),1.0)','cont','internal'}, ...
   'trimap',cold(1024), ...
   'tribar','on',...
   'title','Surface: von Mises stress',...
   'geom','off');
hold on;
postplot(fem, ...
   'contdata',{'mises_smps','cont','internal'}, ...
   'contmap','jet(1024)', ...
   'contbar','on',...
   'contlevel',1.0:0.2:4.0);
set(gca,'visible','off')
axis equal
axis([-2,1,-2,2])

%% Stress profile along ridge
figure(4); clf
%north ridge
H(1)=postcrossplot(fem,1,9, ...    'Npoints',10,...
   'lindata','s1_smps', ...
   'linxdata',{'y/cos(anorth)','unit','m'});hold on
% south ridge
H(2)=postcrossplot(fem,1,8, ...    'Npoints',10,...
   'lindata','s1_smps', ...
   'linxdata',{'-y/cos(asouth)','unit','m'});
xlim([-4,4]); ylim([0,4]);
xlabel('Distance along ridge','fontsize',18)
ylabel('Tension Enhancement','fontsize',18)
title('First principal stress','fontsize',24)
set(gca,'fontsize',18)
set(H,'linewidth',2)
box on; grid off
hold on
```

```
plot([1,1]*-1.35, [0,4],'k','linewidth',1);
plot([1,1]*1.35, [0,4],'k','linewidth',1);

%% Find Max
fem.const.H=8; %height of plate
Hm=-fem.const.H/2*.8; Yr=0; HM=fem.const.H/2*.8;
   [Amax,ymax]=FindMax(fem,Hm,Yr,HM);
```

Asymmetry Stability Models
RTJ_geomodel_thesis_7_5_7_5.m

```
%% Velocity Triangle Geometry
% U2 = 55.0;  %57.31; %29; %half spreading rate of SEIR in mm/yr (AUS wrt ANT)
% U1 = 47.5; %49.69; %24; %half spreading rate of CIR in mm/yr (AUS wrt AFR)
% U3 = 13.6; %13.92;% 7; %half spreading rate of SWIR in mm/yr (ANT wrt AFR)
% [PR1,PR2,PR3,P1R2,P1R3,P2R1,P2R3,P3R1,P3R2]=RRRgeom(U1,U2,U3);

%Symmetric Models
x=deg2rad(7.5);
a=deg2rad(7.5);
[PR1,PR2,PR3,P1R2,P1R3,P2R1,P2R3,P3R1,P3R2,U1,U2,U3]=RRRgeomAz(-x-
a,x-a,1);

% Width of ellipse
Ew=0.002;


dt = 1/abs((U2(2)-U3(2))/(PR2(2)-PR3(2)));


%% COMSOL Multiphysics Model M-file
% Generated by COMSOL 3.4 (COMSOL 3.4.0.248, $Date: 2007/10/10 16:07:51 $)

flclear fem

% COMSOL version
clear vrsn
vrsn.name = 'COMSOL 3.4';
vrsn.ext = '';
vrsn.major = 0;
vrsn.build = 248;
vrsn.rcs = '$Name:  $';
vrsn.date = '$Date: 2007/10/10 16:07:51 $';
fem.version = vrsn;
```

```
% Geometry
% store azimuth
fem.const.anorth=x-a;
fem.const.asouth=pi-x-a;

% parr={point2(0,0)};
% g1=geomcoerce('point',parr);
carr={curve2([0,PR1(1)],[0,PR1(2)],[1,1]), ...
   curve2([PR1(1),P2R1(1)],[PR1(2),P2R1(2)],[1,1]), ...
   curve2([P2R1(1),P2R3(1)],[P2R1(2),P2R3(2)],[1,1]), ...
   curve2([P2R3(1),PR3(1)],[P2R3(2),PR3(2)],[1,1]), ...
   curve2([PR3(1),0],[PR3(2),0],[1,1])};
g2=geomcoerce('solid',carr); %construct plate 2
carr={curve2([0,PR1(1)],[0,PR1(2)],[1,1]), ...
   curve2([PR1(1),P3R1(1)],[PR1(2),P3R1(2)],[1,1]), ...
   curve2([P3R1(1),P3R2(1)],[P3R1(2),P3R2(2)],[1,1]), ...
   curve2([P3R2(1),PR2(1)],[P3R2(2),PR2(2)],[1,1]), ...
   curve2([PR2(1),0],[PR2(2),0],[1,1])};
g3=geomcoerce('solid',carr); %construct plate 1
carr={curve2([0,PR3(1)],[0,PR3(2)],[1,1]), ...
   curve2([PR3(1),P1R3(1)],[PR3(2),P1R3(2)],[1,1]), ...
   curve2([P1R3(1),P1R2(1)],[P1R3(2),P1R2(2)],[1,1]), ...
   curve2([P1R2(1),PR2(1)],[P1R2(2),PR2(2)],[1,1]), ...
   curve2([PR2(1),0],[PR2(2),0],[1,1])};
g1=geomcoerce('solid',carr); %construct plate 3
%
g4=ellip2((-1-PR1(1))/1,Ew,'base','center','pos',{PR1(1),PR1(2)},'rot','0'); %rift
ellipse
%
g5=geomcomp({g2,g3},'ns',{'g2','g3'},'sf','g2+g3','edge','none'); %combined 3 plates
g6=geomcomp({g4,g5},'ns',{'g4','g5'},'sf','g5-g4','edge','none'); %model geometry
with 3 plates

% Geometry objects
clear s

s.objs={g6};
s.name={'Pl'};
s.tags={'g6'};

fem.draw=struct('s',s);
fem.geom=geomcsg(fem);


figure(2); clf;
geomplot(fem,'edgelabels','on','submode','off'); axis equal;
```

```
%% Initialize and refine mesh for 15
refedg=0.02;
fem.mesh=meshinit(fem, ...
   'hauto',3,...
   'hmaxedg',[9, refedg, 8, refedg]);
% meshplot(fem)

%% (Default values are not included)

% Application mode 1
clear appl
appl.mode.class = 'SmePlaneStress';
appl.module = 'SME';
appl.gporder = 4;
appl.cporder = 2;
appl.assignsuffix = '_smps';
clear bnd
bnd.Rx = {0,U2(1)*dt,U3(1)*dt};
bnd.Hx = {0,1,1};
bnd.constrcond = {'free','displacement','displacement'};
bnd.Ry = {0,U2(2)*dt,U3(2)*dt};
bnd.Hy = {0,1,1};
%% Boundary Conditions

bnd.ind = [3,3,2,2,2,3,1,1,1,1,1];
%boundary [1,2,3,4,5,6,7,8,9,0,1];

%%
appl.bnd = bnd;
clear equ
equ.nu=0.25;
equ.E=1;
appl.equ = equ;
fem.appl{1} = appl;
fem.border = 1;

% Multiphysics
fem=multiphysics(fem);

% Extend mesh
fem.xmesh=meshextend(fem);

% Solve problem
fem.sol=femstatic(fem, ...
              'solcomp',{'u','v'}, ...
```

```
            'outcomp',{'u','v'});

% Save current fem structure for restart purposes
fem0=fem;
%% Plot Results
%Stress enhancement map

figure(3); clf;
% Plot solution
postplot(fem, ...
   'tridata',{'max(min(mises_smps,2.0),1.0)','cont','internal'}, ...
   'trimap',cold(1024), ...
   'tribar','on',...
   'title','Surface: von Mises stress',...
   'geom','off');
hold on;
postplot(fem, ...
   'contdata',{'mises_smps','cont','internal'}, ...
   'contmap','jet(1024)', ...
   'contbar','on',...
   'contlevel',1.0:0.2:4.0);
set(gca,'visible','off')
axis equal
axis([-2,1,-2,2])

%% Stress profile along ridge
figure(4); clf
%north ridge
H(1)=postcrossplot(fem,1,8, ...    'Npoints',10,...
   'lindata','s1_smps', ...
   'linxdata',{'y/cos(anorth)','unit','m'});hold on
% south ridge
H(2)=postcrossplot(fem,1,9, ...    'Npoints',10,...
   'lindata','s1_smps', ...
   'linxdata',{'-y/cos(asouth)','unit','m'});
xlim([-4,4]); ylim([0,4]);
xlabel('Distance along ridge','fontsize',18)
ylabel('Tension Enhancement','fontsize',18)
title('First principal stress','fontsize',24)
set(gca,'fontsize',18)
set(H,'linewidth',2)
box on; grid off
hold on
plot([1,1]*-1.35, [0,4],'k','linewidth',1);
plot([1,1]*1.35, [0,4],'k','linewidth',1);
```

```
%% Find Max
fem.const.H=8; %height of plate
Hm=-fem.const.H/2*.8; Yr=0; HM=fem.const.H/2*.8;
   [Amax,ymax]=FindMax(fem,Hm,Yr,HM);
```

References

Bird, R.T. and Naar, D.F., 1994, Intratransform origins of mid-ocean ridge microplates: Geology, v. 22, p. 987-990.

Bird, R.T., Tebbens, S.F., Kleinrock, M.C., and Naar D.F., 1999, Episodic triple-junction migration by rift propagation and microplates: Geology, v. 27, p. 911-914.

COMSOL, 2006, User's Guide, COMSOL, (http://comsol.com/products/multiphysics/)

Cronin, V.S., 1992, Types and kinematic stability of triple junctions: Tectonophysics, v. 207, p. 287-301.

DeMets, C., Gordon, R.G., Argus, D.F., and Stein, S., 1994, Effect of recent revisions to the geomagnetic reversal time scale on estimates of current plate motions: Geophysical Research Letters, v. 21, p. 2191-2194.

Erdogan, F. and G.C. Sih, 1963, On the Crack Extension in Plates Under Plane Loading and Transverse Shear: Journal of Basic Engineering, v 85D, p. 519-527.

Fournier, M., C. Petit, N. Chamot-Rooke, O. Fabbri, P. Huchon, B. Maillot, and C. Lepvrier, 2008, Do ridge-ridge-ridge triple junctions exist on Earth? Evidence from the Aden-Owen- Carlberg junction in the NW Indian Ocean, Basin Research, v. 20, p. 575-590, doi: 10.1111/j1365-2117.2008.00356.x.

Honsho, C., K. Tamaki, H. Fujimoto, 1996, Three-dimensional magnetic and gravity studies of the Rodriguez Triple Junction in the Indian Ocean: Journal of Geophysical Research, v. 101, p. 15,837-15,848.

Johnson, G.L., Hey, R.N., and A. Lowrie, 1973, Marine geology in the environs of Bouvet Island and the South Atlantic Triple Junction: Marine Geophysical Researches, v. 2, p. 23-36.

Klein, E.M., Smith, D.K., Williams, C.M., and Schouten, H., 2005, Counter-rotating microplates at the Galápagos triple junction: Nature, v. 433, p. 855-858.

Krause, D.C. and N.D. Watkins, 1970, North Atlantic Crustal Genesis in the Vicinity of the Azores: v. 19, p. 261-283.

Larson, R.L., Searle, R.C., Kleinrock, M.C., Schouten, H., Bird, R.T., Naar, D.F., Rusby, R.I., Hooft, E.E., and H. Lasthiotakis, 1992, Roller-bearing tectonic evolution of the Juan Fernandez microplate: Nature, v. 356, p. 571-576, doi 10.1038/356571a0.

Lawn, Brian R. Fracture of Brittle Solids. Cambridge: Cambridge UP, 1993.

Lawyer, L., 1984, The Cenozoic evolution of the Bouvet triple junction: EOS Transactions, American Geophysical Union, v. 65, pg. 1100.

Ligi, M., Bonatti, E., Bortoluzzi, G., Carrara, G., Fabretti, P. Gilod, D., Peyve, A.A., Skolotnev, S. and Turko, N., 1999, Bouvet Triple Junction in the South Atlantic: Geology and Evolution, Journal of Geophysical Research, v. 104, p. 29,365–29,385.

Lonsdale, P., 1983, Overlapping rift zones at the 5.5° S offset of the East Pacific Rise: Journal of Geophysical Research, v. 88, pg. 9393-9406

Lonsdale, P., 1985, Linear volcanoes along the Pacific-Cocos plate boundary, 9° N to the Galápagos triple junction: Tectonophysics, v. 116, p. 255-279.
Lonsdale, P., 1988, Structural patterns of the Galapagos microplate and evolution of the Galapagos triple junction: Journal of Geophysical Research, v. 93, p. 13,551-13,574.
Lonsdale, P., Blum, N., and Puchelt, H., 1992, The RRR triple junction at the southern end of the Pacific-Cocos East Pacific Rise: Earth and Planetary Science Letters, v. 109, p. 73-85.
MacDonald, K.C., and P.J. Fox, 1983, Overlapping spreading centers: New accretion geometry on the East Pacific Rise: Nature, v. 301, p. 55-58.
McKenzie, D.P., and R.L. Parker, 1967, The North Pacific: An example of tectonics of a sphere: Nature, v. 216, p.1276-1280.
McKenzie, D.P., and W.J. Morgan, 1969, Evolution of triple junctions: Nature, v. 224, p. 125-133.
McKenzie, D.P. and J.G. Sclater, 1971, Evolution of the Indian Ocean since Late Cretaceous: Geophysical Journal of the Royal Astronomical Society, v. 82, p. 437-528.
Menke, William, Plate motion calculator, http://www.ldeo.columbia.edu/users/menke/plates.html
Mitchell, N.C., 1991, Distributed extension at the Indian Ocean triple junction: Journal of Geophysical Research, v. 96, p. 8019-8043.
Mitchell, N.C. and L.M. Parson, 1993, The Tectonic Evolution of the Indian Ocean Triple Junction, Anomaly 6 to Present: Journal of Geophysical Research, v. 98, p. 1793-1812.
Mitchell, N.C., and R.A. Livermore, 1998, The present configuration of the Bouvet triple junction: Geology, v. 26, p. 267-270.
Patriat, P., and V. Courtillot, 1984, On the stability of triple junctions and its relation to episodicity in spreading: Tectonics, v. 3, p. 317-332.
Patriat P., and J. Segoufin, 1988, Reconstruction of the Central Indian Ocean: Tectonophysics, v. 155, p. 211-234.
Patriat, P., Sauter, D., Munschy, M., and L. Parson, 1997, A Survey of the Southwest Indian Ridge Axis Between Atlantis II Fracture Zone and the Indian Ocean Triple Junction: Regional Setting and Large Scale Segmentation: Marine Geophysical Researches, v. 19, p. 457-480, doi 10.1023/A: 1004312623534.
Sauter, D., Mendel, V., Rommevaux-Jestin, C., Patriat, P., and M. Munschy, 1997, Propagation of the Southwest Indian Ridge at the Rodrigues Triple Junction: Marine Geophysical Researches, v. 19, p. 553-567, doi: 10.1023/A:1004313109111.
Schouten, H., Klitgord, K. D. and D.G. Gallo, 1993, Edge-driven microplate kinematics: Journal of Geophysical Research, v. 98, p. 6689–6701.
Schouten, H., Smith, D.K., Montési, G.J., Zhu, W., and E.M. Klein, 2008, Cracking north of the Galápagos triple junction: Geology, v. 36, n. 5, p. 339-342.
Sclater, J.G., Bowin, C., Hey, R., Hoskins, H., Peirce, J., Phillips, J., and C. Tapscott, 1976, The Bouvet Triple Junction: Journal of Geophysical Research, v. 81, p. 1857-1869.
Sclater, J.G., Fisher, R.L., Patriat, P., Tapscott, C., and B. Parsons, 1981, Eocene to

recent development of the Southwest Indian Ridge, a consequence of the evolution of the Indian Ocean triple junction: Geophys. J.R. Astr. Soc., v. 64, p. 587-604.
Searle, R.C., 1980, Tectonic Pattern of the Azores Spreading Center and Triple Junction: Earth and Planetary Science Letters, v. 51, p. 415-434.
Searle, R.C. and J. Francheteau, 1986, Morphology and Tectonics of the Galapagos Triple Junction: Marine Geophysical Researches, v. 8, p. 95-129.
Shah, R.C. and A.S'. Kobayashi, 1973, Stress Intensity Factors for an Elliptical Crack Approaching the Surface of a Semi-Infinite Solid: International Journal of Fracture, v. 9, p. 133-146.
Sih, G.C., 1974, Strain-energy-density factor applied to mixed mode crack problems: International Journal of Fracture, v. 10, p. 305-321.
Tapscott, C.R., Patriat, P., Fisher, R., Sclater, J.G., Hoskins, H., and B. Parsons, 1980, The Indian Ocean Triple Junction: J. Geophys. Res., v. 85, p. 4723-4739, doi:10.1029/JB085iB09p04723.
Vogt, P., and W. Jung, 2004, The Terceira Rift as hyper-slow, hotspot-dominated oblique spreading axis: A comparison with the other slow-spreading plate boundaries, Earth and Planetary Science Letters, 218, p. 77–90.
Wessel, P. and W. H. F. Smith, Free software helps map and display data: EOS Trans. AGU, 72, 441, 1991
West, B.P., H. Fujimoto, C. Honsho, K. Tamaki, and J.C. Sempéré, 1995, A three-dimensional gravity study of the Rodrigues Triple Junction and Southeast Indian Ridge: Earth and Planetary Science Letters, 133, p. 175-184.